Spring 2016

Estimation of papilledema severity using spectral-domain optical coherence tomography

Jui-Kai Wang
University of Iowa

ESTIMATION OF PAPILLEDEMA SEVERITY USING SPECTRAL-DOMAIN OPTICAL COHERENCE TOMOGRAPHY

by

Jui-Kai Wang

A thesis submitted in partial fulfillment of the
requirements for the Doctor of Philosophy degree
in Electrical and Computer Engineering
in the Graduate College of
The University of Iowa

May 2016

Thesis Supervisor: Associate Professor Mona K. Garvin

Graduate College
The University of Iowa
Iowa City, Iowa

CERTIFICATE OF APPROVAL

PH.D. THESIS

This is to certify that the Ph.D. thesis of

Jui-Kai Wang

has been approved by the Examining Committee for the thesis requirement for the Doctor of Philosophy degree in Electrical and Computer Engineering at the May 2016 graduation.

Thesis Committee: _____
Mona K. Garvin, Thesis Supervisor

_____
Randy H. Kardon

_____
Joseph M. Reinhardt

_____
Milan Sonka

_____
Xiaodong Wu

ACKNOWLEDGEMENTS

One laboratory cubicle, two heart-breaking relationships, three brand-new cars, four oral presentations in international conferences, five different apartments, six years working on only one significant research topic, and finally, in this seventh year, I am writing my dissertation acknowledgment, right here, right now. Life is bitter but also sweet; a big part of me is sewn together by all of the tears and laughter with great people during these years. Therefore, now is the perfect time, and here is the perfect place, to allow me to show my gratitude to all of these special people.

First of all, I must express my appreciation to Prof. Garvin for being my research advisor since 2010. Without her guidance and support, my academic dream would have been shattered, and I would have gone back home to be a cook. She showed me how to stay positive throughout everything and always do research with the utmost accuracy. The spirit I learned from her is beneficial for me not only in academia, but also in every day life. Dr. Kardon also plays a significant role in my Ph.D journey. He has a magical ability to explain difficult clinical backgrounds using very understandable language. He made me realize that a knowledgeable expert always has the ability to explain complicated concepts in a clear and simple way so that people without that background knowledge can quickly follow the key ideas in a short conversation. Next, I want to thank Dr. Kupersmith, Dr. Sibony and the other doctors/members in the IIHTT OCT group. I am so glad that I can contribute my efforts into this great project and feel honored that my name is listed in our published papers. Next, I would like to thank Prof. Sonka, Prof. Reinhardt and Prof. Wu serving on my dissertation committee and giving me valuable suggestions about my research work. It is my best pleasure to have you here to make this doctoral work thorough and complete. I also appreciate Prof. Saha, who financially supported me in my first year here, as well as Prof. Kruger, Prof. Anderson and Prof. Bai, who gave me TA positions to experience teaching and communicating with students. I have been fortunate to learn from so

many great professors in the ECE department and I am so proud to receive my Ph.D. from this excellent program. Finally, I want to mention that this thesis was supported in part by the National Eye Institute (NEI) of the National Institute of Health (NIH) R01 EY023279, U10 EY017281-01A1, U10 EY017387-01A1, 3U10EY017281-01A1S1, and the Department of Veterans Affairs Rehabilitation Research and Development Division (Iowa City Center for the Prevention and Treatment of Visual Loss and Career Development Award 1IK2RX000728).

In other aspect of life, Cathy Kern, my Iowa Mom, is the first person that I need to thank. She patiently helped me figure out endless life problems. Xiaoxin, Junjie, Qiao, Li, Liang, Saleh, Dakai, Feiran, Zhi, Bhavna, Paul, Kyungmoo, Andreas, Sam, Caitlin, Sydney, Dina, Andy Chang, Victor, Chen, Jason, Will, Danielle, and other good friends have also done many favors for me throughout these years. Emily and Mr. and Mrs. Beisler helped me so much in improving my English ability and showed me how the American culture works. Malerie endured my fragile-hearted personality and encouraged me to improve myself and stay strong. I will definitely miss all of you when we are scattered in all different countries in the coming years. My life is colored because of you.

Last but not least, I would like to dedicate this dissertation to my beloved grandparents in heaven. I am deeply sorry that I could not finish this earlier for you to see my achievements when you were alive. I also want to thank Aunt Chun-Hui. Without your support, I would have had no chance to even start my academic journey. And, Dad, I love you. I finally got this degree and grew up to be the type of person that you expect me to be. I hope you will always feel proud when you think/talk about me. Finally, I want to particularly mention my best friend Hsing-Ying. In these seven years, your kindness and tolerance have strengthened me every single day. You saved me so many times when I was at the lowest points. I want to share this honor with you and bless our ceaseless friendship.

ABSTRACT

Papilledema is a particular type of optic disc swelling caused by elevated intracranial pressure. By observing the visible features from fundus images or direct funduscopic examination, a typical method of assessing papilledema (i.e., the six-stage Frisén grading system) is qualitative and frequently suffers from low reproducibility.

Compared to fundus images, spectral-domain optical coherence tomography (SD-OCT) is a relatively new imaging technique and enables cross-sectional information of the retina to be acquired. Using SD-OCT images, quantitative measurements, such as the retinal volume or depth, are intuitively more robust than the traditional qualitative approach to evaluate papilledema. Also, multiple studies suggest that deformation of the peripapillary retinal pigment epithelium and/or Bruch's membrane (pRPE/BM) may reflect intracranial pressure change. In other words, modeling/quantifying the pRPE/BM shape can potentially be another indicator of papilledema. However, when the optic disc is severely swollen, the retinal structure is dramatically deformed and often causes the commercial SD-OCT devices to fail to segment the retinal layers. Without an appropriate layer segmentation, the retinal measurements are not reliable.

To solve the issue of inconsistently assessing papilledema severity, a comprehensive machine-learning framework is proposed in this doctoral work to achieve the goal by accomplishing the following four aims. First, robust approaches are developed to automatically segment the retinal layers in 2D and 3D SD-OCT images, including cases in which the optic discs are severely swollen. Second, semi- and fully automated methodologies are designed to segment the pRPE/BM opening under the swollen inner retina in these SD-OCT images. Third, 2D/3D pRPE/BM shape models are constructed by extending the pre-segmented pRPE/BM opening in both 2D and 3D SD-OCT images, and then the 2D/3D pRPE/BM shape measures are computed. Finally, based on the previous segmented retinal layers, eight OCT 2D/3D global/local measurements of retinal structure are reliably computed. Considering

both the 2D/3D pRPE/BM shape measures and these eight OCT features as an input set, a machine-learning framework using the random forest technique is proposed to compute a papilledema severity score (PSS) on a continuous scale. The newly proposed PSS is expected to be an alternative to the traditional qualitative method to provide a more objective measurement of assessing papilledema severity.

PUBLIC ABSTRACT

Papilledema is a specific type of optic-nerve-head (ONH) swelling due to elevated intracranial pressure, and it can indicate serious underlying conditions. Head injury, brain tumor, brain inflammation, subarachnoid hemorrhage, blockage of cerebrospinal fluid (CSF) flow, reduction in CSF reabsorption, idiopathic intracranial hypertension (IIH) are the possible reasons that may cause intracranial hypertension. To diagnose the severity of papilledema, clinicians commonly examine the visible features using either 2D retinal photos or direct observation of the retina. Then, a severity scale from 0 (normal) to 5 (severe) is decided based the clinician's judgment. However, this type of method is not stable, so different clinicians may frequently disagree with each other. Moreover, sometimes even the same clinician may have different decisions after multiple observations of the same retinal image.

Optical coherence tomography (OCT) is a new imaging technique and enables the cross-sectional information of the retina to be acquired. Therefore, the volume of the retina at the ONH region is able to be computed as an indicator to reflect the degree of the optic disc swelling. Similarly, the thickness of certain retinal regions as well as the shape of certain retinal layers are also potentially useful for the same purpose.

In this thesis, a system was proposed to use computers to mimic how clinicians make decisions when measuring the degree of the optic disc swelling. A technique called random forest was used to achieve this goal by automatically deciding the best feature combination from the input feature set, including the previously discussed retinal volume, thickness, and shape measures. It is expected that the output of this machine-learning system is very close to the decisions that clinicians would make; more importantly, this proposed system would have the same results every time if the input features are the same, and the processing takes much less time than clinicians do for similar tasks.

TABLE OF CONTENTS

LIST OF TABLES

Table

LIST OF FIGURES

Figure

CHAPTER 1
INTRODUCTION

Optic disc edema due to raised intracranial pressure, also called papilledema, may be caused by several situations, including head injury, brain tumor, brain inflammation, subarachnoid hemorrhage, and idiopathic intracranial hypertension (IIH) [1, 2]. The six-stage Frisén grading system is a typical assessment of papilledema in clinics [3]. To assign a Frisén grade, neuro-ophthalmologists examine the visible features of retinal vessels and tissue structures of the optic disc and peripapillary retina from direct funduscopic observation or digital color fundus photographs and evaluate the degree of the optic disc edema using a scale from 0 (normal) to 5 (severe). Since the Frisén grading system is a qualitative method, inherent limitations may include the need for specialized clinical expertise, outputs of non-continuous scale, and high intra-/inter-observer variability [4–7]. Thus, there is a strong clinical need to develop quantitative and more objective approaches for the purpose of reliably assessing papilledema severity.

In comparison with traditional fundus photographs, optical coherence tomography (OCT) [8] is a relatively new imaging technique that potentially provides a promising alternative for quantitatively assessing papilledema. Unlike fundus photographs, which only capture the projective appearance of the back of the eye, the OCT images contain high-resolution, cross-sectional views to enable the depth and/or volume of the retinal structure to be directly measured. The first-generation OCT works in the time domain (TD-OCT, commercially available since 2003) and is primarily a 2D imaging technique, as only up to six cross-sectional scans can be acquired during a single acquisition. Take the optic-nerve-head (ONH) protocol for an example: TD-OCT supports six circular B-scans centered at the optic disc opening and also provides the automated measurements of the peripapillary retinal nerve fiber layer (RNFL) and total retinal (TR) thicknesses. Previous studies showed that the RNFL and TR

thicknesses are promising measurements for assessing mild papilledema [4,9,10]. However, when it comes to more severe cases, these thickness-based measurements become unstable because the commercial retinal segmentation approaches often fail [4].

The second-generation OCT works in the frequency domain (SD-OCT, commercially available since 2007), and such machines further allow true volumetric information of the retina to be acquired. Particularly, the volumetric ONH measurement is appealing in cases of the optic disc swelling, because measuring the entire extent of the optic disc edema intuitively makes much more clinical sense than using only the thickness measurements from an arbitrary peripapillary circle. However, although SD-OCT supports true 3D image information, most of the commercial SD-OCT machines still separately segment the retinal layers in each individual B-scan and include crucial assumptions about the distances among different homogeneous retinal layers. Segmenting severely swollen retinal layers using commercial SD-OCT software has a high failure rate, due to the unresolved issues related to dealing with a dramatically deformed inner retina [11, 12].

In addition to the previously discussed OCT measures (i.e., the ONH volume, the RNFL and TR thicknesses), recent studies showed that the shape of the peripapillary retinal pigment epithelium and/or Bruch's membrane (pRPE/BM) layer may also indirectly reflect the intracranial pressure change [13, 14]. Specifically the shape of the pRPE/BM layer in patients with increased intracranial hypertension (ICP) is contorted anteriorly toward the vitreous, and this shape difference is not otherwise explained by disc edema alone. Additional interventions that lower the ICP, including a spinal tap, a shunting procedure, or medical treatments, will restore the pRPE/BM layer to its normal shape, bending away from the vitreous [15]. To quantify the deformation of the pRPE/BM shape, the pRPE/BM shape model was originally constructed by using ten equidistant landmarks that were manually placed from the pRPE/BM opening along the pRPE/BM boundary at both nasal and tem-

poral directions in the central B-scan from a high-definition 5-line raster (HD-5LR, Carl Zeiss Meditec, Inc., Dublin CA) scan for each available subject [14]. However, the step of manually placing equidistant landmarks on the pRPE/BM boundary is very time-consuming, so there is a strong need to develop a new methodology to accelerate these manual steps so that the pRPE/BM shape models can be applied/tested in larger datasets.

To generate the pRPE/BM shape models of papilledema eyes, Bruch's membrane opening (BMO) needs to be identified first. The current challenge in this topic is that the region around BMO is often obscure in SD-OCT images when the optic discs are severely swollen. The swollen retinal tissue reduces the depth that the OCT signals can penetrate and results in image shadows. This type of artifact significantly increases the difficulty of directly finding the true BMO points in regular volumetric SD-OCT images. Without obtaining the correct BMO location, the pRPE/BM shape direction and precise angle cannot be properly measured, which are potentially very important parameters to indicate how much the abnormal intracranial pressure affects the retina [13, 14]. HD-5LR scans, on the other hand, provide a renewed promise for this particular BMO segmentation problem. The SD-OCT devices with HD-5LR protocol first repeatedly scan the same horizontal narrow regions at five indicated retinal areas of interest and then average these repeated scans to construct new individual HD B-scans. However, the trade-off between the image quality and scanning range limits the HD-5LR protocol to merely working in 2D. Therefore, how to combine the information that is obtained from the HD B-scans (2D) and regular SD-OCT volumes (3D) introduces a new and interesting research topic.

Overall, the main goal of this doctoral work is to develop a comprehensive methodology to reliably assess papilledema severity on a continuous scale by addressing the challenges mentioned above. **In particular, the thesis has the following aims:**

- **Aim 1** – Develop automated retinal layer segmentation algorithms specifically

for a swollen optic disc in both 2D high-definition 5-Line raster (HD-5LR) and 3D volumetric SD-OCT scans. The proposed algorithms segment retinal layers using an existing graph-based approach (Li et al. [16]), but the input cost functions and surface constraints are completely re-designed to adapt the need for segmenting a severely swollen optic disc in both 2D and 3D SD-OCT images.

- **Aim 2** – Develop frameworks for combining the information from a HD-5LR scan and the corresponding SD-OCT volume to identify the true Bruch's membrane opening (BMO) under the shadow of the swollen retinal tissue. This is completed by first registering the HD B-scans to the appropriate locations in the corresponding SD-OCT volume, then adopting the information from the HD B-scan to help design the cost images of the volumetric image, and finally applying a graph-theoretic algorithm to identify the visible BMO in the SD-OCT volume.

- **Aim 3** – Construct 2D and 3D shape models of the peripapillary retinal pigment epithelium and/or Bruch's membrane (pRPE/BM) and compute the pRPE/BM shape measures to reflect the degree of the pRPE/BM oriented toward/away from the vitreous. Based on the segmented BM surface from Aim 1, the pRPE/BM statistical shape models are generated using the HD-5LR central B-scan (2D) and the volumetric scan (3D). Furthermore, the pRPE/BM shape measures are extracted from the 2D/3D shape models.

- **Aim 4** – Assess papilledema by outputting a severity score on a continuous scale using a machine-learning system with the input of meaningful OCT features. The proposed papilledema severity score (PSS) is the first machine-learned assessment of papilledema on a continuous scale using quantitative features from the SD-OCT images. This aim is accomplished using random forest classifiers with all of the available OCT features that are obtained from the previous aims.

The PSS is expected to provide a more robust measurement of papilledema severity than the traditional qualitative method does.

1.1 Thesis Organization

The rest of this thesis is organized as follows.

- **Chaper 2** introduces the clinical background of what papilledema is and its symptoms as well as the common measurements. The well-known Frisén grade system, popular OCT measurements, and recent shape analysis are all briefly addressed in this chapter.

- **Chaper 3** discusses more technical details regarding time-domain and frequency-domain OCT imaging, what the challenges and common approaches are for developing automated algorithms to perform the retinal layer segmentation in OCT images, and an overview of how a graph-based algorithm segments retinal layers and the Bruch's membrane opening.

- **Chaper 4** summarizes the automated retinal layer segmentation methods that are heavily used in this doctoral work. Details about how to design the 2D and 3D cost images in multiple resolutions are revealed. The processes of repairing the truncated SD-OCT images are also discussed.

- **Chaper 5** addresses the difficulty of segmenting Bruch's membrane opening (BMO) in cases of a severely swollen optic disc. Semi-/fully automated methods are addressed here, and the technique of combining information from both 2D and 3D SD-OCT to help segment the BMO is also introduced.

- **Chaper 6** provides the details of how to generate 2D and 3D pRPE/BM shape models and compute the shape measures based on the BMO segmentation results from Chapter 5.

- **Chaper 7**, first, illustrates how to compute common OCT features based on the retinal segmentation results from Chapter 4, including the ONH volume and peripapillary RNFL as well as TR thicknesses. Next, region-based volumetric OCT measurements are discussed. Then, a preliminary machine-learning system is provided to test the correlation between the Frisén grades and all the other OCT features in a relatively small dataset. Finally, an overall framework using a random forest algorithm is introduced to obtain a papilledema severity score on a continuous scale, and the results are tested in a larger dataset of a recently finished nation-wide clinical trial (i.e., Idiopathic Intracranial Hypertension Treatment Trial – IIHTT).

- **Chaper 8** concludes the previous chapters and discusses the possible limitations and the potential future work.

CHAPTER 2
CLINICAL BACKGROUND

2.1 Papilledema

Papilledema is a specific type of optic-nerve-head (ONH) swelling due to elevated intracranial pressure, and it can indicate serious underlying conditions [1]. Head injury, brain tumor, brain inflammation, subarachnoid hemorrhage, blockage of cerebrospinal fluid (CSF) flow, reduction in CSF reabsorption, idiopathic intracranial hypertension (IIH) are the possible reasons that may increase intracranial pressure [1]. Fig. 2.1 shows a posterior view of the retina. Because the skull is a bony structure, the total volume inside the skull is fixed. Therefore, any enlargement of cranial constituents may press the other constituents and/or lead to the CSF pressure increasing [1]. CSF normally exists in the subarachnoid space around the brain side instead of the optic nerve side. When the intracranial pressure abnormally elevates, CSF would flow from the brain side to the optic nerve side in the subarachnoid space. Then, the surrounding CSF may inflame the ONH and results in optic disc swelling. In particular, it is not papilledema if the ONH swelling is caused by any other reason (e.g., ischemic optic neuropathy and optic neuritis) other than elevated intracranial pressure.

2.2 Symptoms

Although blindness can happen to patients with severe papilledema, rapid vision loss is not a typical symptom for early stages of papilledema. However, headaches, nausea, and vomiting are very common during this period. When papilledema is developing, patients might temporarily have difficulty seeing clearly, including gray and/or double visions. These visual symptoms, also called the transient visual obscurations (TVO), only last a matter of seconds at the onset, but the severity and frequency of occurrence increase as the time goes by. In general, TVO occurs when patients suddenly change their positions, such as standing up quickly or severe cough-

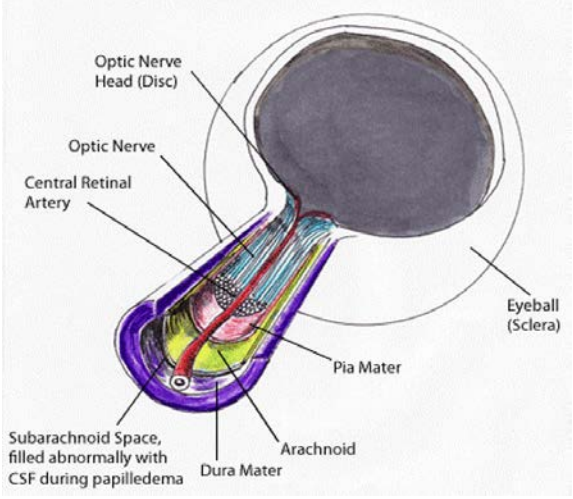

Figure 2.1: Posterior view of an eye. (The image is obtained, with permission, from http://ihrfoundation.org/hypertension/info/C140.)

ing [17]. In the later stage, papilledema patients often suffer unbearable headaches, and urgent treatments are necessary.

Because papilledema can be caused by several reasons, correcting the underlying cause is the direct treatment. If there is no identifiable causes of increased intracranial pressure (i.e., idiopathic intracranial hypertension), medical treatments, such as weight loss and diet, acetazolamide and furosemide, are common options [1, 18–20]. However, if patients fail the maximum medical therapy, for example the patient continues to suffer severe intractable headache and/or progressive vision loss, surgical interventions, such as optic nerve sheath fenestration (ONSF), CSF diversion (shunting) and venous sinus stent placement, are potential options [1, 20, 21]. Therefore, there is a strong need to develop reliable assessments of papilledema so that neuro-ophthalmologists can promptly adjust their treatments based on longitudinal papilledema evaluation.

2.3 Quantifying Papilledema Using Fundus Images

2.3.1 Frisén Grading System

The six-stage Frisén grading system [3] was introduced in 1982 and has been the standard of measurement for papilledema. In practice, neuro-ophthalmologists examine the visible features of the peripapillary retina and the optic disc from direct funduscopic observation or digital color fundus photographs. Then, based on the observations, clinicians assign a severity grade from 0 to 5 to quantify the optic disc swelling; grade 0 indicates normal, grades 1 and 2 represent mild swelling, grade 3 shows moderate abnormality, and a grade of 4 or 5 means that the situation is severe and the optic disc starts to atrophy [3]. Fig. 2.2 shows the digital fundus images with Frisén grade 0 to 4 in order from the left to right. Although the Frisén grading scheme is commonly used in both clinical and research fields, poor reproducibility, high intra- and inter-observer variability, tedious processing steps, specific expertise, and discretized outputs are the major limitations [4–7]. So, modified versions of the Frisén grading scheme have often been studied. For example, to improve the systematic reliability on diagnosing severe papilledema, Scott et al. [4] modified the original Frisén scale scheme by observing key features at different stages. To minimize the intra- and inter-observer variability and accelerate the processing speed, Ecbegaray et al. [5] proposed an automated feature-classifying approach for predicting Frisén scale grades, for which the features included blood vessel, peripapillary texture, and disc margin obscuration features from the fundus photographs.

Although the latest generation of fundus cameras has supported high-definition image quality and full-color information, this imaging technique is still fundamentally limited to 2D. Thus, the volumetric information of the optic disc is difficult to be directly observed and quantified. Stereoscopic fundus photographs could be used to indirectly reconstruct the 2D information into 3D. However, this method is sensitive

Figure 2.2: Digital fundus images with the Frisén grade from 0 to 4.

to eye-movements and fixation instabilities; also, the step of registering two input stereo fundus image is tedious [22].

2.4 Quantifying Papilledema Using Optical Coherence Tomography

2.4.1 Two-Dimensional Thickness Measurements

Optical coherence tomography (OCT) is a relatively new imaging technique and is able to provide cross-sectional images of the optic nerve head (ONH) and/or retina. The original idea of OCT came from Huang et al. [8] in the time domain (TD), and such machines were commercially available after 2003. TD-OCT machines typically capture at most six cross-sectional 2D scans (with an axial resolution of 8 to 10 μm) around the ONH during one acquisition, where the highest scan-dimension is $128 \times 6 \times 1024$ (Cirrus, from Carl Zeiss Meditec, Inc., Dublin, CA). Automated algorithms for segmenting the retinal layer(s) are available on the commercial TD-OCT machines and supported peripapillary thickness measurements of the retinal nerve fiber layer (RNFL) as well as the total retina (TR). Several studies have used the peripapillary RNFL and/or TR thickness measurements for alternatives of the traditional Frisén grading system to quantify papilledema severity [4,9,10]. However, none of these TD-OCT devices can reliably measure the retinal thickness when the input optic disc is severely swollen, because the segmentation step often fails due to the deformation of the swollen retinal structure. To increase the accuracy of assessing the severity of papilledema in cases of the severely swollen optic discs, Scott et al.

suggested using the TR thickness as the reference instead of the RNFL thickness [4]. Overall, using TD-OCT commercial machines to measure papilledema severity most likely only works in cases of mild swelling.

2.4.2 Three-Dimensional Volumetric Measurement

Spectral domain OCT (SD-OCT) [23–25] has been commercially available since 2007. Compared to TD-OCT, SD-OCT provides a much better image resolution. Take Cirrus OCT images (Cirrus, from Carl Zeiss Meditec, Inc., Dublin, CA) for example. An SD-OCT volume covering $6 \times 6 \times 2$ mm^3 can contain $200 \times 200 \times 1024$ voxels using the ONH protocol or $512 \times 128 \times 1024$ voxels using the Macular protocol. Because of the extensively increased amount of the available B-scans in a single SD-OCT volume, volumetric measurements of ophthalmic structures become possible (Fig. 2.3). Compared to the 2D retinal thickness measurements along the arbitrary peripapillary circle, the 3D measurements can be particularly appealing because the volumetric information is intuitively more representative of the degree of optic disc edema. Unfortunately, most of the commercial SD-OCT machines still face the same difficulty as the TD-OCT machines did of not having the ability to robustly and accurately segment the swollen retinal layers. A possible cause of why these commercial OCT devices often fail to accurately segment the retinal layers of swollen optic discs is that the dramatically thickened retina might violate the initial quantitative assumptions in these segmentation algorithms, and then the error propagations contradict the entire layer segmentation [11, 12]. Another challenge for the current commercial SD-OCT devices is that the tip of the optic disc may get truncated when imaging severely swollen optic discs due to the limitation of the SD-OCT image dimensions in the **z** direction. In this case, the quantitative measurements provided from these commercial devices are often significantly underestimated.

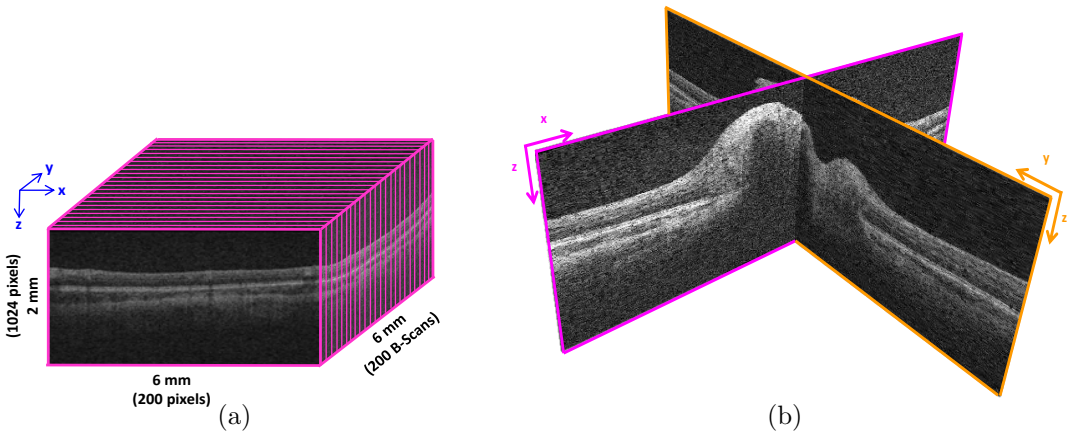

(a) (b)

Figure 2.3: An example of papilledema in SD-OCT image. (a) A 3D image cube. (b) 3D presentation of two perpendicular 2D slices, where the optic disc swelling can be clearly observed.

2.4.3 Shape Measure

Recent studies also have demonstrated that an inverted-U shape (towards the vitreous) of peripapillary retinal pigment epithelium/Bruch's membrane (pRPE/BM), as visible from the ONH SD-OCT scans, may suggest increased intracranial pressure [13–15], which results in developing papilledema. Therefore, measuring the pRPE/BM shape can potentially be another clinical indicator to represent the severity of papilledema. However, even though regular SD-OCT enables retinal cross-sectional images to be acquired, the shadows from a severely inflated inner retina often eclipses the true image signal response from the outer retina around the Bruch's membrane opening (BMO) so that the image visibility around the BMO region is dramatically deteriorated.

Another SD-OCT protocol is called high-definition 5-line raster (HD-5LR) scan, which highly increases the image visibility in each individual B-scan by repeatedly scanning the same retinal region. However, HD-5LR scan only supports five HD B-scans. Due to the difficulties of directly observing the true BMO in the SD-OCT volumes, most recent studies [14, 26] have commonly used HD-5LR scans to analyze

the BMO structure in cases of optic disc swelling. For example, Sibony et al. originally designed a 2D pRPE/BM shape model by manually placing 20 equidistant landmarks on the BM layer at both nasal and temporal sides in the central HD-5LR B-scan to inspect the magnitude of the anterior/posterior displacement of the BM layer [14]. This study successfully demonstrated that the BM layer is more inwardly bowed toward the vitreous in papilledema eyes than normal or anterior ischemic optic neuropathy (AION) eyes. However, this method has an extremely tedious step of manually placing equidistant landmarks on the pRPE/BM boundary for each input HD B-scan. Therefore, it is not feasible to directly apply the pRPE/BM shape model to lager datasets when the landmarks are completely manually placed.

2.5 Summary

The Frisén grading system, based on direct funduscopic observation or digital color fundus photographs, is a standard method of qualitatively assessing the severity of papilledema; however, high intra-/inter-observer variability, need of specific expertise, and tedious processing steps make this traditional method have very low reproducibility. On the other hand, newly introduced SD-OCT enables cross-sectional information of the retina to be acquired and supports quantitative measurements. Also, recent studies have started to use the OCT-based features to evaluate mild papilledema. However, the retinal layers are dramatically deformed when the optic disc is severely swollen. Under this circumstance, most of the current commercial OCT devices cannot provide dependable OCT segmentation and measurements. Therefore, there is a strong need to develop algorithms/approaches to have the ability of segmenting severely swollen retinal layers and further provides reliable OCT measurements (such as the RNFL and TR thicknesses, total and regional ONH volumes, and pRPE/BM shape measures) to reflect the papilledema severity.

CHAPTER 3
TECHNICAL BACKGROUND

3.1 Optical Coherence Tomography

Optical coherence tomography (OCT) has been increasingly used since its introduction in 1991 [8] because of its ability to extract cross-sectional information of the retina. The first generation of OCT operates in the time domain (TD-OCT) using low-coherence interferometry. By linearly or circularly scanning the area at the retina (usually the macular or peripapillary region), an image slice, a.k.a. B-scan, is composed from all of the acquired A-scans. Stratus OCT-3 (Carl Zeiss Meditec, Dublin, CA) is an example of a TD-OCT machine (commercially available in 2003), and each B-scan has typical dimensions of 128×1024 pixels. Due to the limitations of the scanning speed, Stratus OCT-3 can only provide six non-successive B-scans per image.

Fourier-domain OCT (FD-OCT) [23–25,27] [i.e., spectral-domain OCT (SD-OCT)] is a more recent OCT technique. Basically, SD-OCT improves TD-OCT by immobilizing the moving reference mirror and replacing the photo-detector by a low-pass spectra-meter [28–30] to dramatically increase the scanning speed, which provides the ability to image the true 3D contextual information. For example, Zeiss Cirrus OCT (Carl Zeiss Meditec, Dublin, CA) can acquire an ONH image volume with a resolution of $200 \times 200 \times 1024$ voxels, covering $6 \times 6 \times 2$ mm^3 of the retina in the physical domain in only about two seconds.

Another SD-OCT protocol is called "high-definition 5-line raster" scans (i.e., HD-5LR scans, which was mentioned in Sec. 2.4.3), which consists of 4096 A-scans penetrating a 2 mm axial depth for each scanning line and includes a few adjustable parameters, such as the length, angle, and distance between scanning lines (by default, an HD B-scan covers 9 mm in width, and the spacing between each two successive B-scans is 0.25 mm). HD-5LR scans provides better image quality by repeatedly scan-

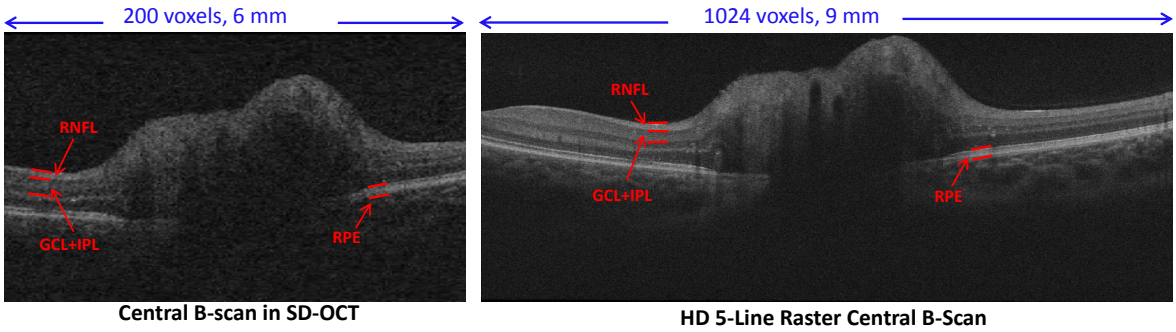

Figure 3.1: Central B-scans from a SD-OCT volume (left) and an HD-5LR scan (right). Retinal nerve fiber layer (RNFL), ganglion cell - inner plexiform layer (GCL+IPL), and retinal pigment epithelium (RPE) complex are indicated in both central B-scans. The HD-5LR B-scan has better image quality than the regular SD-OCT B-scan.

ning five parallel linear regions and averaging these repeated scans to construct five individual HD B-scans. HD-5LR scans support better image quality of each B-scan compared to the B-scans in the regular SD-OCT volumes, but a HD-5LR scan can only support "five" B-scans, which are not sufficient to construct a true volumetric image. Therefore, it results in a very interesting new topic of how to combine the 2D detailed information from the HD B-scans and 3D contextual information from the corresponding SD-OCT volumes. Fig. 3.1 shows the resolution difference between two central B-scans from an SD-OCT and HD-5LR scan, and Fig. 3.2 is an example that shows the physical mapping of each HD-5LR B-scan in the corresponding SD-OCT volume.

3.2 Challenges of Automated Retinal Layer Segmentation in OCT

Developing reliable, automated methods to quantitatively measure the retinal properties has been a popular topic in the field of OCT image processing because of the tremendous advantages. Compared to manual tracing, automated methods can reduce not only processing time but also the inter- and intra-observer variability.

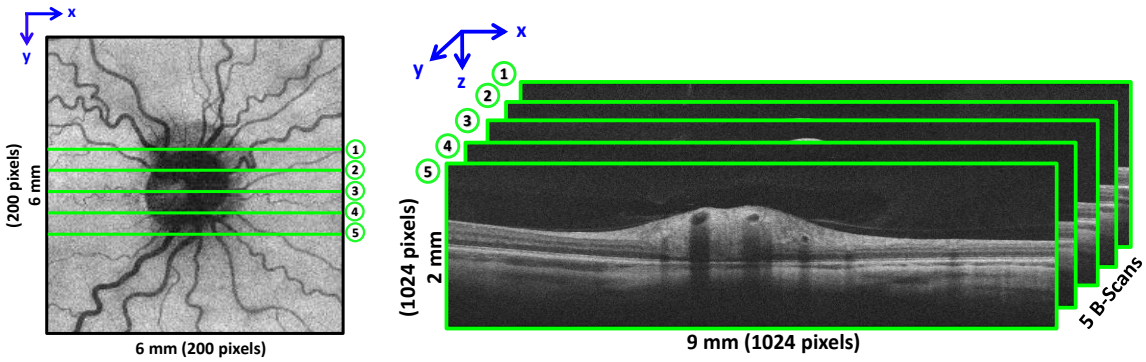

(a) (b)

Figure 3.2: The matching relationship between a 5-line raster scan and its corresponding SD-OCT image. (a) RPE projection image from the SD-OCT image, and (b) HD 5-line raster scan.

Because of the fact that different retinal tissue and nerve cells have distinct reflective properties in the OCT images, many automated layer-segmentation algorithms are designed to distinguish the retinal layers by identifying their varied intensity values. For example, the retinal nerve fiber layer (RNFL) has much higher intensity reflection than the ganglion cell inner plexiform layer (GCIPL) has in the inner retina, and the retinal pigment epithelium (RPE) complex consists of two bright bands at the bottom part of the retina (Fig. 3.1). These physiological properties are generally very useful prior information for program developers to make initial assumptions to simplify an algorithm's complexities. Although OCT images demonstrate the potential for automated analysis by computer algorithms, the program developers are still facing a few inherent challenges of segmenting retinal layers in these OCT images [31]:

1. Speckle noise [32,33] – It is a type of granular noise and an intrinsic characteristic of coherent images. Speckle noise occurs due to several reasons. In general, multiple scattered photons with different scattering angles is a major cause, and the physical parameters of the OCT machines (such as the angle of the incident light, the aperture size of the signal detector, etc.) also have some

degrees of influence. Speckle noise degrades the quality of the OCT images and blurs the boundaries among retinal layers. Suppressing speckle noise is typically the first step of segmenting the retinal layers in the OCT images from the perspective of automated retina-layer-segmentation algorithms.

2. Signal attenuation at deeper retinal layers – OCT machines acquire images by receiving the signal reflection from the tissue and comparing it to the referenced signal. When the signal detector receives weaker reflection from the target areas, the image intensity/quality decreases. This situation happens in cases of optic disc swelling, in particular because it is more difficult for the incident OCT signal to fully penetrate the entire swollen retina. Image shadows are often observed around the region near the Bruch's membrane opening (BMO), and this artifact causes most of the automated methods to overestimate the true BMO region size [34].

3. Shadows from blood vessels – When the OCT machines are scanning the retinal tissue under blood vessels, the different scattering properties between the retinal tissue and blood vessels cause the tube-shaped shadows to manifest in the images. These blood vessel shadows obscure and disjoint the boundaries of the retinal layers, which can possibly make the automated layer-segmentation algorithms locally fail.

4. Motion artifacts [35,36] – A scanning beam traveling from an OCT machine light source to the retinal tissue and then scattering back to the reflection detector needs a certain time to finish the entire itinerary. Although the signal traveling time is relatively short, it is still possible for a patient's eyeball to move or quiver during image acquisition. These movements affect the continuity of B-scan compositions in OCT images and appear in a form of sections of successive B-scans shifting in the same direction together.

Overall, to cope with these artifacts, the layer segmentation algorithms working in 3D (which means the algorithms consider the entire OCT volume as one input) are more robust than algorithms working in 2D (which means the algorithms perform segmentation on individual B-scan separately and then merge the results together). Compared to the 2D algorithms, the 3D algorithms take the advantage of using the contextual information to avoid local segmentation failures when the artifacts locally affect the SD-OCT image quality or the retinal structure dramatically deforms in certain regions.

3.3 Automated Methods of Retinal Layer Segmentation in OCT

Since the introduction of commercially available OCT machines, the development of automated layer segmentation methods in OCT images has become an important topic. Compared to manually tracing the retinal layers in the OCT images, automated methods have advantages, such as improved time-efficiency, and low intra-/inter-observer variability. Based on relevant retinal segmentation results, quantitative measurements can be reliably computed and provide ophthalmologists with a more objective reference. For example, the thinning of GCIPL could imply that the ganglion cells have been dying; with an accurate retinal layer segmentation, ophthalmologists can not only qualitatively observe the cell loss in the OCT images (i.e., a thinning retina) but also quantitatively measure the amount of the cell layer has atrophied within the precision of a micro-meter. By quantitatively knowing how much cell loss, ophthalmologists can more precisely adapt their therapies based on treatment results over time.

To segment retinal layers in OCT images, intensity peak detection along each A-scan is an early common method, and the process usually follows these steps:

1. Suppress speckle noise using low-pass filtering [37], median filtering [38–42], nonlinear anisotropic diffusion filtering [43], or Gaussian smoothing filtering [42,

44].

2. Apply intensity peak (and/or valleys) detection for each individual A-scan [37–44].

3. Post-process to interpret and/or integrate pre-detected intensity peaks using Markov boundary model [38], prior clinical knowledge of the strengths from a kernel response [39], coherence information of retinal layer structure [43], adaptive thresholding techniques [40, 41], dynamic programming [42], or averaging multiple nearby A-scan picks [44].

4. Smooth segmented layers using cubic B-splines [38], linear interpolation [43], or polar interpolation [40, 41].

Intensity-based layer segmentation approaches also have some variability, which may include using the correlation between adjacent A-scans instead of searching and mapping each A-scan individually [45], non-denoising approaches using an intensity-based iterative thresholding technique [46], with prior knowledge of vessel sections, and a layer segmentation using a Canny edge detector [47]. The main limitation of the intensity-based approaches is that the texture information is not totally considered, so these approaches are sensitive to speckle noise, blood vessel shadows, and motion artifacts (Sec. 3.2).

In addition to the intensity-based approaches (as discussed above), active-contours-based methods [48–50], machine-learning-based methods [51–53], and shape models [54, 55] are also common algorithms for segmenting the OCT retinal layers. Although all these methods are capable of extracting the retinal structure, shape, and regional texture information in 2D or partially in 3D, they also face additional challenges, such as high computational complexity, requiring a ground truth for the training processes, less flexibility because the testing images need to be highly similar to the training images, not fully automated algorithms, difficulties in selecting clinically

meaningful features, and not truly considering the global 3D information from the OCT volumes.

Graph-based searching, generally speaking, is a more robust option for addressing the segmentation problem in OCT images by applying an implicit transformation from pixels/voxels in an image to nodes in a graph. Classic graph algorithms (for example, dynamic programing and Dijakstra's method) for finding the shortest path have been applied to segment retinal boundaries in OCT B-scans [56–58]. Even though these approaches work and have been tested on 3D OCT volumes, they are actually not "true 3D" approaches due to the fact that these algorithms only process individual B-scan separately and then merge the segmentation results together rather than considering the entire SD-OCT volume as a complete input.

When it comes to the "true 3D" retinal layer segmentation, Garvin et al. [59] first applied a 3D graph-theoretic approach [16, 60] to simultaneously detect multiple retinal surfaces in SD-OCT macular scans. Later, Lee et al. [61] introduced a multi-resolution technique to accelerate the processing time and extended this graph-theoretic algorithm to SD-OCT optic nerve head (ONH) scans. Although the graph-theoretic algorithms require a few parameters as inputs to constrain the behaviors of the output surfaces, the step of parameter selection is generally straightforward and user-friendly for experienced developers based on the regularity of the retinal structure properties. In addition, the graph-theoretic algorithms compute the mathematically optimal surfaces based on the pre-designed input cost-functions, so the layer segmentation results can be precisely performed when the cost-functions are well-defined. Initially, these input cost images for the graph search algorithms were designed by domain experts. Recently, Antony et al. [62] proposed a machine-learning method considering texture information to create probability maps, which can be converted into the cost functions, and this technique makes the processes of designing the input cost functions easier and more efficient. A year later, Antony et al. [63] tested the

robustness of their method in the OCT images of humans, mice and canines. Besides improving the method for designing cost images, Song et al. [64] proposed a novel idea of incorporating the shape and context prior knowledge to increase the algorithm's robustness [16]. In the graph domain, the shape-prior and the context-prior terms can penalize the local change from the expected retinal shape and surface properties. By adding the prior information, the graph-theoretic algorithm has added the ability to entirely consider both global and local optimization and achieves better robustness. More technical details about how to construct graphs in a graph-theoretic algorithm and its usage will be discussed in the next section.

3.4 Graph-Search Algorithm

To achieve the "true 3D" consideration, a particular kind of graph-search algorithm [16, 60, 64] was used in this doctoral study. Garvin et al. [59] first applied this graph-theoretic algorithm [16] to the field of OCT image segmentation. This method has the ability to simultaneously compute the globally optimal solutions for all the target retinal surfaces based on the input cost-function images and proper surface feasibility constraints. It converts the original image layer segmentation problem into an optimization problem of labeling feasible minimum-cost closed sets in newly constructed graphs. To build the graphs, the input cost images are transferred into the node costs, and the surface feasibility constraints are transformed to the rules of graph node connections. After the graph is appropriately generated, minimum-cost closed sets are computed by applying a minimum s-t cut algorithm [16, 60]. More details regarding to the surface feasibility constraints and surface set costs are provided in the following two subsections.

3.4.1 Smoothness and Surface-Interaction Constraints

Assume that a volumetric image can be described as $\mathcal{I}(\mathbf{x}, \mathbf{y}, \mathbf{z})$ with dimensions $X \times Y \times Z$, and the target surface $\mathcal{S} : (x, y) \rightarrow \mathcal{S}(x, y)$ is a terrain-like surface in

$\mathcal{I}$ intersecting only one voxel of each column, $Col(x, y)$, is parallel to the $\mathbf{z}$-axis (for example, an A-Scan in a SD-OCT volume) and spans the entire $\mathbf{x} \times \mathbf{y}$ domain. When $\mathcal{S}(x, y)$ is regarded "feasible," the smoothness constraints ($\Delta_{\mathbf{x}}, \Delta_{\mathbf{y}}$ at $\mathbf{x}, \mathbf{y}$ directions, respectively) are applied to guarantee the surface connectivity within a certain degree of freedom, which means if $\mathcal{I}(x, y, z_1)$ and $\mathcal{I}(x+1, y, z_2)$ are two adjacent voxels on a feasible surface along the $\mathbf{x}$ direction then $|z_1 - z_2| \leq \Delta_{\mathbf{x}}$ [on the other hand, along the $\mathbf{y}$ direction, for $\mathcal{I}(x, y, z_1)$ and $\mathcal{I}(x, y+1, z_2)$ then $|z_1 - z_2| \leq \Delta_{\mathbf{y}}$]. Further, Garvin et al. [59] demonstrated that $\Delta_{\mathbf{x}}, \Delta_{\mathbf{y}}$ can be varied among different adjacent voxel pairs, so the smoothness constraint can be written as

$$-\Delta^{u}_{\{(x_1,y_1),(x_2,y_2)\}} \leq \mathcal{S}(x_1, y_1) - \mathcal{S}(x_2, y_2) \leq \Delta^{l}_{\{(x_1,y_1),(x_2,y_2)\}},$$

where for each adjacent $Col(x_1, y_1)$, $Col(x_2, y_2)$ pair, $\Delta^{l}_{\{(x_1,y_1),(x_2,y_2)\}}$ and $\Delta^{u}_{\{(x_1,y_1),(x_2,y_2)\}}$ represents the maximum increase and decrease in the z-direction, respectively.

When there are more than one target surfaces in the segmentation problem, in addition to the previously discussed smoothness constraints for each individual target surface, the surface-interaction constraints are also introduced to limit the minimum (δ^l) and maximum (δ^u) distant relationship between each two neighbor target surfaces for all the A-scans [16]. Take a two surface segmentation for example. Assume that surface $\mathcal{S}_i(x, y)$ is above $\mathcal{S}_j(x, y)$, the surface-interaction constraints at each $Col(x, y)$ can be written as

$$\delta^l(x, y) \leq \mathcal{S}_i(x, y) - \mathcal{S}_j(x, y) \leq \delta^u(x, y),$$

where $\delta^l(x, y)$ is the minimum distance constraint for the $\mathbf{z}$-value of a voxel on feasible surface $\mathcal{S}_i(x, y)$ minus the $\mathbf{z}$-value of a voxel on feasible surface $\mathcal{S}_j(x, y)$; $\delta^u(x, y)$ is the same idea but for the maximum distance constraint between feasible surfaces $\mathcal{S}_i(x, y)$ and $\mathcal{S}_j(x, y)$.

3.4.2 Cost of Feasible Surfaces

The cost functions for the graph-theoretic algorithm can be decomposed into edge-based and region-based cost functions. A typical edge-based cost image $\mathcal{I}_{c_{\mathcal{S}}}(\mathbf{x}, \mathbf{y}, \mathbf{z})$ is designed to reflect the voxels on the target surface with very low cost values obtained from the first and/or second derivatives of the image intensity function. For surface $\mathcal{S}_i(x, y)$, the edge-based cost can be described as $C_{\mathcal{S}_i(x,y)} = \sum_{\{(x,y,z)|z=\mathcal{S}_i(x,y)\}} \mathcal{I}_{c_{\mathcal{S}_i}}(x, y, z)$. For a multiple n surface set $\{\mathcal{S}_1(x, y), \ldots, \mathcal{S}_n(x, y)\}$, the total edge-based costs can be computed by $C_{\{\mathcal{S}_1(x,y),\ldots,\mathcal{S}_n(x,y)\}} = \sum_{i=1}^{n} C_{\mathcal{S}_i(x,y)}$.

On the other hand, the region-based cost image $\mathcal{I}_{c_{\mathcal{R}}}(\mathbf{x}, \mathbf{y}, \mathbf{z})$ is designed to reflect the unlikeness of a voxel belonging to particular regions. Following the above multiple n surface example, the number of the regions will be $n + 1$ regions. For region $\mathcal{R}_i$, the region cost can be written as $C_{\mathcal{R}_i} = \sum_{(x,y,z)\in\mathcal{R}_i} \mathcal{I}_{c_{\mathcal{R}_i}}(x, y, z)$. Therefore, the region costs of the entire n surfaces is $C_{\{\mathcal{R}_0,\ldots,\mathcal{R}_n\}} = \sum_{i=0}^{n} C_{\mathcal{R}_i}$. Therefore, the entire cost of n surface set can be expressed as:

$$\begin{aligned} C_{Total} &= C_{\{\mathcal{S}_1(x,y),\ldots,\mathcal{S}_n(x,y)\}} + C_{\{\mathcal{R}_0,\ldots,\mathcal{R}_n\}} \\ &= \sum_{i=1}^{n} C_{\mathcal{S}_i(x,y)} + \sum_{i=0}^{n} C_{\mathcal{R}_i} \end{aligned} \tag{3.1}$$

3.4.3 Soft Constraints with Shape-Prior Knowledge

Although Garvin et al. [59] showed that the smoothness and surface-interaction constraints can be variables at arbitrary $Col(x, y)$ and its adjacent neighbors, the method did not grant the penalty of the deviation inside the allowed constraints. Under this circumstance, only hard constraints were used so the surfaces can only be feasible or not feasible.

A modified version of the graph-search algorithm is to add extra soft constraints based on some given prior shape information [64]. The cost of the surface set will be penalized by a convex function $f(h)$ if the change of the surface is deviated from

a statistic model (i.e., the mean shape in this case). Therefore, the shape deformation inside the shape constraints can be suppressed. Assume that the mean shape prior is $m_{(x_1,y_1),(x_2,y_2)}$ for each two adjacent $Col(x_1,y_1), Col(x_2,y_2)$ column-pair on a feasible surface $\mathcal{S}_i(x,y)$, the cost of the shape term can be written as $C_{Sp_i} = \sum_{\{(x_1,y_1),(x_2,y_2)\in\mathcal{N}_c\}} f(\mathcal{S}_i(x_1,y_1) - \mathcal{S}_i(x_2,y_2) - m_{(x_1,y_1),(x_2,y_2)})$, where $\mathcal{N}_c$ represents a set of neighboring columns. So, the cost of the entire n surface set can be rewritten as:

$$\begin{aligned} C_{Total} &= C_{\{\mathcal{S}_1(x,y),\ldots,\mathcal{S}_n(x,y)\}} + C_{\{\mathcal{R}_0,\ldots,\mathcal{R}_n\}} + C_{\{\mathcal{S}_{Sp_1},\ldots,\mathcal{S}_{Sp_n}\}} \\ &= \sum_{i=1}^{n} C_{\mathcal{S}_i(x,y)} + \sum_{i=0}^{n} C_{\mathcal{R}_i} + \sum_{i=1}^{n} C_{\mathcal{S}_{sp_i}}. \end{aligned} \tag{3.2}$$

In order to represent the cost term, adding the extra weighted arcs to the s-t cut formulation of the graph is needed. Take a 2D graph for example: Assume that the smoothness constraint in the $\mathbf{x}$ direction is a constant $\Delta_{\mathbf{x}}$, the intra-column and inter-column arcs can be connected with the arc weight of $+\infty$ (i.e., the hard constraints). When the mean shape prior $(m_{(x_1,x_2)})$ is given for each two adjacent $Col(x_1), Col(x_2)$ column-pair for a feasible boundary $\mathcal{S}(x)$, the soft constraints are added by penalizing the shape deviation from the mean shape, where the shape prior penalty can be expressed by $f(\mathcal{S}(x_1) - \mathcal{S}(x_2) - m_{(x_1,x_2)})$. Let $h = \mathcal{S}(x_1) - \mathcal{S}(x_2) - m_{x_1,x_2}$, so the shape prior penalty can be rewritten as $f(h)$. The second derivative of the convex function $f(h)$ can be expressed as $[f(h)]'' = [f(h+1) - f(h)] - [f(h) - f(h-1)]$, and the first derivative is $[f(h)]' = f(h+1) - f(h)$. For each $-\Delta_{\mathbf{x}} < h < \Delta_{\mathbf{x}}$, if $[f(h)]' \geq 0$, an arc is added from $node(x_1,z)$ to $node(x_2, z - m_{(x_1,x_2)} - h)$ with an arc weight of $[f(h)]''$. if $[f(h)]' < 0$, and an arc is added from $node(x_2,z)$ to $node(x_1, z + m_{(x_1,x_2)} + h)$ with an arc weight of $[f(h)]''$.

Assume that the smoothness constraint is one (i.e $\Delta_{\mathbf{x}} = 1$), Fig. 3.3 (a) illustrates the 2D graph construction with hard constraints. If the shape prior now is given and known a horizontal line, the mean shape change will be 0 (i.e., $m_{x_1,x_2} = 0$), Fig. 3.3 (b) shows the graph construction with both hard and soft constraints.

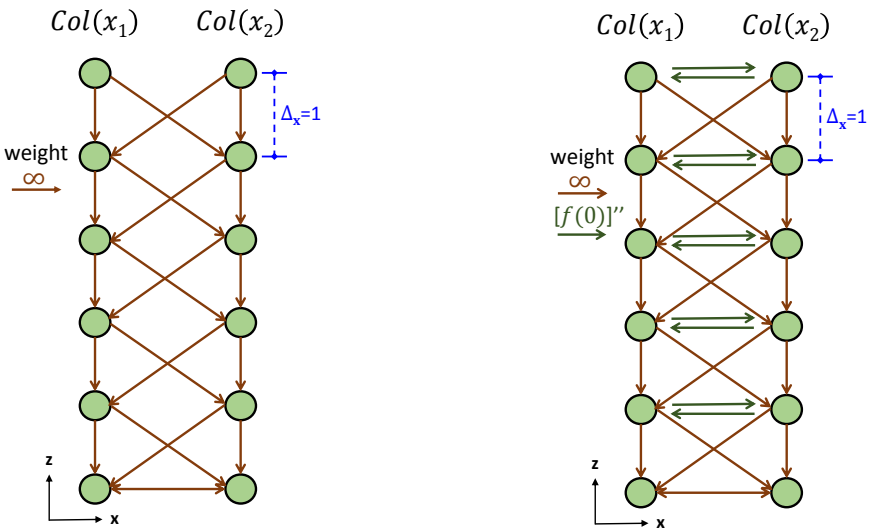

(a) (b)

Figure 3.3: A 2D example of the graph construction with arc weights. (a) Hard constraints with the smoothness constraint $\Delta_{\mathbf{x}} = 1$. (b) Adding soft constraints with the mean shape change $m_{x_1,x_2} = 0$, where the source and sink nodes are not shown.

3.5 Segmentation of Bruch's Membrane Opening in OCT

Although the original design of the graph-search method was to segment a 1D boundary passing throughout an entire $\mathbf{x}$ direction in a 2D image or to segment a 2D surface completely covering the $(\mathbf{x}, \mathbf{y})$ plane in a 3D volume, this method can be extended to segment the boundary of a closed circular region in 2D or the surface of a 3D tubular object [16,65]. A good application for this extension is to solve the Bruch's membrane segmentation problems in OCT images [66]. In an SD-OCT retinal pigment epithelium (RPE) complex *en-face* image (which is a type of intensity-projection image between two surfaces), the projected Bruch's membrane opening (BMO) is an oval-like closed region. To apply the graph-search algorithm to segment the BMO, the RPE *en-face* image needs to be unwrapped from the center. In this unwrapped image, the original circular BMO close contour is transformed to a horizontal-like boundary. Here, the 2D graph-search algorithm for the single boundary detection

can be applied. After converting the horizontal segmented boundary back to the original RPE *en-face* image domain, the BMO contour is segmented. More details can be found in the work of Hu et al. [66]. Recently, Antony et al. proposed an iterative graph-search approach to segment the BMO and surrounding surfaces in the SD-OCT volumes of glaucoma patients [67].

3.6 Summary

OCT, which has the ability to support 2D/3D cross-sectional information, is a relatively new technique of acquiring retinal images in ophthalmology. Based on appropriate layer segmentations, measurements from the retina (such as the peripapillary RNFL and TR thicknesses, the total ONH volumes, and the pRPE/BM shape measure) help ophthalmologists have more objective references to trace retinal longitudinal changes. However, artifacts in OCT images dramatically increase the difficulties of developing robust segmentation algorithms in an automated fashion. Common methods of segmenting retinal layers have been addressed in this chapter, and a particular type of graph-theoretic algorithms was introduced to provide a "true 3D" solution with the input of pre-designed cost function images and surface-feasibility constraints. This graph-search method converts the original layer segmentation problem in the image domain into a minimum closed-set problem in the graph domain. The following chapters will elaborate more details about how to extend this method to fit the need of segmenting swollen optic discs.

CHAPTER 4
AUTOMATED RETINAL LAYER SEGMENTATIONS IN SWOLLEN OPTIC DISCS USING SD-OCT (AIM 1)

4.1 Introduction

Papilledema is a specific term to reflect optic disc edema due to elevated intracranial pressure, which may indicate fatal conditions [1], so it has been an important topic in modern ophthalmology to have a rapid, reliable method to measure its severity. A well-known qualitative method is the Frisén scale scheme [3], which assesses the severity of papilledema using a grade from 0 (normal) to 5 (severe) by neuro-ophthalmologists examining the visible features of the optic nerve head (ONH) and the peripapillary retinal region from direct funduscopic observation or digital color fundus photographs. Although the Frisén grading scheme has became a clinical standard, major limitations (such as high intra/inter-observer variability, specific expertise in interpreting retinal features, tedious processing steps) are still unavoidable [4].

On the other hand, the newly introduced OCT techniques [8] impressively enable quantitative measurements of the retina (e.g., the thickness, volume, and shape). Generally speaking, current commercial SD-OCT machines only need a few seconds to acquire one retinal scan (for example, around 2.4 seconds per scan for the Cirrus HD-OCT using the 512×128 Macular protocol) without invasive procedures, and the accompanying segmentation algorithms have the ability to compute the peripapillary retinal nerve fiber layer (pRNFL) and total retina (pTR) thicknesses, which are quantitative metrics and are potentially reasonable alternatives to the qualitative Frisén scheme grades [4, 9, 10].

However, the layer-segmentation algorithms from the commercial SD-OCT devices are designed to work in cases of non-swollen retina and often fail to output dependable results when the optic disc swelling is more severe than mild [11,12]. A possible reason to explain the high failure rate is that the "iceberg shape" of the swollen optic disc commonly violates the pre-defined thickness constraints among the retinal layers in

these commercial SD-OCT segmentation algorithms. In addition, these algorithms only find the boundaries of the desired retinal layers on each B-scan individually rather than simultaneously considering the complete 3D retinal structure. When the retinal tissue is obscure and/or the retinal profile rapidly changes among B-scans in the input OCT images, the performance of these segmentation algorithms is highly unstable. Therefore, a 3D segmentation algorithm, which can utilize the contextual benefits of considering neighbor B-scans, potentially has a better capability for accurately identifying retinal layers in severe swollen optic discs than traditional 2D algorithms. An existing 3D graph-search method had been successfully applied to segment the non-swollen retinal layer in the SD-OCT images [16, 59, 61], but the original setting does not work for severely swollen optic discs.

Thus, the **objective of Aim 1** in this doctoral work is to develop automated algorithms which are capable of reliably segmenting retinal layers for both normal and swollen optic discs in SD-OCT images (which includes both the ONH HD-5LR and volumetric scans) by re-designing the input cost function images and surface-constraints using an existing graph-search algorithm. Having robust layer segmentation algorithms is important, because all the future retinal measurements/features in this thesis will depend on accurate segmentation results. Aim 1 has three sub-goals: 1) to provide the retinal layer segmentation in HD-5LR scans, 2) to provide the retinal layer segmentation for volumetric scans, and 3) to recover the segmentation when the inner retinal tissue gets truncated due to the severe optic disc swelling. Aim 1 provides a solid foundation for the following research aims, which include the Bruch's membrane opening (BMO) detection (Aim 2), 2D/3D pRPR/BM shape model constructions and measurements (Aim 3), and retinal feature computations as well as machine learning framework for estimating the papilledema severity (Aim 4).

For the **publication of Aim 1**, the proposed SD-OCT volumetric segmentation method, which works for both normal and swollen optic discs, was first published

in [7], which will be elaborated in Section 7.2. Also, studies [11, 12, 68] used both accompanying algorithms of the commercial SD-OCT devices (Zeiss, Cirrus) and the proposed segmentation algorithm to segment swollen optic discs. Compared to the commercial algorithms, the proposed algorithm has demonstrated that its segmentation failure rates are noticeably lower [11, 12]. The method for correcting the underestimated SD-OCT ONH measurement was published in [69].

4.2 Two-Dimensional Layer Segmentation in Swollen Optic Discs Using HD-5LR Scans

In this section, an automated algorithm is designed for segmenting the inner limiting membrane (ILM) and the top as well as bottom boundaries of the retinal pigment epithelium complex (called topRPE and botRPE boundaries for simplification) in swollen optic discs on individual B-scans using HD-5LR scans (Fig. 4.1). In this scenario, the 2D version of the graph-search algorithm [16] is a suitable approach to achieve this goal. With appropriate pre-processing of the boundary feasibilities based on the prior knowledge of the retina, the computed theoretically optimal minimum-cost-closed sets are matched with the desired boundary segmentations in the input OCT B-scans. In other words, the retinal layer boundaries are the theoretically optimal solutions of being labeled based on the input cost-function images. Boundary feasibilities include two types of constraints: 1) the smoothness constraint, which limits the local changes in the depth direction (i.e., the A-scan direction) for each given boundary to a specified range, and 2) boundary interaction constraint, which limits distances between pairs of neighboring boundaries for each A-scan to a specified range. Theoretical details about these constraints were discussed in Section 3.4.

4.2.1 Layer Segmentation in 2D – No Prior Information of Bruch's Membrane Opening

The task here is to segment the ILM, topRPE and botRPE boundaries in the central three B-scans from the input HD-5LR B-scans (2D layer segmentation) without

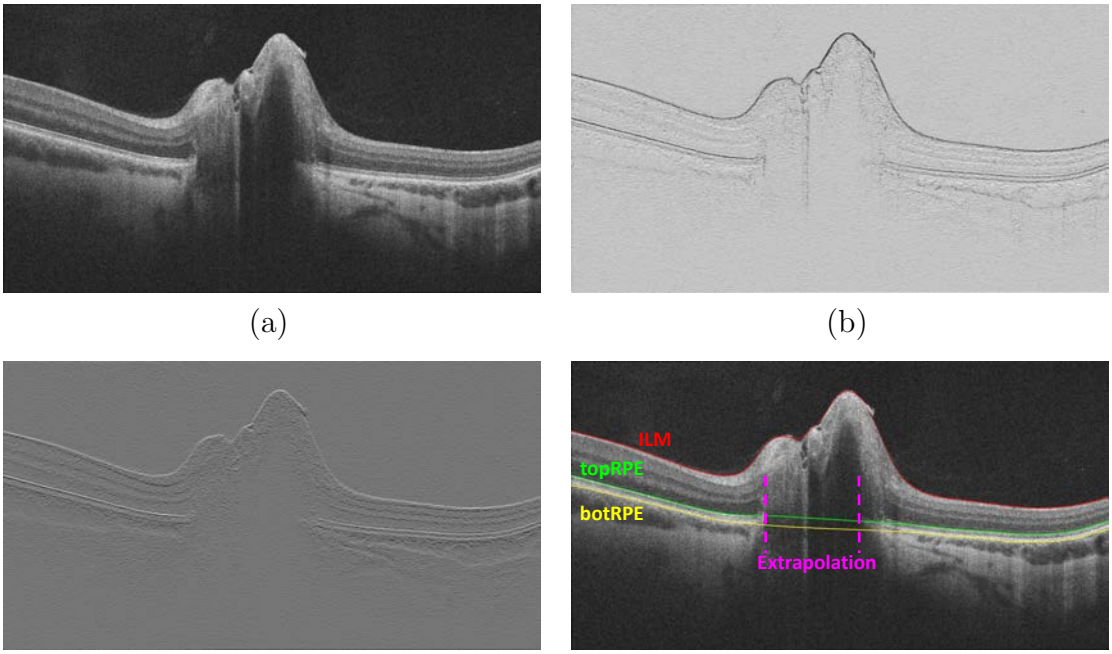

Figure 4.1: Layer segmentations of the eye with optic disc edema in an HD raster B-scan. (a) The central B-scan of an HD-5LR scan in the original resolution. (b) The D-to-B cost image for ILM [i.e., the red boundary in (d)] and topRPE [i.e., the green boundary in (d)]. (c) The B-to-D cost image for botRPE [i.e., the yellow boundary in (d)]. (d) Layer segmentation results.

prior information of the Bruch's membrane opening (BMO). The automated segmentation is developed using a multi-resolution technique, as described in the following steps:

1. Extract the middle three B-scans from the input HD-5LR scan.

2. Segment the retinal layers for each extracted B-scan in an image that is down-sampled by 16 in the **z** direction using the following steps:

   (a) Down-sample the input B-scan by 16 in the **z** direction.

   (b) Smooth the downsampled image and use a Sobel filter to generate a dark-to-bright (D-to-B) boundary cost image.

(c) Perform the 2D graph-search algorithm with the input D-to-B cost images to simultaneously segment both the ILM and topRPE boundaries.

(d) Use the thin-plate-spline (TPS) interpolation algorithm [70] to smooth the pre-segmented topRPE boundary and "truncate" the region above the smooth boundary. (Note: "truncate" means assigning very high costs in this region in the cost image). The cost image of the topRPE boundary is then updated.

(e) Perform the 2D graph-theoretic algorithm again on the updated D-to-B cost image for the topRPE. The layer segmentation in the down-sampled-by-16 resolution is complete.

3. Up-sample the previously obtained segmentation results into the image down-sampled by 8 and perform the following steps:

(a) Downsample the input B-scan by 8 in the **z** direction.

(b) Smooth the downsampled B-scan and compute the D-to-B cost image using a Sobel filter and the bright-to-dark (B-to-D) cost image using an inverse Sobel filter.

(c) Based on the topRPE segmentation results from the previous resolution, truncate the outer retina in the D-to-B cost image.

(d) Perform the 2D graph-theoretic algorithm to only segment the ILM with the modified D-to-B cost image.

(e) Based on the segmented ILM, truncate the inner retina in both D-to-B and B-to-D cost images.

(f) Perform the 2D graph-theoretic algorithm again to simultaneously segment both topRPE and botRPE boundaries using the updated D-to-B and B-to-D cost images.

(g) Use the TPS algorithm to smooth the segmentation results.

4. Repeat the same processes of refining the segmentation results at higher resolutions until the segmentation is finally performed at the original image resolution.

Fig. 4.1 is an example of a central HD-5LR B-scan and its segmentation results.

4.2.2 Layer Segmentation in 2D – Given Two Bruch's Membrane Opening Points

In this task, two BMO points are manually determined. The goal is the same as what was discussed in the previous section (i.e., to segment ILM, topRPE, and botRPE boundaries for each input HD raster B-scan), but the segmented botRPE boundary is expected to pass through (or at least very close to) the given BMO points. The segmentation steps in this task are very similar to the steps that have been discussed in the previous section. The only difference is that since the positions of the two BMO points for each input HD B-scan are given, there exists more flexibility to manipulate the cost images by imposing very low-cost values to bias the cost image such that the layer segmentation prefers to pass through the desired regions. Fig. 4.2 shows another example of the same B-scan from Fig. 4.2.1 but with two given BMO points considered.

4.2.3 Conclusions

Although there is no particular measurement in this section, it is very important to have the ability to segment retinal layers in HD-5LR scans with and without given BMO points, because this segmentation is a necessary step for future usage, including the BMO segmentation described in Aim 2 (Chapter 5) and the pRPE/BM shape model generation described in Aim 3 (Chapter 6). This segmentation algorithm also has been tested and qualitatively validated in the Idiopathic Intracranial Hypertension Treatment Trial (IIHTT) longitudinal dataset, for which the failure rate was 2.4% (19/782 scans). The limitation of this algorithm is that the outer retina must

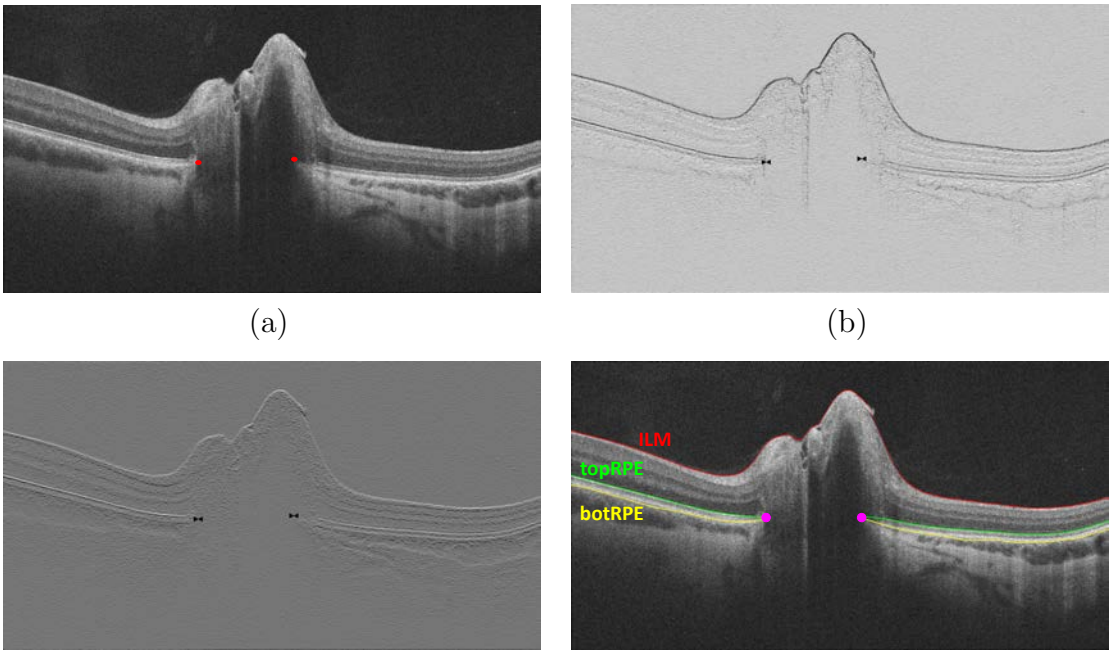

(a) (b) (c) (d)

Figure 4.2: Layer segmentations of the eye with optic disc edema in HD raster B-scan with two given BMO points. (a) The central B-scan. (b) The modified D-to-B cost image. (c) The modified B-to-D cost image. (d) Layer segmentation results with the two given BMO points (pink dots).

completely appear in the HD-5LR B-scan, because the botRPE is one of the first boundaries to be segmented in multi-resolution processes. When the botRPE is not correctly identified at low resolution, the errors propagate to higher resolutions and cause a segmentation failure.

4.3 Three-Dimensional Layer Segmentation in Swollen Optic Discs Using SD-OCT Volumes

For this goal, the focus in how to extend the previous discussed 2D layer segmentation algorithm into a 3D version. The target surfaces are the ILM, the bottom surface of the RNFL (called botRNFL), the top and bottom surfaces of the RPE complex (i.e., topRPE and botRPE in the previous section). A 3D version of the graph-search algorithm [16] is used to segment the target surfaces, and the surface feasibilities are

defined by 1) smoothness constraints, which limit local changes along the **z** direction for each desired surface to a specified range, and 2) surface interaction constraints, which limit the minimum and maximum distances between pairs of surfaces for each $\mathbf{x}-\mathbf{y}$ column to a specified range (more details are in Section 3.4).

4.3.1 Three-Dimensional Cost Function Image Design

The processes of generating cost images in 3D can be easily extended from 2D by using the 3D Gaussian filers for smoothing the input SD-OCT images and applying 3D Sobel filters ($3\times3\times3$) for computing the D-to-B and B-to-D cost function images.

4.3.2 Three-Dimensional Layer Segmentation

The steps in the 3D automated segmentation algorithm are very similar to the 2D case, except for the usage of 3D cost function images as the inputs. The major difference is that the D-to-B cost images are used for detecting the ILM and topRPE surfaces and the B-to-D cost images are good for segmenting the botRNFL and botRPE surfaces. Use of a multi-resolution technique is important in the 3D processing, because the surface searching ranges can be dramatically reduced by trimming the input cost function images based on the segmentation results at lower image resolution. Under these circumstances, the computational time can be significantly decreased (from several hours to minutes). Fig. 4.3 (a) is the central B-scan of the SD-OCT volume from the same subject in the previous section, and Fig. 4.3 (b) shows its layer segmentation results.

On the other hand, motion artifacts often occur during SD-OCT imaging and appear in the form of retinal tilting in B-scans. To set up a regular reference frame, the segmented botRPE surface will be considered as a reference surface. The entire retina in the SD-OCT volume is flattened by realigning each A-scan until the reference surface is flat. Although the retinal flattening process essentially does not change any quantitative measurement results, the images are more consistently aligned [Fig. 4.3

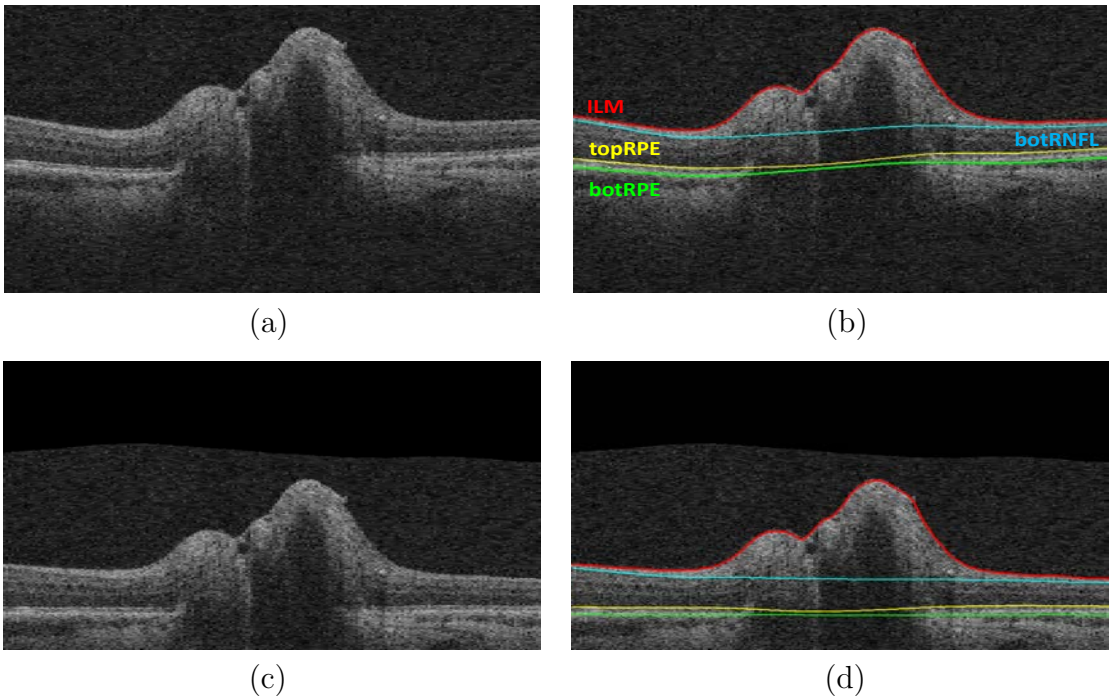

Figure 4.3: Layer segmentation of the eye with optic disc edema in a SD-OCT Volume. (a) The input central B-scan. (b) Layer segmentation results of the input B-scan. (c) The flattened central B-scan. (d) Layer segmentation results of the flattened B-scan.

(c) and (d)] and more readily used for registration in Section 5.2.2. More examples will be shown in Section 7.2, including 3D visualizations for different degrees of optic disc swelling (Fig. 7.2).

4.3.3 Conclusions

The focus in this section is on the development of a methodology which has the ability to automatically segment severely swollen retina considering 3D contextual information, using a graph-search algorithm. This automated segmentation approach is very important, because all the retinal measurements/features that are computed using SD-OCT volumetric images depend on these segmentation results. To the best of my knowledge, there is still no commercial software that has the ability to reliably process the layer segmentation problems when the optic disc is severely swollen [11,12].

Section 7.2 has more details about the computations and correlations among the common OCT measurements [including the ONH volume, peripapillary retinal nerve fiber layer (pRNFL) and total retina (pTR) thicknesses]. This 3D segmentation algorithm also has been tested and qualitatively validated in the IIHTT longitudinal dataset. Among the 1564 ONH-centered SD-OCT volumetric scans, 37 scans are excluded due to a failure of the segmentation (i.e., a failure rate of 2.4%). Again, as we previously discussed in Section 4.2.3, most of the segmentation failures are caused by the fact that the botRPE surface, which is one of the most important surfaces in the multi-resolution processes, is not complete in the SD-OCT volumes.

4.4 ILM Recovery for Incomplete SD-OCT Volumes

SD-OCT enables the 3D cross-sectional information from the ONH region to be acquired and supports volumetric measurements based on the retinal layer segmentations. However, in cases of severe optic disc edema, the inner retina deforms and becomes too swollen to be fully enclosed by the SD-OCT image window in the **z** direction, causing the "top of the iceberg" to be cut off. In such scans, the border of the ILM is missing from the portion of the nerve projecting the furthest into the vitreous. The goal in this task is to develop an automated methodology to detect and recover the missing part of the ILM so that the optic-nerve-head (ONH) volumetric measurement can be corrected from the underestimation.

4.4.1 Thin-Plate-Spline (TPS) Interpolation

A thin-plate-spline (TPS) interpolation algorithm [70] is used to help recover the missing parts of the ILM in incomplete SD-OCT volumes. The ILM-recovery approach is developed by accomplishing the following steps:

1. Detect the cut-off region in the input SD-OCT volume by checking the ILM layer segmentation results, which are obtained from Section 4.3.

2. Select the contour voxels of the cut-off region as important landmarks, and then randomly sample the other landmarks from the segmented ILM surface.

3. Perform the TPS interpolation based on the landmarks we obtained from the previous step, and the missing ILM can be regenerated.

4.4.2 Experimental Methods and Results

Eleven complete 3D SD-OCT ONH-centered papilledema scans (including right and/or left eyes from The University of Iowa) were used as inputs. The data selection criterion here was that each of these 11 SD-OCT scans was swollen enough so that the artificial truncation from the top of the swollen disc would not reach out the non-swollen region. The selected 11 SD-OCT images with severe optic disc edema were first segmented using the 3D graph-search algorithm. Then, based on the segmentation results, the ILM tip of each input SD-OCT scan can be detected. To compare the recovered ILM with the original ILM for each input SD-OCT volume, 50, 100, 150 voxels were artificially cut off from the ILM tip of each scan. Therefore, 44 SD-OCT volumes from 11 papilledema subjects (which include the input 11 complete papilledema SD-OCT volumes and the 50, 100, 150 pixels artificially cut-off versions) were used in this experiment. The flow chart is shown in Fig. 4.4.

For these 11 input complete SD-OCT volumes with papilledema, the mean absolute errors of the artificially truncated volume by 50, 100, 150 voxels were 0.045, 0.236, and 0.565 mm^3. After recovering the missing ILM, the mean absolute errors of the corrected volumes were 0.044, 0.035 (significantly decreased), and 0.120 (significantly decreased) mm^3, where $p < 0.01$ (Fig. 4.5). Fig. 4.6 is an example of how the ILM undergoes the transition from the original segmentation, the 150 voxel artificial truncation, and after the TPS correction. In this particular example, 3.29% of the volume is lost after the truncation and 99.79% of the volume is recovered after TPS interpolation.

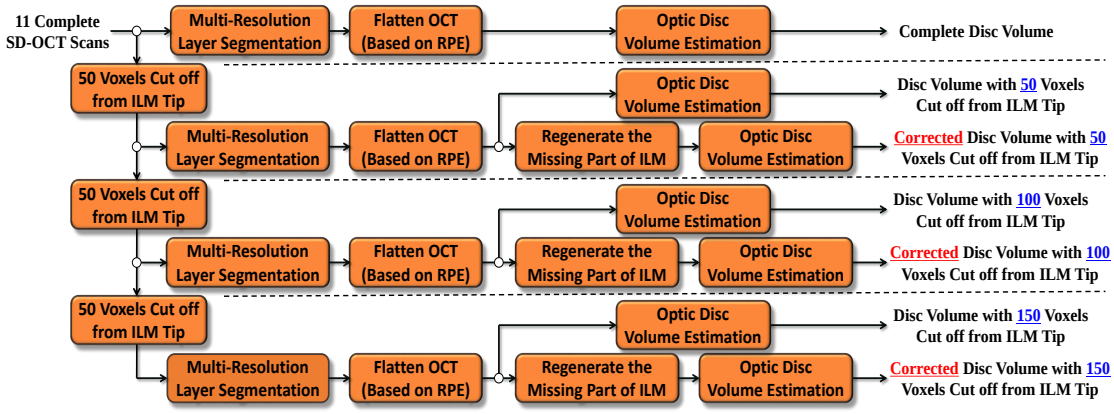

Figure 4.4: A flow chart of the automated approach of repairing the truncated inner retina, where the regeneration of the missing part of the ILM was implemented by using the TPS interpolation, and the optic disc volume was defined between the ILM and the bottom surface of the RPE complex (i.e., botRPE).

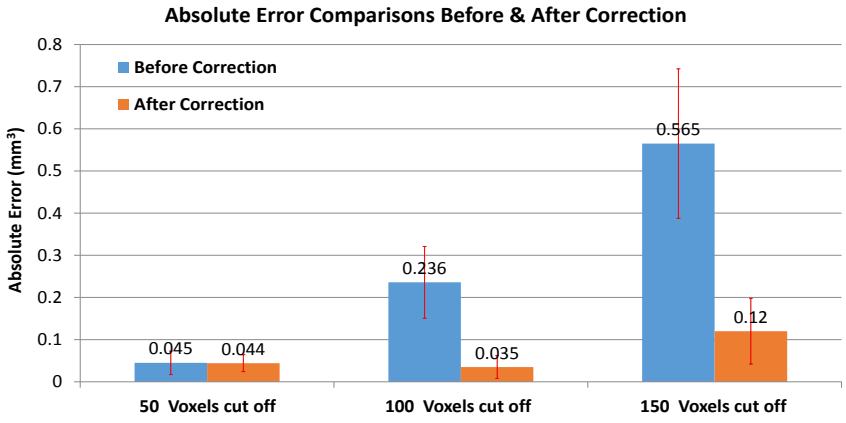

Figure 4.5: Absolute differences of comparing 11 complete SD-OCT volumes and 50, 100, and 150 voxels cut-off from the top tip of the ILM.

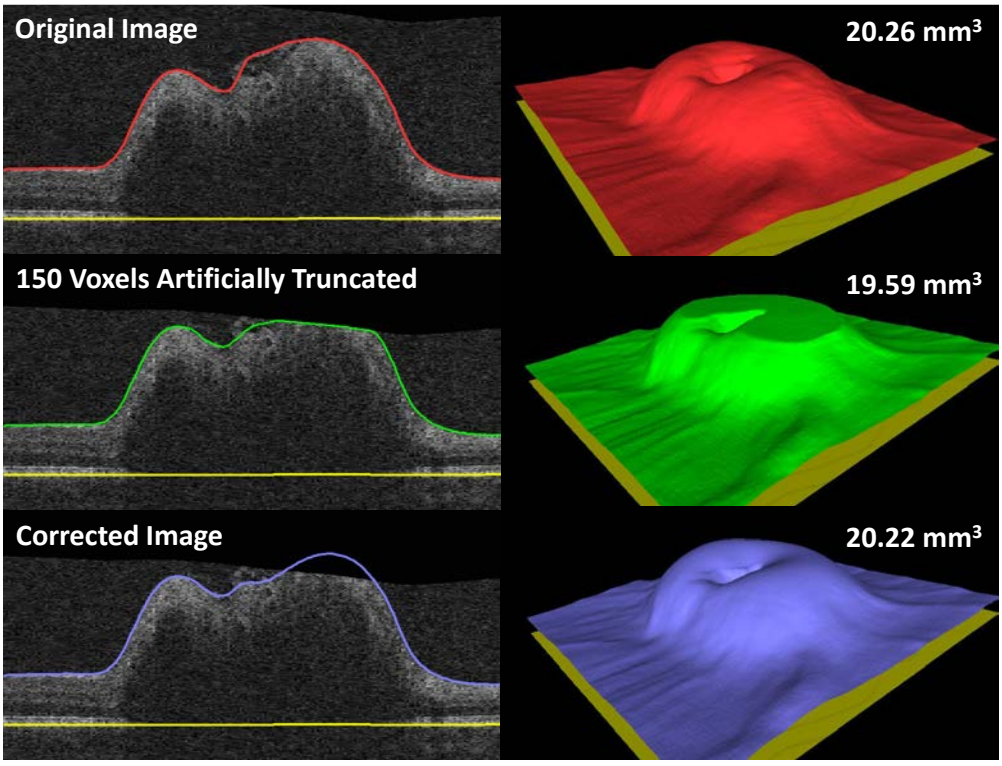

Figure 4.6: A central B-scan with 3D layer segmentation results and its missing ILM correction.

4.4.3 Conclusions

The unadjusted volumetric quantification can be underestimated when the swollen optic disc does not completely conform to the dimensions of the OCT imaging window, causing them to be truncated. By reconstructing the missing inner retina using TPS interpolation and then re-computing the corrected disc volume, the volumetric measurement for papilledema becomes more reliable.

CHAPTER 5
BRUCH'S MEMBRANE OPENING SEGMENTATION IN SWOLLEN OPTIC DISCS USING COMBINED INFORMATION FROM SD-OCT HD-5LR RASTER SCANS AND VOLUMETRIC IMAGES (AIM 2)

5.1 Introduction

In cases of optic disc swelling, directly locating the true Bruch's membrane opening (BMO) points in a regular SD-OCT optic-disc-nerve (ONH) volume (for example, Carl Zeiss, ONH protocol with $200 \times 200 \times 1024$ voxels) is a very challenging topic, because the area around BMO is often shadowed by the swollen and deformed inner retina. Also, when the blood vessels pass through the swollen ONH region, they often cause vertical stripe-shape shadows to deteriorate the image quality around the true BMO area. Fig. 5.1 is an example showing how the BMO points look different in a normal eye compared to a papilledema eye.

Compared to the regular ONH SD-OCT images, high-definition 5-line raster scans (HD-5LR, Carl Zeiss, $1024 \times 5 \times 1024$ voxels) are created from another protocol where better image quality is obtained by repeatedly scanning five parallel linear regions and averaging these repeated scans to construct five individual HD B-scans. Due to the HD B-scans having better image quality, the true BMO can potentially be observed in the obscured region under the swollen inner retina if any of these HD B-scan passes

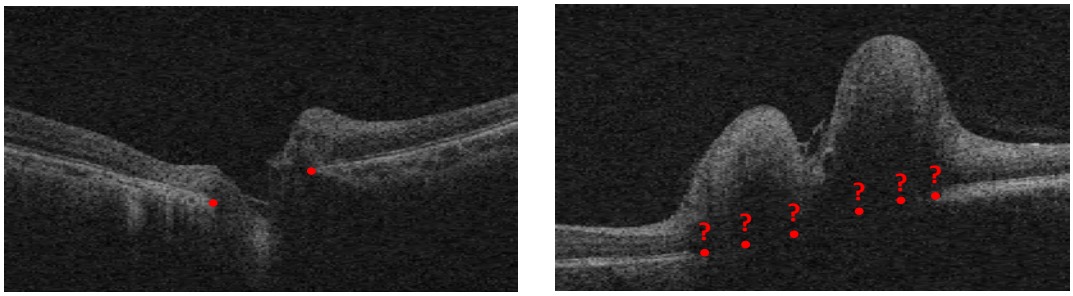

(a) (b)

Figure 5.1: BMO candidate points (the red dots) in the central B-scan of a SD-OCT volume from (a) a normal eye and (b) a papilledema eye.

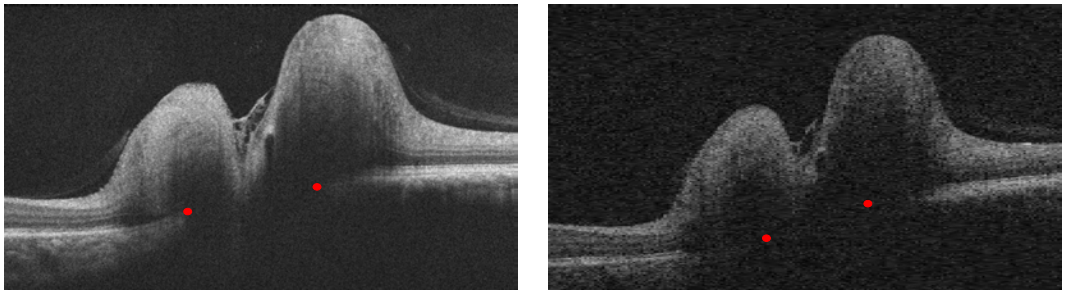

(a) (b)

Figure 5.2: BMO points (the red dots) in a central B-scan of the (a) HD-5LR scan and (b) regular SD-OCT volume.

through the optic disc center. Fig. 5.2 shows the image quality difference between the central B-scans from an HD-5LR and regular volumetric SD-OCT image. One might notice that the BMO points are easier to determine in the HD-5LR central B-scan.

Although the true BMO points are potentially observable in the HD-5LR scans, the information from five HD B-scans is not enough to construct a complete true BMO contour. To identify this contour, a possible approach is to use the BMO information from the HD-5LR scans to place landmarks and then to transfer these landmarks into the corresponding regular SD-OCT volume. Next, a BMO segmentation approach in the regular SD-OCT can be performed to segment the complete BMO contour. In other words, this approach is to combine the SD-OCT volume (3D but lower-resolution) with the HD-5LR scans (higher-resolution but 2D) to help solve the BMO segmentation problem in both the SD-OCT protocols. In practice, directly placing the BMO landmarks in HD-5LR scans using a fully automated method is still not straightforward. Even though the image resolution of each HD B-scan is better than the resolution of the regular SD-OCT volume, the shadow from the inner retina is still unavoidable in cases of severely swollen optic discs. In addition, the border tissue of the RPE complex may also complicate the criteria of deciding the true BMO points.

Therefore, this chapter can be divided into two sections. In Section 5.2, a semi-

automated method is developed to transfer the manually decided BMO points from an HD-5LR scan into the corresponding regular SD-OCT volume to help segment the complete BMO profile. The results from this section give us a positive answer to the question "If we have prior knowledge of the true BMO positions in an HD-5LR scan, is it helpful to use it for segmenting the BMO in the corresponding SD-OCT volume?" Next, Section 5.3 is a straightforward extension of this semi-automated method into a fully automated one.

The **objective** of this chapter (Aim 2) is to develop framework for combining an SD-OCT image volume and the corresponding HD-5LR scan to segment the true BMO under the shadow of the swollen inner retinal tissue. To **achieve** this goal: First, the ILM and RPE complex layers are separately segmented in both SD-OCT and HD-5LR images using the methods from Chapter 4. Second, the HD-5LR scan is registered to the corresponding SD-OCT volume. Third, a 2D-version of the graph-search algorithm [16, 66] is applied to segment the true BMO contour in the RPE *en-face* image domain using the combined information from both the SD-OCT and HD-5LR images. This novel idea is meaningful because this is the first study about using an automated approach to find the true BMO contour for papilledema eyes by combining the information from two types of SD-OCT images with different dimensions as well as resolutions. For the **publication of Aim 2**, the semi-automated method of segmenting the BMO contour in the SD-OCT RPE *en-face* image domain utilizing prior-information from HD-5LR scans was published in [34]. Then, a fully automated version was completed in [71].

5.2 Combined Use of High-Definition and Volumetric Optical Coherence Tomography for the Segmentation of Bruch's Membrane Opening in Cases of Optic Disc Swelling

SD-OCT is a relatively new imaging technique to enable cross-sectional images of the retina and optic nerve head to be acquired. In cases of optic disc swelling, quanti-

tative measurements based on the retinal layer segmentation (such as the thicknesses of the retinal nerve fiber layer and total retina [4], and global/regional volumetric estimations of the optic disc [7, 72]) have been developed to quantify disc edema using volumetric OCT images alone. Recently, studies observing the shape of the peripapillary retinal pigment epithelium and/or Bruch's membrane (pRPE/BM) changes due to elevated intracranial pressure [14, 15] give strong motivation for developing automated methodologies to identify the true Bruch's membrane opening (BMO) for the preparation of generating pRPE/BM shape models.

Although the volumetric OCT has the ability to provide 3D contextual information, the true BMO points are often invisible under the shadows from the swollen retinal tissue. Consequently, a common graph-based BMO segmentation approach [66], which was originally designed for glaucoma eyes, often overestimates the true BMO contour in cases of optic disc swelling. The goal of this task is to develop an approach to segment the true BMO by utilizing information from both SD-OCT scans (providing 3D context) and the HD-5LR scans (providing better local visibility of the BMO). In particular, for each SD-OCT volume and the HD-5LR scan pair, the proposed approach first automatically registers these HD B-scans into the SD-OCT image. Next, six manually placed BMO points (two points from each of the three central HD B-scans) are transferred into the SD-OCT RPE *en-face* image. Next, the input cost image of the unwrapped RPE *en-face* image is updated by dramatically suppressing the cost values around the converted landmarks. Finally, the graph-based approach with shape priors [64] is applied to identify the true BMO contour. In this task, using the OCT image pairs from 25 patients with optic disc swelling, the computed BMO points from the proposed method are compared to the traditional method [66] (which uses the volumetric OCT scans alone) and to two sets of manually marked BMO points from an independent observer. This method has been published [34].

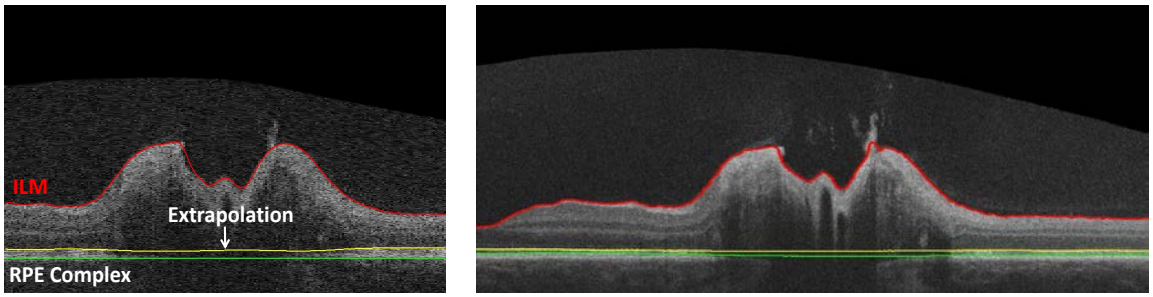

(a) (b)

Figure 5.3: Examples of the flattened retina in the central B-scan. (a) Regular volumetric scan. (b) HD-5LR scan.

5.2.1 Retinal Layer Segmentation

The input ONH OCT volumes (image dimensions of $200 \times 200 \times 1024$ voxels covering $6 \times 6 \times 2$ mm^3, Carl Zeiss Meditec, Dublin, CA) and the corresponding HD-5LR scan (contains five non-successive HD B-scans; each HD B-scan has image dimensions of 1024×1024 pixels covering 9×2 mm^2, Carl Zeiss) are automatically segmented, using graph-theoretical algorithms in 3D and 2D, respectively (Chapter 4). Here, the internal limiting membrane (ILM) and the upper and lower bounding surfaces of the retinal pigment epithelium (RPE) complex are the target surfaces. To reduce the effect of motion artifacts within the SD-OCT images, both the 2D HD B-scans and 3D volumetric images are flattened using the lower bounding surface of the RPE as the reference plane. Fig. 5.3 (a) and 5.3 (b) are examples of a flattened retina with layer segmentations in the central B-scan from a SD-OCT volume and the corresponding HD-5LR scan, respectively. During flattening, as the RPE surfaces (i.e., the yellow and green lines) are not defined inside the BMO region, a thin-plate-spline method [70] is used to extrapolate the segmented surfaces inside a central cylindrical region (of constant size) defined to be larger than the expected size of the BMO.

5.2.2 Image Registration Between SD-OCT HD-5LR and Volumetric Scans

To use the combined information from each SD-OCT HD-5LR scan and the corresponding volumetric scan, image registration is performed in an automated fashion in the flattened OCT image domain to register the five HD B-scans to the corresponding B-scans within the volumetric scan. First, independent 2D-to-2D registrations for each HD B-scan in a particular location range within the SD-OCT volume are pre-computed. Here, the image registration is done by using rigid transformations and the sum-of-the-squared-differences registration metric as implemented in the Insight Segmentation and Registration Toolkit (ITK). Specifically, with our assumption that the HD-5LR scans and the volumetric scan are both reasonably centered on the optic nerve head, the central (i.e., the third) HD B-scan is registered to each of the volumetric B-scans between 80 and 120 (out of the 200 B-scans in the entire volume) and the pairwise registration metric values and registration parameters saved. Similarly, based on the default distance of 0.5 mm (around 17 B-scans in the SD-OCT volume) between two neighboring HD-5LR B-scans (and allowing for a $\pm$ 0.06 mm deviation = $\pm$ 2 B-scans in the SD-OCT volume), the volumetric B-scan location range for pre-computing the registration metric values and registration parameters corresponding to the first, second, fourth, and fifth high-definition raster scans were 44–88, 61–105, 95–139, and 112–156, respectively.

Next, based on these pre-computed independent 2D-to-2D registration metric values, for each candidate registered volumetric B-scan location corresponding to the central HD B-scan (i.e., volumetric B-scan locations 80–120), a "grouped" registration is obtained by finding the best matching volumetric B-scan (i.e., B-scan with smallest pre-computed registration metric) for each of the remaining four HD raster B-scans such that each chosen volumetric B-scan satisfies the expected physical distance constraints. In particular, we require that the other chosen B-scan locations

be within 0.06 mm (= 2 B-scans) of the expected physical distance. For example, to determine the grouped registration corresponding to the central HD B-scan registered to volumetric B-scan 80, for the first HD B-scan the B-scan with the smallest pre-computed registration metric from 2D-to-2D registrations with volumetric B-scans 44–48 would be chosen; for the second HD B-scan, the constrained range would be B-scans 61–65; for the fourth HD B-scan, the constrained range would be B-scans 95–99, and for the fifth HD B-scan, the constrained range would be 112–116. In general, for the central HD B-scan at physical location x, the optimal volumetric B-scans corresponding to the first, second, fourth, and fifth high-definition B-scan are constrained to be at location $x - 1.0$ mm $\pm$ 0.06 mm, $x - 0.5$ mm $\pm$ 0.06 mm, $x + 0.5$ mm $\pm$ 0.06 mm, and $x + 1.0$ mm $\pm$ 0.06 mm, respectively. The grouped registration metric is computed by summing all of the individual B-scan registration metric values.

After computing the grouped registration metric values for each set of specified possible physically constrained B-scan registration locations, the set with the overall lowest grouped registration metric becomes the final registration. Fig. 5.4 (a) provides an example *en-face* image, which is generated by averaging the voxel intensities in each A-scan in the RPE complex from an SD-OCT volume [between the yellow and green surfaces in Fig. 5.3 (a)]; Fig. 5.4 (b) shows an example of a projective view of the registered HD B-scans on the *en-face* image, for which the yellow and green horizontal lines indicate whether the HD B-scans do or do not pass the BMO region, respectively.

5.2.3 Manual Placement of BMO Points in HD B-Scans

Considering often only three of the five high-definition OCT B-scans pass through the BMO region in the SD-OCT volume [i.e., the yellow lines in Fig. 5.4 (b)], two BMO points in each of the three central HD B-scans are manually placed resulting

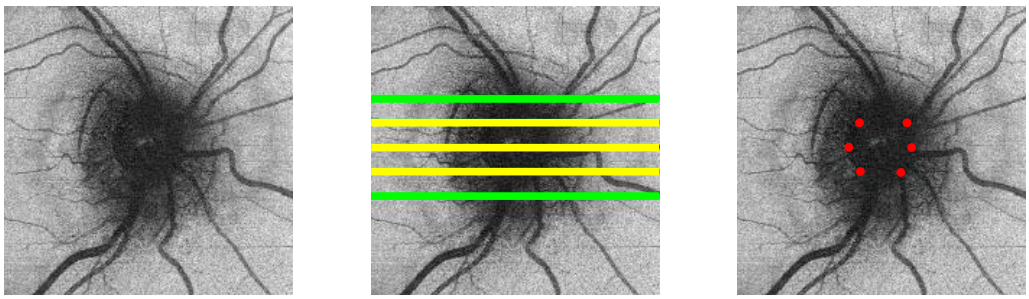

(a) (b) (c)

Figure 5.4: Registration of the HD B-scans and manual BMO landmarks into the corresponding SD-OCT volume. (a) The SD-OCT RPE *en-face* image. (b) The projective view of the registered HD B-scans [note: the green and yellow lines represent the B-scans that do not pass and pass the BMO region, respectively] in the RPE *en-face* image. (c) The projected view of the mapped manual BMO points from the three central HD B-scans.

in the total of six manual points. In particular, each of the three central input HD B-scans is first resized from 1024×1024 pixels to 4608×1024 pixels to reflect the true 9:2 width-to-height ratio in the physical domain. Then, two BMO landmarks are manually placed in each input HD B-scan using GNU Image Manipulation Program (GIMP, version 2.8.10). Next, these six manually placed landmarks are automatically mapped into the SD-OCT image domain using the registration information computed as described in Section 5.2.2. Fig. 5.4 (c) shows the projective view of the mapped BMO landmarks in the SD-OCT RPE *en-face* image. It is worthwhile to note that the BMO point placement in the central three HD B-scans is the only manual step in the proposed method.

5.2.4 BMO Contour Segmentation in SD-OCT RPE *En-Face* Images

Transferring a 2D circular object segmentation problem into a 2D horizontal direction boundary segmentation problem is a typical step in finding the BMO contour using a graph-search algorithm in the SD-OCT *en-face* image domain [66]. To make this idea work, the SD-OCT RPE *en-face* image is first unwrapped based on the

approximate BMO center (defined as the halfway point between the two BMO landmarks from the registered central HD B-scan). In the unwrapped polar-coordinate domain, the BMO boundary can be considered a function of θ, mapping θ values to radial values. Taking advantage of the fact that the BMO is generally oval-like in the RPE *en-face* image (which means the BMO shape prior prefers neighboring changes of the BMO boundary, $f(\theta)$, to remain small in the unwrapped image domain), the graph-based algorithm to include shape-prior constraints [64] is next performed. In particular, the cost image, $C(r, \theta)$, is generated by computing the gradient in the radial direction in the *en-face* image and then locally modifying it by dramatically decreasing the costs around the manual BMO points. The graph-based approach finds the projected BMO boundary $f(\theta)$ with the minimal total cost:

$$C_{Total} = \sum_{\theta=0}^{359} C(f(\theta), \theta) + \lambda \sum_{\theta=0}^{358} [f(\theta+1) - f(\theta)]^2 + \lambda [f(0) - f(359)]^2 \qquad (5.1)$$

where the first term reflects the contribution of the boundary cost from the image-based cost term and the other terms represent the shape cost with the consideration of the circularly constraint. Note that there are two differences between the traditional [66] and proposed method: (1) the use of soft-smoothness constraints [64] (as reflected in the shape-prior terms in C_{Total}) rather than only hard smoothness constraints, and (2) the added incorporation of image information from the HD B-scans in the cost function $C(r, \theta)$.

5.2.5 Manual Tracing for Evaluation

Because of the difficulty of directly visualizing the BMO in volumetric OCT scans, an independent observer manually traced the BMO points in the radially transformed SD-OCT volumes twice (with the mean of the two tracings being used as the reference), where 12 equiangular points are placed covering the entire 360 degrees (in other words, placing one manual BMO point for every 30 degrees). As an example, Fig. 5.5

(a) shows the locations of the 12 radial scans, which are highlighted in purple. For each radial scan, the observer places a landmark to indicate the BMO point. In the first (second) session, these landmarks are colored in yellow (cyan). Fig. 5.5 (b, c) are the examples of the first and second session traces in the radial scan at 0°. Fig. 5.5 (d, e) show all the manual landmarks in the projective view on the RPE *en-face* image domain from Fig. 5.5 (b, c), respectively. Finally, Fig. 5.5 (f) shows the mean landmark locations between both manual tracing sessions (green dots).

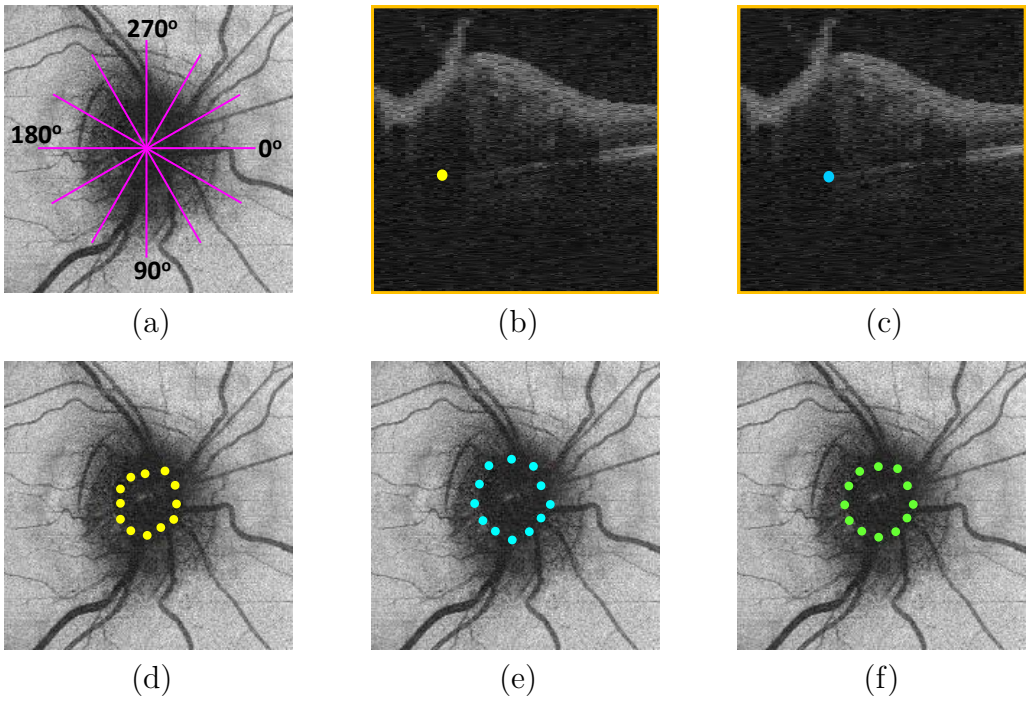

Figure 5.5: Manually marking BMO points in the radial SD-OCT domain. (a) Locations of 12 radial scans in the SD-OCT RPE *en-face* image. (b, c) Expert's first and second tracing sessions in the 2D radial scan at 0°. (d, e) Projective views of expert's first and second tracing sessions with 12 landmarks on the SD-OCT RPE *en-face* images. (f) The mean locations of 12 landmarks between (d) and (e).

5.2.6 Experimental Methods and Results

Twenty-five SD-OCT volumes and the corresponding HD-5LR scans from 25 different subjects with optic disc edema from the University of Iowa were used, where the ONH volume of each input SD-OCT image was larger than 14.42 mm^3 (equivalent to Frisén scale grade 2 in our previous work [7]). For comparison purposes, the traditional graph-search method was implemented [66]. To achieve that, the SD-OCT RPE *en-face* image was unwrapped [Fig. 5.6 (a)]. Then, the BMO boundary was segmented using the traditional 2D graph-search method without applying shape-prior information in the unwrapped cost image [Fig. 5.6 (b)] and then was transferred back to the original *en-face* image. Here, the traditional method was often affected by the shadow from the swollen optic disc and overestimated the size of the true BMO [Fig. 5.6 (c)].

Next, the proposed method was also applied to the unwrapped *en-face* image. Fig. 5.6 (d) illustrates the new version of the cost image by dramatically decreasing the local cost near the locations of the converted BMO landmarks (i.e., the dark butterfly patterns). Fig. 5.6 (e) demonstrates the segmented BMO boundary. Next, the BMO was transferred back to the original *en-face* image, and Fig. 5.6 (f) shows the final BMO segmentation. Note that the segmented contour is correctly located on the boundary of the true BMO instead of the shadow region.

Fig. 5.7 shows examples from four different subjects (where the total retinal volumes from the left to right column were 14.53, 17.13, 20.53 and 25.37 mm^3, respectively); in the first row are the RPE *en-face* images, in the second row are the BMO segmentation results using the traditional graph-search method [66], in the third row are the results using the proposed method, in the fourth, fifth and sixth rows are manual tracing 1 (yellow dots), manual tracing 2 (cyan dots) and the mean manual tracing (green dots), respectively.

Signed and root mean square (RMS) differences (mean ± standard deviation)

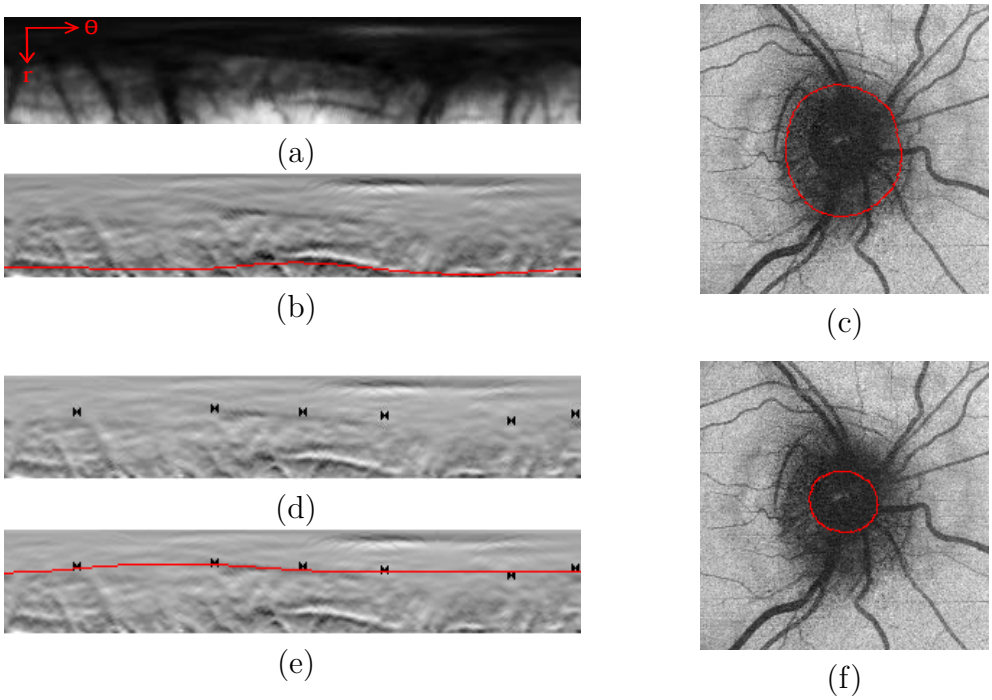

Figure 5.6: Comparison examples of BMO segmentations in the SD-OCT RPE *en-face* images using the traditional and proposed semi-automated methods. (a) Unwrapped RPE *en-face* image. (b) Segmented BMO boundary in the unwrapped cost image using the traditional method. (c) Segmented BMO in the *en-face* image using the traditional method. (d) Locally modified cost image (i.e., the dark butterfly patterns) using the combined information from both SD-OCT and HD-5LR B-scans in the unwrapped en-face image domain. (e) Segmented BMO boundary in the unwrapped *en-face* image using the proposed method. (f) Segmented BMO result in the *en-face* image using the proposed method.

between (1) the traditional graph-based method and mean manual tracing, (2) the proposed approach and mean manual tracing, and (3) manual tracings 1 and 2 were computed in the unwrapped *en-face* image domain, and the results are shown in Table 5.1. The proposed approach had significantly smaller ($p < 0.001$) RMS differences with the mean manual tracing (5.34 ± 3.34 pixels) than the traditional approach (21.71 ± 3.87 pixels). The proposed approach also had slightly larger RMS differences with the mean manual tracing than that computed from the repeat tracings of a single observer (4.22 ± 1.97 pixels); however, the differences were not significant

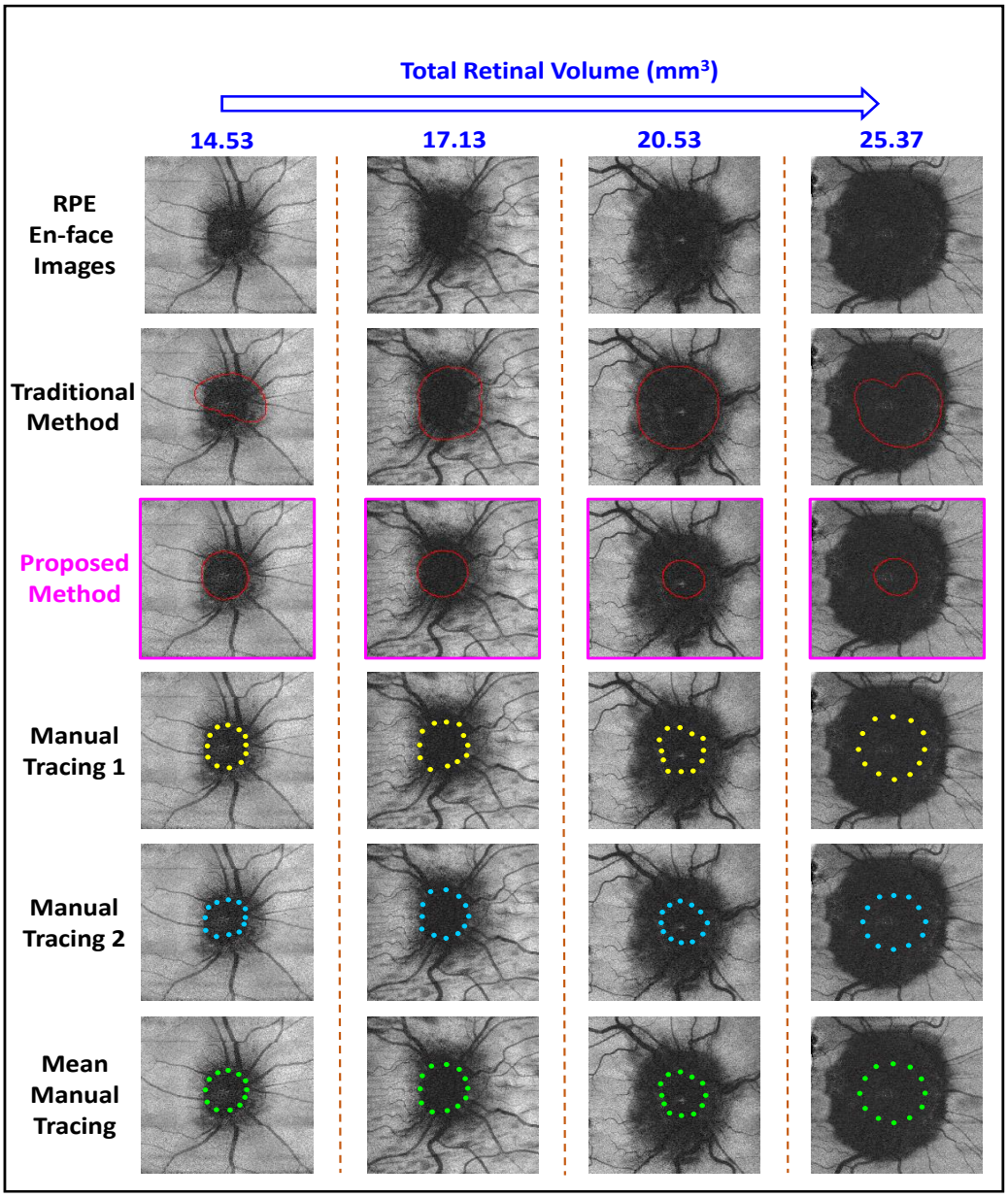

Figure 5.7: BMO segmentations in cases (columns) with different degrees of optic disc swelling from mild to severe (from 14.53 to 25.37 mm^3).

Table 5.1: Summary of signed/unsigned BMO positioning differences in pixels[†].

	Traditional Approach vs. Mean Manual Tracing	Proposed Approach vs. Mean Manual Tracing	Manual Tracing 1 vs. Manual Tracing 2
Signed Difference	18.42 ± 8.44	-2.94 ± 4.62	-0.83 ± 2.55
RMS Difference	21.71 ± 3.87	5.34 ± 3.34	4.22 ± 1.97

[†] Mean ± SD in pixels for 25 subjects with optic disc edema, where the pixel size is 30×30 μm.

(p-value = 0.16).

5.2.7 Conclusions

As was illustrated in Fig. 5.1, detecting the BMO in cases of optic disc edema using SD-OCT volumes alone is very challenging. Using the non-modified graph-search method often outputs an overestimated result due to the shadow from the swollen retinal tissue. The proposed semi-automated approach, combining the extra information from the HD-5LR and volumetric scans, is capable of segmenting the true BMO in a swollen optic disc. The outputs of the proposed method are not significantly different to the expert's manual tracing. Although the proposed method is not fully automated, the processing time of placing six manual landmarks in the central three B-scans from the input HD-5LR scan is practically acceptable (around one to two minutes per HD-5LR scan). However, one limitation is that the BMO points can sometimes still be totally obscured under extremely swollen optic discs in HD-5LR scans. Under this circumstance, the accuracy of the proposed method might be affected by the incorrect BMO manual placement. In addition, the limited visibility of the BMO can also affect the reference standard (e.g., the larger area of the BMO in the most severe case of swelling in Fig. 5.7 may be due to the limited visibility of the BMO). In such situations, comparing the resulting BMO areas at the time of

swelling to that from a later time in which the swelling has decreased is expected to be useful. Finally, future work will focus on completely automating this semi-automated approach (i.e. the next task in Section 5.3) and using the detected BMO points to build 3D shape models (which will be introduced in Section 6.3). Combining the use of low- and high-definition images may be beneficial in other application areas as well.

5.3 Fully Automated Bruch's Membrane Segmentation Using Combined 2D and 3D SD-OCT with Shape-Prior, Multiple Texture Information and *En-Face* Image in Severely Swollen Optic Discs

Since the results from Section 5.2 give a positive answer to the original question "If we have prior knowledge of the true BMO position in an HD-5LR scan, is it helpful to use it for segmenting the BMO in the corresponding SD-OCT volume?," the goal in this section is to improve the semi-automated approach (requiring six manually placed landmarks from the input HD-5LR scan) to a fully automated version. To achieve this goal: First, the topographic shape of the internal limiting membrane (ILM) and the textural information near BM are utilized to roughly estimate five candidate BMO sets, from five individual approaches, in the central three HD-5LR scans. For each HD B-scan, the mean of three closest BMO candidates is considered the final BMO estimation in the HD-5LR image domain. After transferring the final BMO estimation from the HD-5LR image domain into the volumetric SD-OCT RPE *en-face* image domain, a graph-search algorithm with constraints on the BMO size [73] and shape prior [64] is further applied to segment the complete 2D BMO contour. Finally, comparing the three segmented BMO contours from the second, third and fourth HD B-scans, the algorithm automatically decides which HD B-scan is the best central B-scan (i.e., the one passing through the optic disc), and its corresponding BMO contour is considered as the final BMO segmentation results. A preliminary outcome of this fully automated method was published in [71].

5.3.1 Layer Segmentation and Registration in SD-OCT Images

The input SD-OCT image pairs (i.e., the HD-5LR and volumetric scans), first, need to be segmented and registered together. This step is exactly same as what was discussed in Section 5.2.1 and 5.2.2.

5.3.2 BMO Estimations in Central HD-5LR B-scan

To fully automate the semi-automated approach from Section 5.2, the key step is to automate the only manual process of placing the BMO landmarks. However, as we discussed before, due to the poor visibility around the BMO, directly segmenting BMO in SD-OCT images with severely swollen optic discs is very challenging. Therefore, a compromised idea is to first roughly estimate the BMO in the HD central B-scans using multiple methods and then merge these individual weaker results into a better estimation. Here, five separate methods are proposed to automatically estimate the BMO in the central HD-5LR B-scan, where Approach 1 uses the topographic shape of the ILM and the other four approaches uses textural information along the BM surface. Next, the determined BMO points at the nasal and temporal sides are separately calculated by averaging the closest three candidates at each side and are used to generate a cost image as the input of the graph-search algorithm.

5.3.2.1 Approach 1

By observing SD-OCT images in more than 100 papilledema subjects in the dataset of Idiopathic Intracranial Hypertension Treatment Trail (IIHTT) OCT substudy [11,12,68], it is noticeable that the BMO points in the central HD-5LR B-scan are often approximately found under two ILM peaks [Fig. 5.8 (a)]. Compared to the other retinal layers, the ILM is relatively clear, and the ILM segmentation is robust from the perspective of automated algorithms. Therefore, the original problem of directly finding two BMO points can be recast as a problem of finding the locations

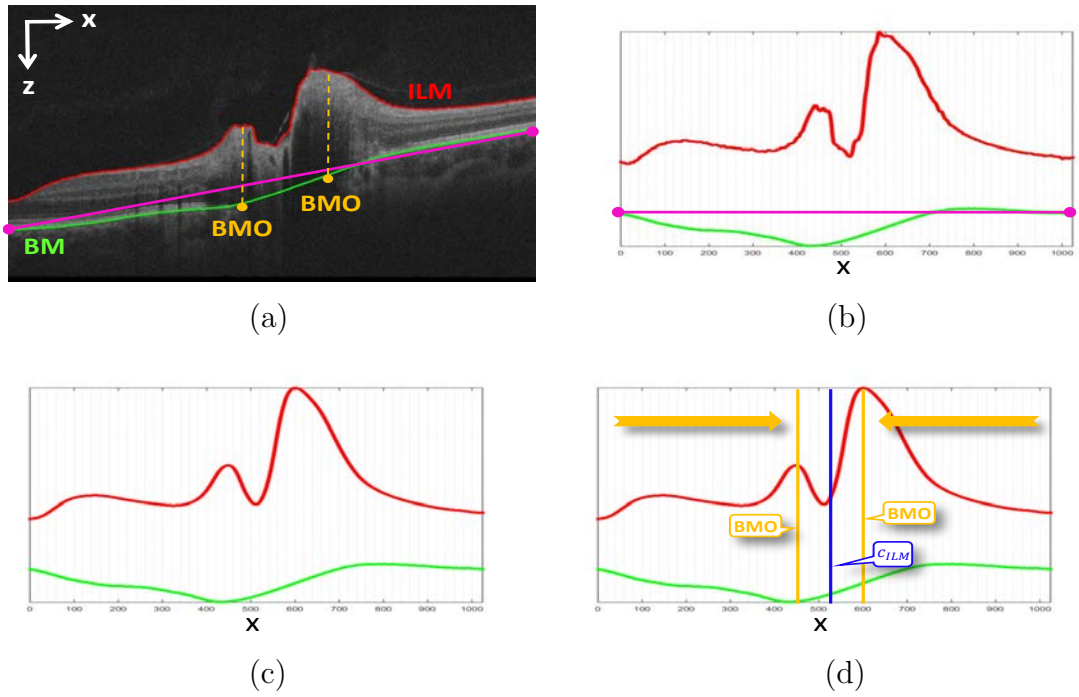

Figure 5.8: Three steps in Approach 1 of estimating BMO points. (a) The original central HD-5LR B-scan with segmentation, where the purple line was just a straight line connecting the two ending points of the BM surface. (b) Flattened segmentation results. (c) Smooth surfaces using thin-plate-spline interpolation. (d) BMO estimation from the two significant local peaks.

of the two local extreme ILM peaks. Approach 1 has three steps. First, flatten the retina using a reference line that connects the two ending points of the BM surface in the input HD B-scan [Fig. 5.8 (a, b)] to prevent the tilted retina from affecting the detection of the local ILM peaks. Second, use the thin-plate-spline (TPS) [70] interpolation to smooth the segmented ILM surface [Fig. 5.8 (c)]. Third, detect the locations of the two ILM peaks with the minimum local values [Fig. 5.8 (d)]. Also, a roughly estimated BMO center in the **x** direction, c_{ILM}, is decided by computing the middle point of the two ILM peaks.

However, this approach does not apply to cases with extremely severe optic disc swelling. The reason is that the inner retina usually appears as a stretched "M" shape in mild to severe cases of optic disc swelling. In addition, when the swelling is

extremely severe, the inner retina may deform as the shape of an iceberg, which has just one peak. So, if the algorithm only detects a single ILM peak, no BMO candidates are generated. Also, the center of the BMO points (c_{ILM}) would be assigned to the scan center.

5.3.2.2 Approach 2

A 1D projected array (named RPE-line) is computed by averaging A-scan intensities between the RPE complex in the input HD-5LR B-scan as shown in Fig. 5.9 (a). The RPE-line reflects a stronger response on the true retinal tissue between the RPE complex and a weaker response in the space between the desired two BMO points. Then, the RPE-line ($f[x]$) is smoothened using TPS interpolation [Fig. 5.9 (b)]. Next, the differenced smooth RPE-line ($d[x] = f[x] - f[x-1]$) is computed [Fig. 5.9 (c)]. Next, the intensity-difference RPE-line, which is denoted as $d_f[x]$, is computed in Algorithm 1. Finally, searching the $d_f[x]$ from the left to the right [Fig. 5.9 (d)], the left BMO point is estimated by detecting the x with the minimum value of $d_f[x]$ before the pre-estimated BMO center, c_{ILM}, obtained from Approach 1. Next, the right BMO point is estimated using the same steps, but everything starts from the right-hand side to the left-hand side in the x-axis. Thus, the second candidate set of the BMO points is then obtained.

5.3.2.3 Approach 3

A thresholding method is used in Approach 3 to enhance the RPE-line intensity contrast between the retinal tissue and image background. The threshold value (μ_{bg}) is estimated by computing the mean image background intensity in two small squares at both sides of the top corners in the input HD-5LR B-scan. Then, the pixels with intensity lower than $c \cdot \mu_{bg}$ ($c = 1.55$ in this work) are re-assigned so that their intensity is zero; the remaining pixels are rescaled to grey-levels from 0 to 255. After that, a 5×3 mean-image filter is applied to reduce the noise. Fig. 5.10 (a) and (b) show the

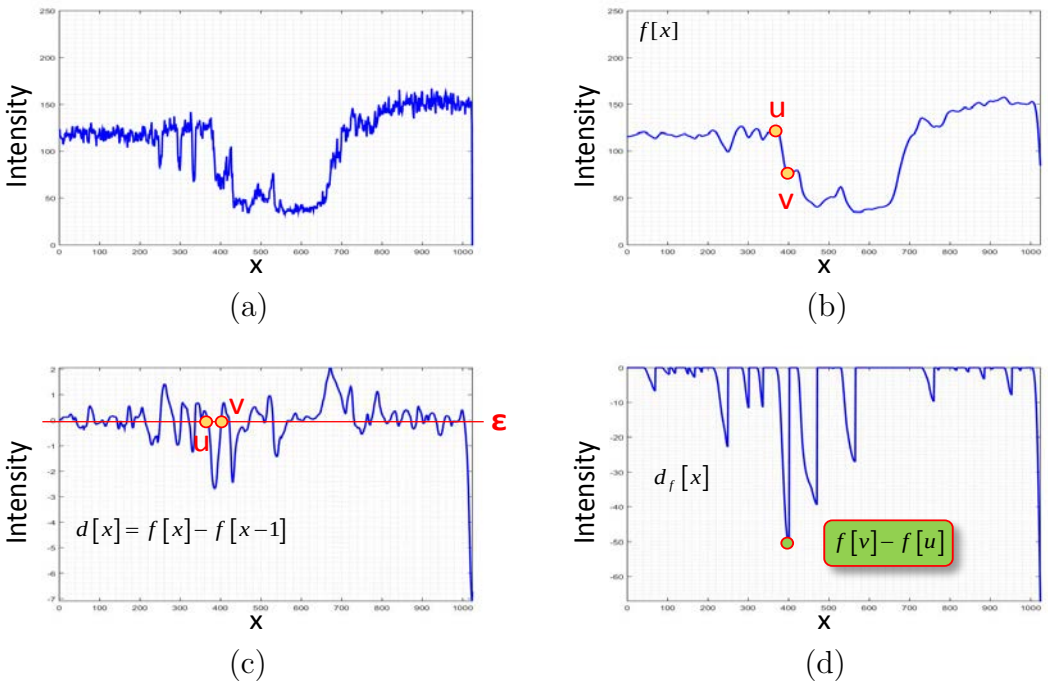

Figure 5.9: Steps of finding the first dropping point on the RPE-line. (a) The original intensity response of the RPE-line. (b) Smooth RPE-line using TPS, $f[x]$. (c) Differenced RPE-line, $d[x] = f[x] - f[x-1]$. (d) Intensity-differenced RPE-line, $d_f[x]$ (which is generated using Algorithm 1).

Algorithm 1: Finding the first significant dropping point on RPE-line from the left [for example, point v in Fig. 5.9 (b)], where L is the length of $d[x]$, ϵ is a parameter to control the degree of the algorithm tolerating the ripple on $d[x]$.

Result: The found x is the estimated left BMO point at x-direction
Initiliazations: $a \leftarrow 0$; $b \leftarrow 0$
while $x < L$ **do**
  if $d[x] > \epsilon$ **then**
    $d_f[x] = 0$,
    $x \leftarrow x + 1$.
  else
    while $d[x] \leq \epsilon$ **do**
      if $d[x] = \epsilon$ **then**
        $d_f[x] = 0$,
        $a \leftarrow x$,
        $x \leftarrow x + 1$.
      else
        $b \leftarrow x$,
        $d_f[x] = f[b] - f[a]$,
        $x \leftarrow x + 1$.
      end
    end
  end
end
Find x with minimum $d_f[x]$ **when** $x < c_{ILM}$.

original HD-5LR central B-scan and the thresholded image [$\mathcal{I}_{Thd}(x, y)$], respectively, where the pseudo-color code is applied for the purpose of better visualization of the retinal texture. A different RPE-line is computed by applying Approach 2 to $\mathcal{I}_{Thd}(x, y)$, and the third set of BMO points is obtained.

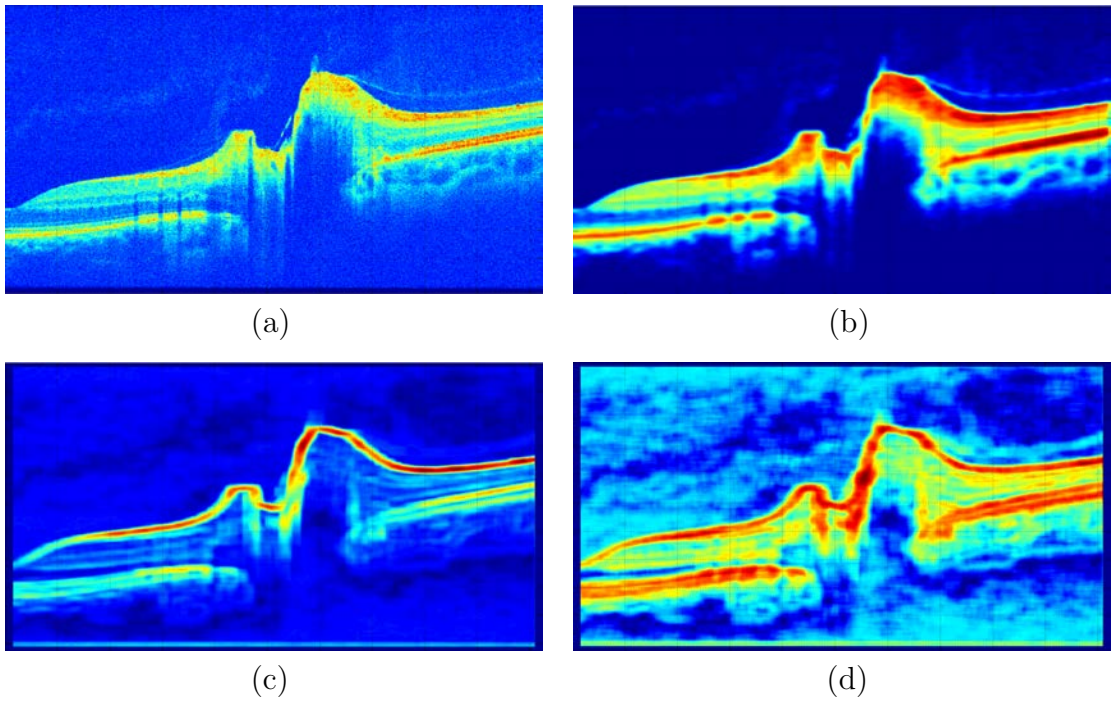

Figure 5.10: HD-5LR central B-scan with different image-enhancement methods. (a) Original image. (b) Thresholding image [$\mathcal{I}_{Thd}(x, y)$]. (c) Variance image [$\mathcal{I}_{Var}(x, y)$]. (d) GLCM entropy image [$\mathcal{I}_{Epy}(x, y)$]. [Note: Pseudo-colors are used for better visualization, where dark blue (or red) represents the gray level intensity of 0 (or 255)].

5.3.2.4 Approach 4

A typical method to extract textural information is to compute the variance of the target image. In this task, a sliding window of dimensions $(2m + 1) \times (2n + 1)$ (here $m = n = 15$) is applied to the entire input image to obtain the textural information.

For each pixel $p(x, y)$ in the sliding window, the mean (μ) can be written as

$$\mu(x, y) = \frac{1}{(2m+1) \times (2n+1)} \sum_{i=-m}^{m} \sum_{j=-n}^{n} p(x+i, y+j). \tag{5.2}$$

Then, the variance image, $\mathcal{I}_{Var}(x, y)$ [Fig. 5.10 (c)], can be generated by

$$\mathcal{I}_{Var}(x, y) = \frac{1}{(2m+1) \times (2n+1)} \cdot \sum_{i=-m}^{m} \sum_{j=-n}^{n} [p(x+i, j+j) - \mu(x, y)]^2. \tag{5.3}$$

By using $\mathcal{I}_{Var}(x, y)$, another RPE-line is computed, and the fourth candidate set of the BMO points is estimated.

5.3.2.5 Approach 5

Approach 5 uses the same sliding window from Approach 4 but computes the gray-level co-occurrence matrices (GLCM) [74, 75] instead of the regional standard deviations. The concept of GLCM is to tabulate the combinations of the intensity for each pixel pair in the sliding window; here, the reference pixel is denoted as $p(m, n)$ and its neighbor pixel as $p(m+dx, n+dy)$ with an offset $d = (dx, dy)$. The input HD-5LR B-scan is first rescaled to 16 gray-levels ($G = 16$), and then GLCMs ($M_{\phi}^{(x,y)}[i, j]$, $\phi = 45°, 90°$ and $135°$) are computed using the sliding window. Next, the GLCM entropy property is adopted to reflect the orderly information of the current location of the sliding window at its center pixel $p(x, y)$. Here, for each $M_{\phi}^{(x,y)}[i, j]$, the GLCM entropy can be described as

$$Entropy_{\phi}(x, y) = \sum_{i,j=0}^{G-1} M_{\phi}^{(x,y)}[i, j] \cdot (\text{-ln } M_{\phi}^{(x,y)}[i, j]). \tag{5.4}$$

To achieve the strongest response, the final GLCM entropy image, $\mathcal{I}_{Epy}(x, y)$

[Fig. 5.10 (d)], is described as

$$\mathcal{I}_{Epy}(x,y) = \max\{Entropy_{\phi}(x,y); \phi = 45^{\circ}, 90^{\circ} \text{ and } 135^{\circ}\}. \quad (5.5)$$

Again, a new RPE-line is computed by applying Approach 2 to $\mathcal{I}_{Epy}(x,y)$, and then the fifth set of the BMO points is obtained.

After obtaining all five sets of the BMO estimations (or four sets if Approach 1 does not output the candidate due to extreme optic disc swelling), the final estimated left and right BMO points are decided by averaging the most clustered three of the five BMO candidates, separately.

5.3.3 BMO Contour Segmentation in SD-OCT RPE *En-Face* Image

In the previous work (Section 5.2 [34]), six landmarks from the central three HD-5LR B-scans are manually placed and automatically mapped into the unwrapped RPE *en-face* cost image to provide anchors with very low costs for the 2D graph-based algorithm with the shape-prior constraint to segment the BMO. In this task, Approaches 1 to 5 are applied to the input HD-5LR second, third and fourth B-scans [i.e., yellow lines in Fig. 5.4 (b)], so three individually estimated BMO sets are computed. For each input HD B-scan, the estimated BMO points are converted into the RPE *en-face* image, and then the unwrapped center is computed. Next, the RPE *en-face* image is unwrapped, and the cost image is computed using the gradient information. Then, applying the mean and standard deviation of the mean normal BMO size as constraints [73], the unwrapped cost image is modified by assigning extremely high costs in regions at least three standard deviations away from the unwrapped mean BMO contour. Using this modified unwrapped cost image, the graph-search algorithm with shape priors is used to segment the BMO contour, and then the results are converted back to the SD-OCT RPE *en-face* image. Therefore,

three individual BMO contours are obtained from the HD-5LR second, third and fourth B-scans, respectively.

In this setting, even when the HD-5LR scan is slightly off from the optic disc center (i.e. the third B-scan is not centered at the optic disc), the second or fourth B-scan may still have the chance to pass through the disc center. (Examples are shown in Sec. 5.3.4). Next, for each set of HD-5LR central three B-scans, the standard deviation (σ) of the pixel intensity in an annulus-like region from the segmented BMO to one-third the radial distance away toward the BMO center was computed. Because the incorrectly segmented BMO contours pass through the optic disc and the image background at the same time, this scheme outputs a smaller σ value from the correctly estimated BMO region than the other two incorrect BMO regions. Finally, $s + \sigma_2$, σ_3 and $s + \sigma_4$ as derived from the second, third and fourth HD-5LR B-scans, were computed around the BMO contour with the lowest value was the final result. (Note: Based on the image protocol, the third HD-5LR B-scan is supposed to pass through the optic disc center. Parameter, s, is a constant to control the penalty when the input HD-5LR scan is not centered well on the optic disc, which means the central B-scan is not the third B-scan; in this work, $s = 4$).

5.3.4 Experimental Methods and Results

Twenty-five subjects with optic disc edema having both SD-OCT ONH-centered volumetric and HD-5LR scans available from the University of Iowa were included in this study, where the SD-OCT volumetric measurement for all the subjects was larger than 14.42 mm^3, which is the mean total ONH volume of Frisén grade 2 in [7]. Layer segmentation in the volumetric and HD-5LR scans were separately performed using 3D and 2D graph-based methods. Based on the segmentation results, the SD-OCT volumetric and HD-5LR scans were registered together [34]. Fig. 5.11 demonstrates an example of the BMO estimation from an HD-5LR B-scan to the SD-OCT RPE *en-face* image domain. After obtaining five sets of BMO points from approaches 1

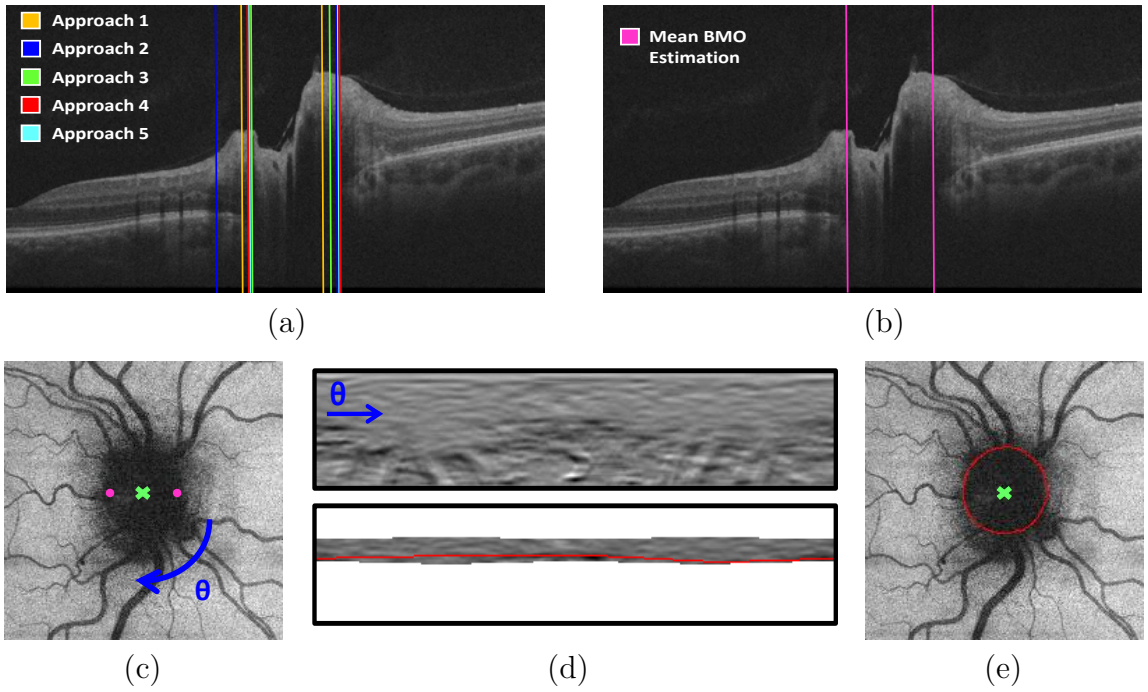

Figure 5.11: BMO estimation from the HD-5LR central B-scan to the SD-OCT RPE *en-face* image. (a) Five BMO candidates from Approach 1 to 5. (b) Mean BMO estimation from the closest three candidates. (c) SD-OCT *en-face* image with registered BMO points (pink dots) and its halfway point (green cross). (d) Top: The cost image in the radial domain; Bottom: Segmentation result on the modified cost image with the constraints of the BMO shape and size. (e) Segmented BMO contour in the *en-face* image.

to 5 [Fig. 5.11 (a)], the mean BMO set was obtained by averaging the closest three candidates at the nasal and temporal sides, separately [pink lines in Fig. 5.11 (b)]. Then, these two points were transferred into the SD-OCT RPE *en-face* domain, the halfway point was used as the unwrapped center [in Fig. 5.11 (c), pink dots are the BMO points and the green cross is the halfway point]. Next, an unwrapped gradient cost image was generated [Fig. 5.11 (d), top], and the segmented BMO is shown in the cost image with the optic disc size constrained [Fig. 5.11 (d), bottom]. Finally, wrapping back the segmentation result from the previous step, a segmented BMO contour was obtain in the SD-OCT RPE *en-face* image domain [Fig. 5.11 (e)].

To allow for the input HD-5LR scan being slightly off from the optic disc center,

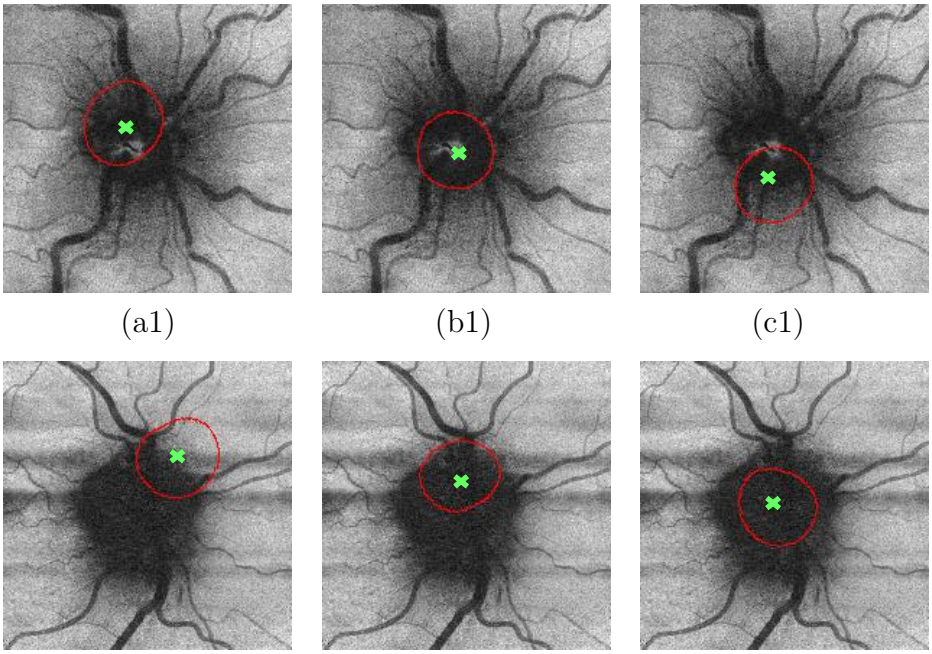

Figure 5.12: Two examples of the estimated BMO contours from the second (a), third (b) and fourth (c) HD-5LR B-scans. In case 1 (top row), the HD-5LR scan was centralized well, which means the third B-scan passing through the center of the optic disc (b1). In case 2 (bottom row), it was the fourth B-scan (c2) passing through the optic disc center instead of the third one (b2).

this BMO-segmentation process (Fig. 5.11) was reapplied to the second, third and fourth HD-5LR B-scans. Fig. 5.12 shows the estimated BMO contours in the three central B-scans from two subjects; the top-row example represents an input HD-5LR scan that was reasonably well centered on the optic disc [i.e., the third B-scan, Fig. 5.12 (b1), passes through the center of the optic disc]. On the other hand, the bottom row in Fig. 5.12 demonstrates a case of an off-centered HD-5LR scan, for which the fourth B-scan passed through the optic disc center [Fig. 5.12 (c2)].

To validate the results, the segmented BMO contours in the SD-OCT RPE *en-face* image domain from the traditional graph-based method [66], the semi-automated method (using six manual landmarks [34]), the proposed fully automated method, and the manual tracings were compared. During the manual tracing process, an

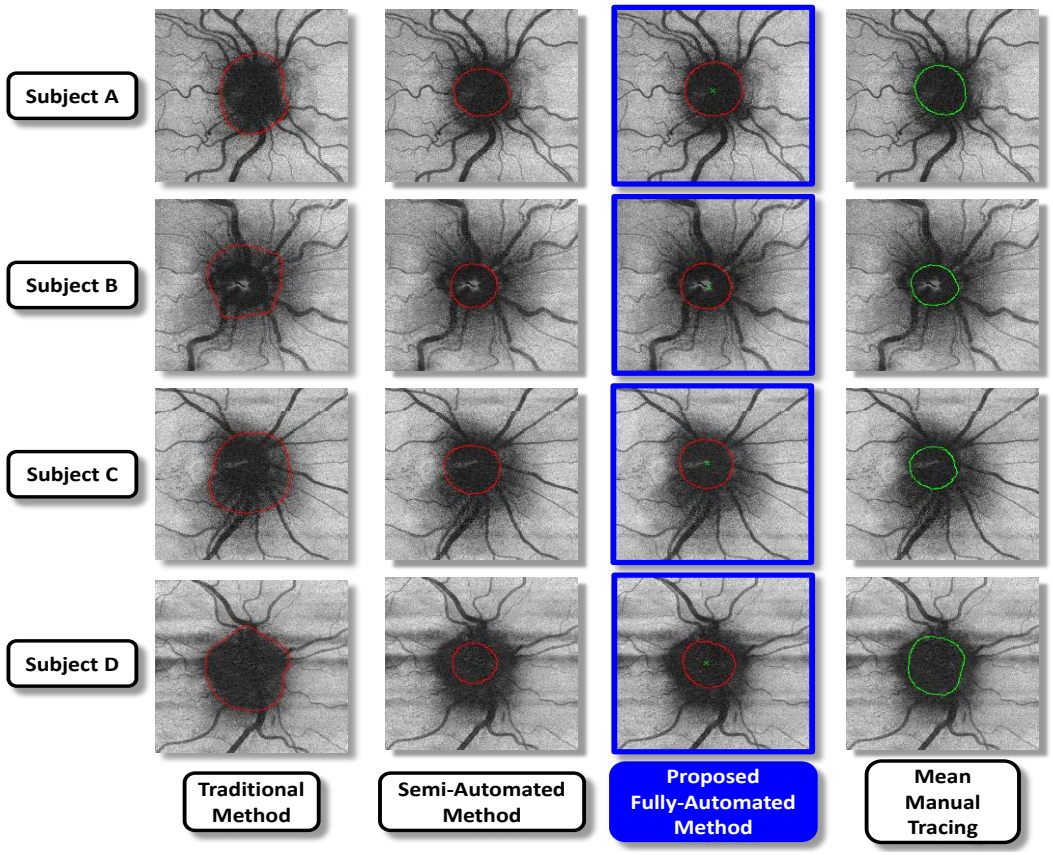

Figure 5.13: Comparisons among the traditional method, semi-automated method, proposed fully automated method and mean manual tracing.

independent observer separately traced the BMO points in the radially transformed SD-OCT domain at every 30° (i.e., 12 manual landmarks per volumetric SD-OCT scan) twice. By interpolating these 12 manual landmarks, the manually traced BMO contour in the SD-OCT RPE *en-face* image domain was obtained [34]. Fig. 5.13 shows examples of qualitative results for the traditional method, semi-automated method, the proposed fully automated method and the mean manual tracing.

For quantitative validation, the signed and root-mean-square (RMS) differences in pixels at every 30° in the unwrapped *en-face* domain between the mean manual tracing (MMT) and 1) the traditional method (TM), 2) the semi-automated method (SAM), and 3) the proposed fully automated method (FAM) were computed (Table 5.2). The

Table 5.2: Summary of signed/RMS BMO positioning differences in pixels[†, ‡].

	TM & MMT	SAM & MMT	FAM & MMT	MT1 & MT2
Signed	18.01 ± 8.32	-2.98 ± 4.55	-0.71 ± 5.58	-0.83 ± 2.55
RMS	21.31 ± 3.87	5.34 ± 3.27	6.64 ± 3.57	4.22 ± 1.97

[†] Mean ± SD in pixels for 25 centralized SD-OCT image pairs with optic disc edema, where the pixel size is 30×30 μm.

[‡] TM: Traditional Method; SAM: Semi-Automated Method; FAM: Fully Automated Method; MMT, MT1, MT2: Mean, First and Second Manual Tracing, respectively.

difference between the first and second manual tracing (MT1 and MT2) were also provided as a reference. The signed differences (mean ± standard deviation) between TM & MMT, SAM & MMT, FAM & MMT and MT1 & MT2 were 18.01 ± 8.32, -2.98 ± 4.55, -0.71 ± 5.58 and -0.83 ± 2.55, respectively; The RMS differences in the same order were 21.31 ± 3.87, 5.34 ± 3.27, 6.64 ± 3.57 and 4.22 ± 1.97, respectively. The mean RMS difference was significantly smaller using SAM and FAM when compared to TM ($p < 0.01$). Also, the mean RMS difference between SAM & MMT and FAM & MMT were not significantly different ($p = 0.19$).

5.3.5 Conclusions

When optic disc swelling is more severe, the visibility around the BMO region deteriorates in OCT images. Under this circumstance, directly and accurately segmenting BMO is extremely challenging. On the other hand, HD-5LR scans provide a better image quality in separate 2D B-scans but lacks for the 3D contextual information. In this work, a fully automated method is proposed to segment the BMO contour in the SD-OCT RPE *en-face* domain using a graph-based algorithm using optic disc shape-prior and size constraints with the combined information from the SD-OCT volume and HD-5LR image pairs. Comparing the fully automated method to the semi-automated method, the RMS difference between FAM & MMT does not

significantly differ from the RMS difference between SAM & MMT. Future work will include developing a new method with the ability to directly provide the BMO segmentation in the original volumetric SD-OCT image domain instead of in the RPE *en-face* image domain.

CHAPTER 6
TWO- AND THREE-DIMENSIONAL SHAPE MODELS OF BRUCH'S MEMBRANE FOR PAPILLEDEMA EYES (AIM 3)

6.1 Introduction

Previous studies have reported that the shape of the peripapillary retinal pigment epithelium and/or Bruch's membrane (pRPE/BM) layer may indirectly reflect the change in intracranial pressure. Specifically the shape of the pRPE/BM layer in patients with intracranial hypertension is displaced anteriorly toward the vitreous and this shape difference is not otherwise explained by disc edema alone [14, 26]. Additional interventions that lower the intracranial pressure [e.g. spinal tap, shunting procedure or a medical treatment for idiopathic intracranial hypertension (IIH)] will displace the pRPE/BM layer posteriorly away from the vitreous [14, 15, 26]. In the original method for generating the pRPE/BM shape model, equidistant landmarks are manually measured and placed on the pRPE/BM surface using the central HD-5LR B-scan for each available subject [14]. However, the manual processes are time-consuming and are not suitable for large datasets.

There is a recently completed clinical trial involving large amount of subjects with IIH. The idiopathic Intracranial Hypertension Treatment Trial (IIHTT) is a multi-center, randomized, double-masked, placebo-controlled, clinical trial that demonstrated the effectiveness of acetazolamide plus weight management in improving the visual field and quality of life of 165 patients with IIH and mild vision loss [18, 19]. An OCT sub-study was further designed to explore continuous structural parameters to quantitatively monitor the changes over time in the optic-nerve-head (ONH) and macular regions [11, 12, 68]. Although the OCT sub-study shows that the standard OCT measures of papilledema are reliable and responsive to the effects of acetazolamide, the pRPE/BM shape measure had not been applied within this large-scale dataset before the works in this thesis.

Therefore, the **objective** of this chapter (Aim 3) is to develop a methodology that

accelerates the manual steps in the traditional method and thus makes a pRPE/BM shape analysis applicable to larger datasets. Also, the traditional method is a 2D analysis; in this chapter, a novel 3D pRPE/BM shape model is designed to include not only nasal and temporal but also superior and inferior pRPE/BM shape information. For the **publication of Aim 3**, the 2D pRPE/BM shape measure using the IIHTT dataset was published in [76] for illustrating the methodology and in [77] for displaying the pRPE/BM longitudinal shape changes between patient groups having diet control with and without acetazolamide treatment. The 3D shape model extension is published in [78].

6.2 Semi-Automated 2D Bruch's Membrane Shape Analysis in Papilledema Using SD-OCT

Papilledema is a type of optic-nerve-head swelling due to elevated intracranial pressure and can be difficult to differentiate from other causes of optic disc edema. Having non-invasive tests for raised intracranial pressure (thus potentially avoiding invasive and uncomfortable tests such as lumbar punctures) would be of tremendous benefit. Recent work has demonstrated that an inverted-U shape (towards the vitreous) of the retinal pigment epithelium and/or Bruch's membrane (pRPE/BM) as visible from SD-OCT scans of the optic disc may suggest raised intracranial pressure [13–15]. In the traditional method, Sibony et al. [14] used a statistical-shape analysis approach to demonstrate the presence of an overall inverted-U shape of the pRPE/BM in papilledema patients, whereas a V-shape was present in normals and patients with anterior ischemic optic neuropathy (another cause of optic disc edema). However, manually placing 10 equidistant landmarks from the Bruch's membrane opening (BMO) along the pRPE/BM surface in both the nasal and temporal directions (i.e., a total of 20 equidistant landmarks per pRPE/BM shape) is tedious, highly susceptible to intra- and inter-observer variation, requiring specific expertise,

and very time-consuming. Therefore, the traditional method is difficult to apply to larger datasets (for example, the IIHTT OCT sub-study dataset) due to these limitations.

The purposes of this work are: 1) to present a semi-automated approach using the HD-5LR B-scan with 20 pRPE/BM landmarks (only requiring two manual BMO landmarks at the nasal and temporal sides; the remaining 18 landmarks are automatically decided/placed on the pre-segmented pRPE/BM surfaces), 2) to compute a statistical shape model using the baseline OCT data from 116 patients in the IIHTT OCT sub-study, 3) to compare the shape parameters computed using the proposed semi-automated approach with those from a fully manual approach, and 4) to compute the sensitivity of the shape parameters obtained with the semi-automated approach with respect to placement of the two manual landmarks.

6.2.1 Manual Placement of BMO Points

In the IIHTT OCT sub-study [11, 68], the SD-OCT HD-5LR and regular volumetric scans (Carl Zeiss Meditec, Dublin, CA) are the captured images of the ONH. Fig. 6.1 (a, b) and (c, d) show the differences in BMO visibility from a non-swollen and swollen optic disc in both SD-OCT protocols, respectively. Although the BMO points are visible in both protocols in the non-swollen case [Fig. 6.1 (a, b)], it should be noted that the HD-5LR central B-scans [Fig. 6.1 (d)] show much better BMO visibility than the central B-scans of the regular volumetric scans [Fig. 6.1 (c)] in cases of optic disc swelling. Therefore, the 2D pRPE/BM shape model in this work is built using the HD-5LR central B-scan.

The first step is to resize the HD-5LR central B-scan to reflect the physical aspect ratio and then manually place two BMO points. Specifically, the central B-scan from each subject in the IIHTT OCT substudy [11, 68] is first resized to reflect the 9:2 width-to-height ratio of the physical dimensions (from 1024×1024 to 4608×1024 in this work). Then, the GNU Image Manipulation Program (GIMP, version 2.8.10) is

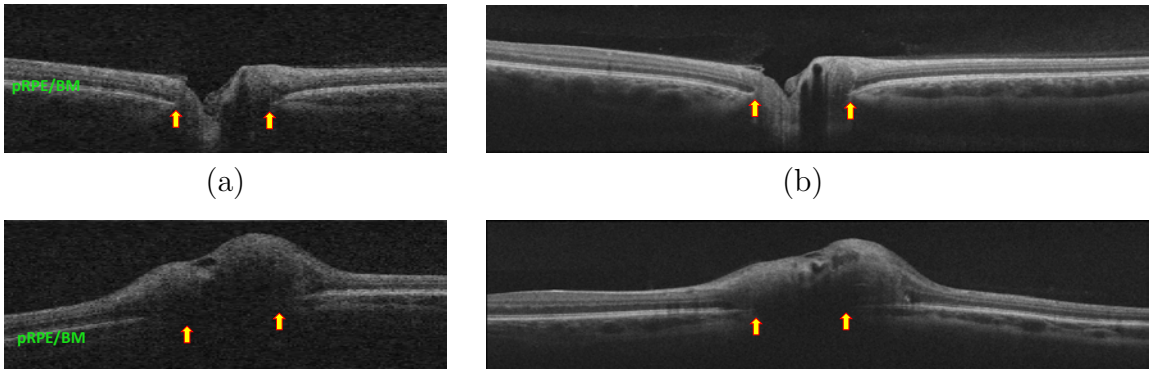

(a) (b)

(c) (d)

Figure 6.1: Increased visibility of BMO in the HD-5LR scan when compared to the regular volumetric scan, where (a) is the central B-scan from a volumetric SD-OCT image in a non-swollen optic disc, (b) is the central B-scan from the corresponding HD-5LR scan, (c) is the central B-scan from another volumetric SD-OCT image in a swollen optic disc, and (d) is the central B-scan from the corresponding HD-5LR scan. Note that the yellow arrows indicate the BMO points, and the physical dimensions of the B-scans of the volumetric and HD-5LR scans are 6×2 and 9×2 mm^2, respectively.

used to manually place two BMO landmarks for each available subject [i.e., the red dots in Fig. 6.2 (a, b)]. It is worthwhile to mention that this BMO placement is the only manual step in the proposed semi-automated method.

6.2.2 Automated Retinal Layer Segmentation and Semi-Automated Landmark Placement

After obtaining the BMO landmarks, automated retinal layer segmentation is performed using the previously discussed graph-search approach (Section 4.2.2 [7,72]) to obtain the internal limiting membrane (ILM) and pRPE/BM boundary. Fig. 6.2 (c) shows an example of the segmentation results, where the red boundary is the ILM, the green boundary is the pRPE/BM, and the two red dots are the manually placed BMO points from the previous step.

Next, on each half of the B-scan (i.e., the nasal and temporal sides), starting with the manually placed BMO landmark (i.e., one of the red dots), nine additional equidistant points [the yellow dots in Fig. 6.2 (d) on each side] are automatically

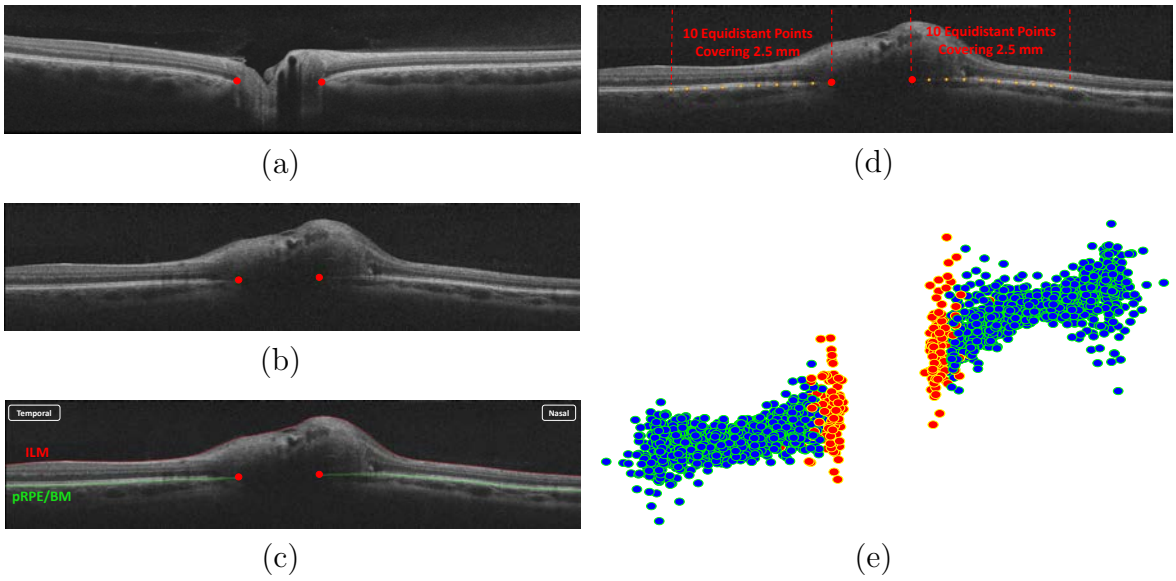

Figure 6.2: Example steps of the proposed semi-automated method, where (a) and (b) displays the manual BMO points in the non-swollen and swollen cases, respectively, (c) shows the manual BMO points with the automated layer segmentation, (d) illustrates the remaining 18 automated equidistant landmarks, and (e) demonstrates the aligned shapes of all 116 right eyes from the IIHTT OCT substudy at baseline.

placed along the segmented pRPE/BM (the green boundary) to provide a total of 10 landmarks covering 2.5 mm in physical space. Thus, including both sides, there are a total of 20 landmarks (two manually placed BMO points plus 18 automatically placed landmarks), each with an x- and y-coordinate, to describe the pRPE/BM shape:

$$\mathbf{s_i} = (x_{i,1}, y_{i,1}, \ldots, x_{i,10}, y_{i,10}, x_{i,11}, y_{i,11}, \ldots, x_{i,20}, y_{i,20})^T, \tag{6.1}$$

where $1 \leq i \leq N$, and N represents the total number of the available input HD-5LR scans ($N = 116$ in this work).

6.2.3 Statistical pRPE/BM Shape Models

Procrustes analysis and principal component analysis (PCA) are the two main steps for generating statistical shape models [79]. In general, Procrustes analysis

includes scaling, rotation and translation to align shapes. However, in this work, in order to preserve meaningful distances between landmarks (as these landmarks are defined based on physical distances along the pRPE/BM from the BMO), all the input shapes are aligned only using the steps of rotation and translation (i.e., excluding the scaling step). Fig. 6.2 (e) illustrates the realigned 2D pRPE/BM shapes after Procrustes analysis without scaling, where the red dots indicate the manually placed BM points and the blue dots indicate the semi-automated landmarks. [Different colors of dots were used in Fig. 6.2 (e) for better visualization.]

After realigning all the available input pRPE/BM shapes, PCA is used to compute the statistical shape models; the mean pRPE/BM shape is computed by

$$\bar{\mathbf{s}} = \frac{1}{N}\sum_{i=1}^{N}\mathbf{s_i}\ , \tag{6.2}$$

where $\mathbf{s_i}$ indicates each individual shape. Then, the covariance matrix is obtained by

$$cov(\mathbf{s}) = \frac{1}{N}\sum_{i=1}^{N}(\mathbf{s_i}-\bar{\mathbf{s}})(\mathbf{s_i}-\bar{\mathbf{s}})^T\ . \tag{6.3}$$

Next, the eigenvectors ($\mathbf{e_i}$) of $cov(\mathbf{s})$ are calculated by solving

$$cov(\mathbf{s})\mathbf{e_i} = \lambda_i\mathbf{e_i}, \text{where } \mathbf{e_i}^T\mathbf{e_i} = 1. \tag{6.4}$$

The principal eigenvectors ($\mathbf{e_{L1}}, \mathbf{e_{L2}}, \mathbf{e_{L3}}$) with the largest three eigenvalues (λ_{L1}, λ_{L2}, λ_{L3}) enables the description of each reconstructed individual shape as

$$\widehat{\mathbf{s_i}} = \bar{\mathbf{s}} + \sum_{j=1}^{3} c_{\mathbf{s_{Lj}}}\sqrt{\lambda_{Lj}}\mathbf{e_{Lj}}\ , \tag{6.5}$$

where $c_{\mathbf{s_{Lj}}}$ is the shape coefficient corresponding to principal component $\mathbf{e_{Lj}}$.

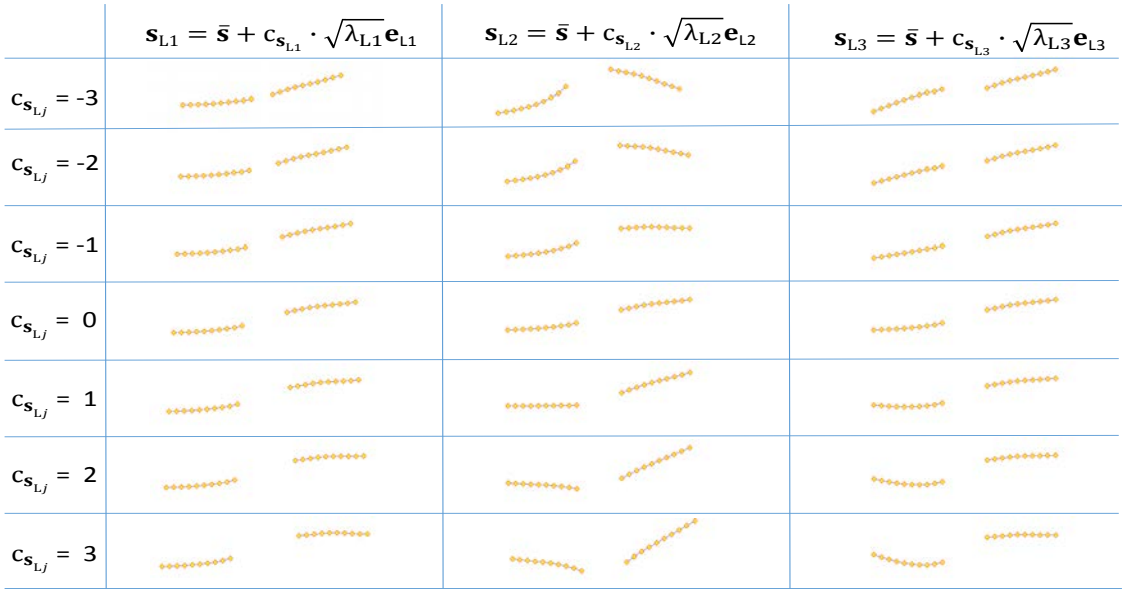

Figure 6.3: The pRPE/BM shape models with the effects of varying coefficients for the first three principal components (which contains 92.75%, 4.69% and 1.32% of the total energy) using IIHTT OCT sub-study baseline data (116 right eyes).

6.2.4 Experimental Methods and Results

In the IIHTT OCT sub-study, of the 126 subjects originally included [18], 116 had right-eye HD-5LR scans available in the baseline dataset. (In the IIHTT, the baseline data was prospectively collected from subjects at study entry prior to initiating treatment.) Fig. 6.3 illustrates the statistical shape models derived from right-eye baseline central B-scans from these 116 subjects. In particular, the shapes resulting from varying the coefficient of the first three principal components are shown. We can observe that the first principal component ($\mathbf{e_{L1}}$) roughly models the size of the BMO (with more positive values of the coefficient reflecting a larger BMO), the second principal component ($\mathbf{e_{L2}}$) models the pRPE/BM anterior/posterior directionality (with more negative values of the coefficient reflecting an inverted U-shaped pRPE/BM, meaning that the pRPE/BM tends to bend towards the vitreous, and more positive values reflecting a V-shaped pRPE/BM, meaning that the pRPE/BM tends to bend

away from the vitreous), and the third principal component models the degree of tilt. Of particular clinical interest for a given set of pRPE/BM landmarks is the coefficient ("shape measure") associated with the second principal coefficient. Figs. 6.4 and 6.5 demonstrate how the individual shape was reconstructed by the three principal components using Eq. (6.5) and how the pRPE/BM anterior/posterior measure ($c_{\mathbf{s_{L2}}}$) changes with different degrees of optic-nerve-head swelling due to intracranial hypertension. Fig. 6.6 provides more examples of the pRPE/BM shape with different values of $c_{\mathbf{s_{L2}}}$.

Shape measure $c_{\mathbf{s_{L2}}}$ was evaluated further in two experiments as follows: First, a subset of 20 central HD-5LR B-scans were selected from the original 116 eyes to cover the range of shape variations of the data. In Experiment I, all 20 landmarks were manually placed on each of these B-scans using the methodology described in [14] and then the resulting $c_{\mathbf{s_{L2}}}$ values using this fully manual approach were compared with those resulting from the proposed semi-automated approach using the same manually placed BMO points. In other words, the purpose of Experiment I was to compare the differences of the pRPE/BM shape measure for when all 20 landmarks are fully manually traced (i.e., a very time consuming process) versus two manually placed BMO points along with the 18 automatically placed landmarks (only requiring one to two minutes per B-scan).

In Experiment II, the sensitivity of the semi-automated approach in computing $c_{\mathbf{s_{L2}}}$ to the placement of the BMO landmarks was evaluated by having a second expert mark the two BMO points on the same 20 HD-5LR B-scans and comparing the resulting shape measures from the semi-automated method using expert 1's BMO points to those using expert 2's BMO points.

Table 6.1 shows the mean signed/unsigned differences of $c_{\mathbf{s_{L2}}}$ in Experiment I and II. In Experiment I, the mean signed difference ($\pm$ standard deviation) in the shape measure between the approach using all manual points and the proposed semi-

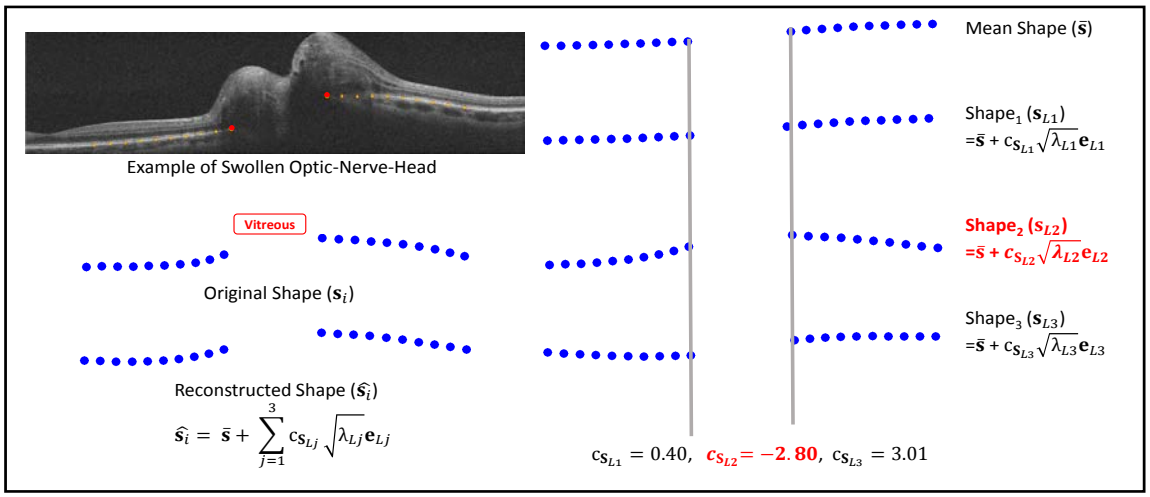

Figure 6.4: An example of pRPE/BM shape associated with a swollen optic disc reconstructed by the three principal components.

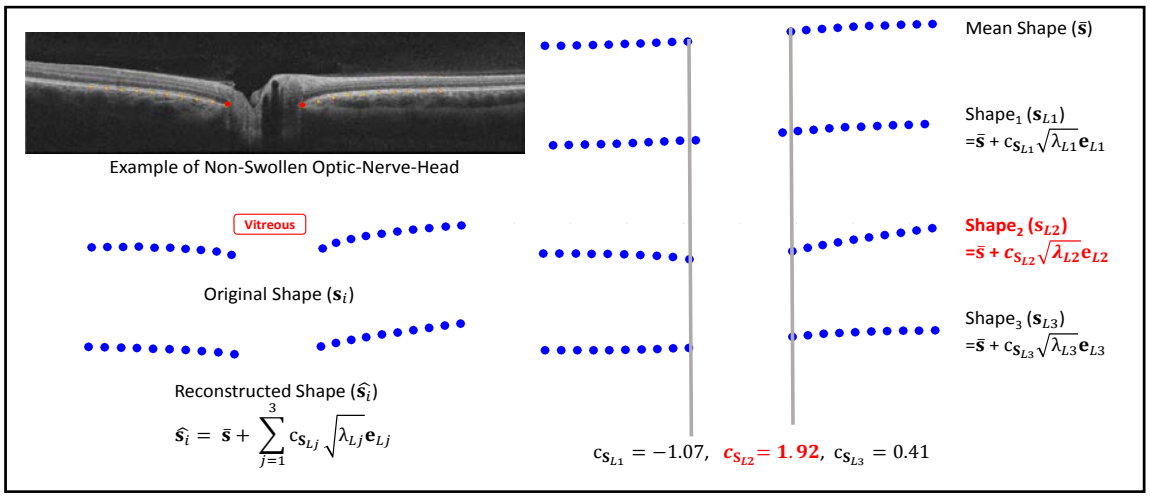

Figure 6.5: An example of pRPE/BM shape associated with a non-swollen optic disc reconstructed by the three principal components.

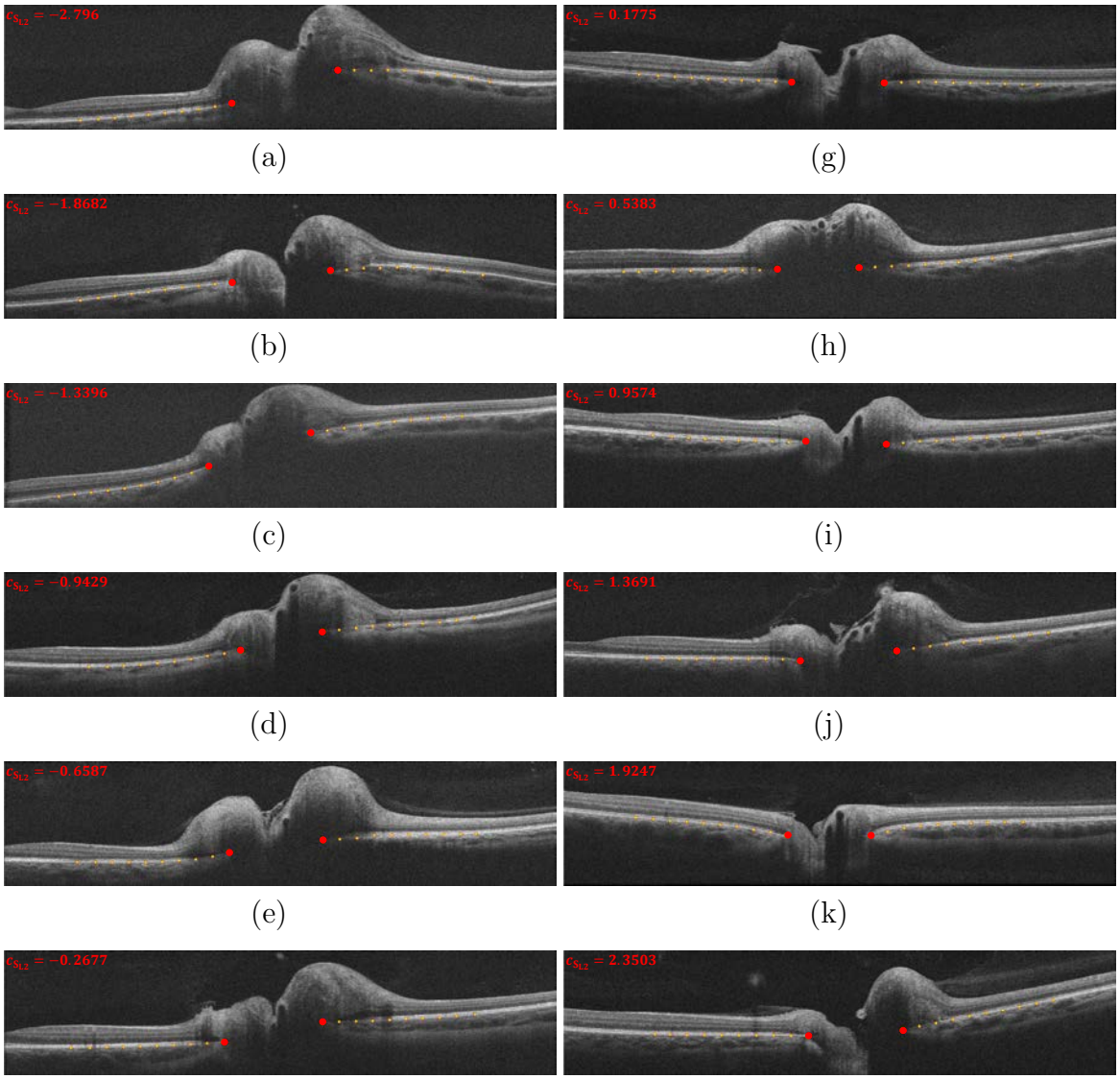

Figure 6.6: Examples of the pRPE/BM shape changing with varying $c_{\mathbf{s_{L2}}}$; the order is ranked by the values of $c_{\mathbf{s_{L2}}}$ from top-left to bottom-right.

automated approach was -0.182 (± 0.179), and the mean unsigned difference was 0.208 (± 0.147). The negative signed difference in Experiment I implies that the fully manual method tends to provide slightly smaller values of $\mathbf{s_{L2}}$ than the semi-automated method. In Experiment II, the mean signed difference (± standard deviation) between the proposed approach using BMO points provided by expert 1 and those provided by expert 2 was 0.039 (± 0.172), and the mean unsigned difference was 0.128 (± 0.118). The scatter plots and correlation coefficients in Experiment I and II are shown in Fig. 6.7 and also Table 6.1. The correlation coefficients in both experiments were ≥ 0.99.

Table 6.1: Results of the pRPE/BM Shape Measures ($c_{\mathbf{s_{L2}}}$) of Experiment I and II

	Mean Signed Difference (± Standard Deviation)	Mean Unsigned Difference (± Standard Deviation)	Corr. (p-value)
Expt I*	-0.182 (± 0.179)	0.208 (± 0.147)	0.991 ($p < 0.001$)
Expt II**	0.039 (± 0.172)	0.128 (± 0.118)	0.990 ($p < 0.001$)

* Comparison between fully manual and proposed methods (using the same manually placed BMO points).
** Comparison between two experts' BMO landmark points using the same semi-automated method.

6.2.5 Conclusions

The proposed semi-automated method dramatically expedites the current fully manual method by only requiring two manual BMO landmarks rather than 20 manual landmarks. This makes it feasible for the first time to analyze the pRPE/BM shape in large datasets (such as the longitudinal data for patients enrolled in the IIHTT).

The low mean signed/unsigned differences as well as the high correlations ($r \geq 0.99$) in both experiments demonstrate that the proposed method is robust and non-

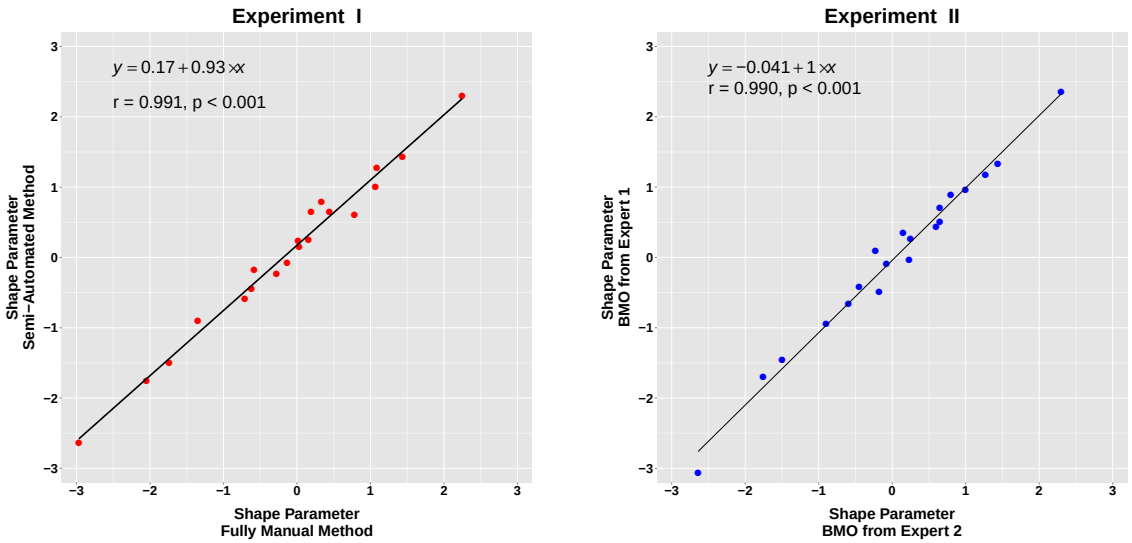

Figure 6.7: Scatter plots with linear regression equations and correlation coefficients (r-values) of Experiment I and II.

sensitive. In addition, applying the shape models in a large dataset ($N = 116$) strongly confirms that the pRPE/BM shape measure ($c_{\mathbf{s_{L2}}}$) indeed reflects different degrees of papilledema. When the value of the pRPE/BM shape measure ($c_{\mathbf{s_{L2}}}$) was negative, the inverted-U shape of the BM/RPE shape (toward the vitreous) indicated optic-nerve-head swelling due to raised intracranial pressure. This observation is consistent with the previous results from Sibony et al. [14, 15].

Overall, this work has presented a practical method to semi-automatically generate the pRPE/BM shape models using the HD-5LR central B-scan. Only two manual landmarks (plus the other 18 automatically decided landmarks on the pRPE/BM surface) are needed to obtain the pRPE/BM anterior/posterior shape measure. In future work, combining and comparing the pRPE/BM shape measure with other quantitative measurements (such as the Frišen scale grade, cerebrospinal fluid pressure, intraocular pressure, total retinal volume, retinal nerve fiber layer thickness, total retinal thickness, and treatment outcome) and performing a longitudinal analysis are expected to provide a comprehensive analysis of the pRPE/BM shape in cases

of optic-nerve-head swelling. Use of such shape models may also prove to be useful in other diseases affecting the ONH, such as glaucoma. In addition, the role of 3D shape models may also prove to hold additional benefits, which is what is discussed in the next section.

6.3 Semi-Automated 3D Bruch's Membrane Shape Analysis in Papilledema Using SD-OCT

Section 6.2 demonstrated that the 2D statistical shape model of the peripapillary retinal pigment epithelium and/or Bruchs membrane (pRPE/BM) can quantify the degree to which the pRPE/BM is oriented towards the vitreous in papilledema eyes, providing a potential non-invasive measure of raised intracranial pressure. However, due to the limitations of the amount of B-scans in an HD-5LR scan, the pRPE/BM shape measure in the previous section could only be computed in 2D. In this work, this 2D semi-automated method is extended to a 3D version, using the regular ONH volumetric image and prior-knowledge of the Bruch's membrane opening (BMO) points from the corresponding HD-5LR central B-scan. The purpose of this work is not only to extend the 2D pRPE/BM shape model to a complete 3D version but also to correlate the 2D and 3D shape measures using the IIHTT right eye baseline dataset.

6.3.1 Automated Retinal Layer Segmentation and Registration in SD-OCT

Both ONH-centered HD-5LR and volumetric scans from the IIHTT right eye baseline dataset are separately segmented and registered using the methods in Section 5.2.1 and Section 5.2.2 [Fig. 6.8 (a, b, c)]. In order to simplify the alignment step (which will be discussed later in Section 6.3.3), an extra flattening step is added. In this work, the retina in each B-scan is flattened by a straight line only in the $\mathbf{x}$ direction, which is connected between the two ending points of the segmented BM surface. Fig. 6.9 is an example of the central B-scan before and after flattening, where

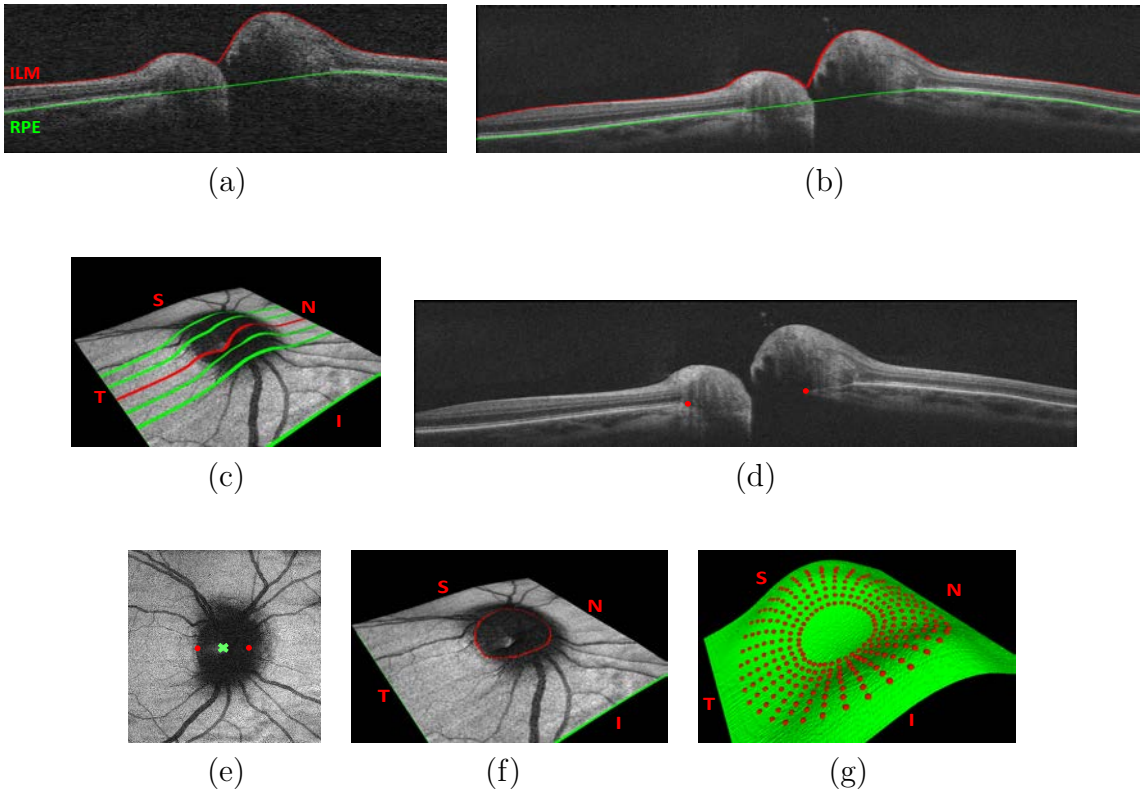

Figure 6.8: The pRPE/BM shape model sampling in 3D. (a, b) Examples of the layer segmentation in the central B-scan of an ONH-centered volumetric and HD-5LR scans, respectively. (c) Registration results of the volumetric and HD-5LR scan in 3D visualization, where the horizontal lines represent the HD-5LR B-scans; in particular, the red one represents the central B-scan. (d) Manual BMO placement in the central HD-5LR B-scan. (e) The mapping of the manual BMO landmarks, i.e., the red dots, in the flattened SD-OCT RPE *en-face* image, where the green cross is the estimated unwrapped center. (f) BMO segmentation in the flattened SD-OCT RPE *en-face* image. (g) BMO samples in 3D; non-isotropic view for better visualization.

the yellow line representing the reference line.

6.3.2 BMO Contour Segmentation and Sampling

Two BMO landmarks are manually placed at the nasal and temporal sides in each central HD-5LR B-scan using the same step as was discussed in Section 6.2.1 [Fig. 6.8 (d)]. Since the SD-OCT images are registered in the previous step, these two manual landmarks are directly converted into the flattened SD-OCT RPE *en-face*

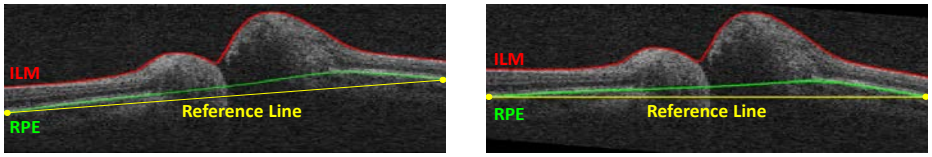

(a) (b)

Figure 6.9: Example of B-scan based flattening, where the yellow line is the reference line. (a) Before. (b) After.

image [Fig. 6.8 (e)]. Then, the RPE *en-face* image is unwrapped using the estimated center from the mapped BMO. Using the methods in Section 5.3.3, a cost image that considers the mean BMO size is generated. After applying a 2D graph-search algorithm, the BMO contour is segmented in the the flattened SD-OCT RPE *en-face* image [Fig. 6.8 (f)]. Then, starting with the segmented BMO contour from 0° to 359°, eight equidistant landmarks are automatically placed covering 1.5 mm in the radial direction for every 10° [Fig. 6.8 (g)]. Therefore, the amount of landmarks in the transition from 2D to 3D is increased from 20 to 288 landmarks. Each 3D pRPE/BM shape, which has a corresponding x-, y- and z-coordinate, can be described as:

$$\mathbf{s_i} = (x_{i,1}, y_{i,1}, z_{i,1}, \ldots, x_{i,288}, y_{i,288}, z_{i,288})^T, \tag{6.6}$$

where $1 \leq i \leq N$, and N represents the total number of the available input B-scans ($N = 116$).

6.3.3 Statistical pRPE/BM Shape Models

As we discussed in Section 6.2.3, Procrustes analysis and principal component analysis (PCA) are the two main steps to generate the statistical shape model. Due to the nature of SD-OCT images, the orientation of all these images is fixed. Therefore, in this work, the step of Procrustes analysis is achieved by only cascading all the centers of all 116 3D pRPE/BM shapes (Fig. 6.10). Then, as in Section 6.2.3, the first

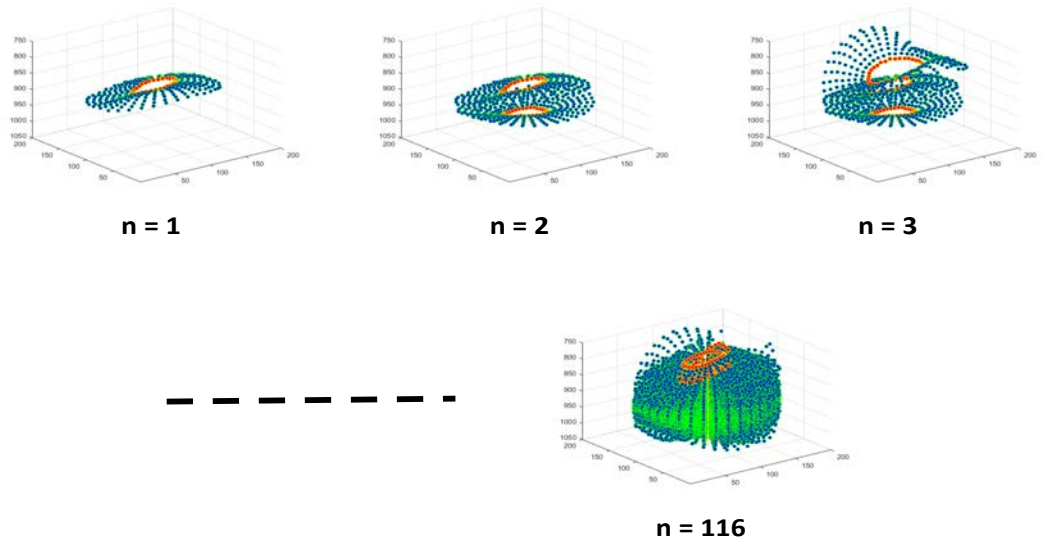

Figure 6.10: Examples of 3D pRPE/BM shape alignment in 116 IIHTT baseline right eyes.

three principal eigenvectors ($\mathbf{e_{L1}}$, $\mathbf{e_{L2}}$ and $\mathbf{e_{L3}}$) are extracted so that the pRPE/BM shape models are generated along with the varying coefficients ($c_{\mathbf{s_{L1}}}$, $c_{\mathbf{s_{L2}}}$ and $c_{\mathbf{s_{L3}}}$).

6.3.4 Experimental Methods and Results

The HD-5LR and volumetric scans from the 116 IIHTT baseline right eyes mentioned in Section 6.2.4 were used to generate 3D pRPE/BM shape models. For each available eye, the steps, including image segmentation, image registration, and image flattening, were performed using the methods in Section 6.3.1. Next, the processes of manually placing two BMO points and automatically deciding the remaining landmarks (i.e., 3D sampling) were done by following the steps in Section 6.3.2. Finally, based on the segmented BMO contour in the SD-OCT RPE *en-face* image, by applying the steps in Section 6.3.3, the 3D pRPE/BM shape models were built, and the shape measures were computed. Fig. 6.11 shows the first three components of the 3D pRPE/BM shape models (which contains 83.6%, 6.8% and 4.8% of the total energy); in particular, the first principal component, $\mathbf{e_{L1}}$, models the pRPE/BM ante-

rior/posterior directionality, the second principal component, $\mathbf{e_{L2}}$, roughly represents the degree of retinal tilt, and the third principal component, $\mathbf{e_{L3}}$, shows the degree of rotation. In this work, the first principal component is particularly interesting for the clinical need (it is similar to the second principal component in the 2D pRPE/BM shape model; Fig. 6.2), so it will be referred as the 3D pRPE/BM shape measure in the following discussion. The correlation between the 2D and 3D pRPE/BM shape measures was 0.8 (p-value < 0.01), and the scatter plot is shown in Fig. 6.12.

6.3.5 Conclusions

The pRPE/BM shape measures in 2D and 3D are new parameters to potentially monitor optic disc edema severity due to raised intracranial pressure. The 3D shape model uses significantly more landmarks than the 2D shape model (2D: 20 landmarks; 3D: 288 landmarks), so the 3D model may be more robust to noise. In addition, the 3D shape model involves contextual information. Compared to the 2D shape model, which only represents the nasal and temporal information, the 3D shape model additionally represents the superior and inferior information. Although there are promising advantages in the 3D pRPE/BM shape model, more validations will be needed in ongoing studies. Future work includes developing a fully automated method and observing relationships among 2D/3D pRPE/BM shape measures and other clinical measures over time, including intracranial pressure (ICP), and visual field sensitivity.

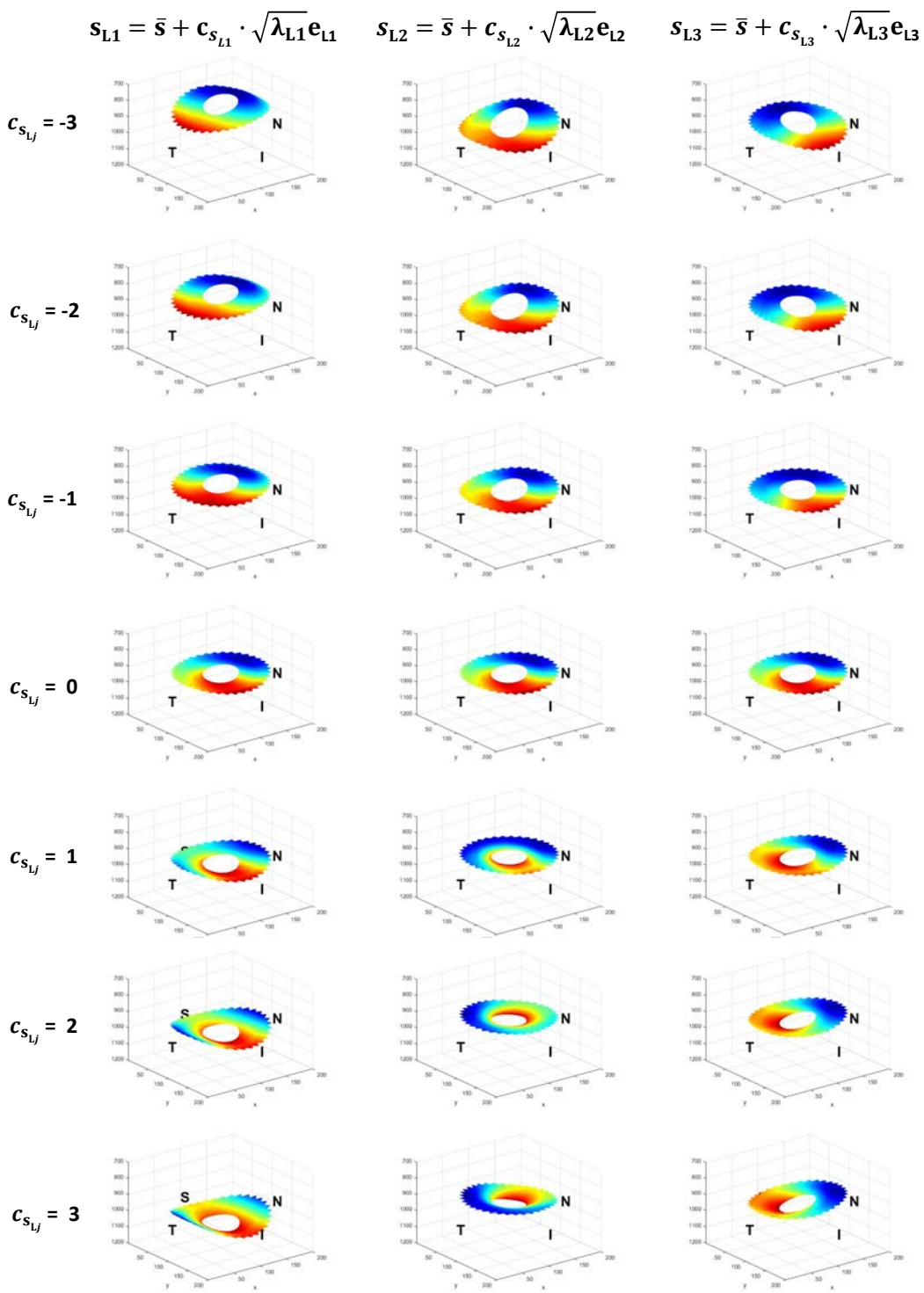

Figure 6.11: pRPE/BM 3D shape models with the effects of varying coefficients for the first three principal components (which contains 83.6%, 6.8% and 4.8% of total energy) using IIHTT OCT sub-study baseline data (116 right eyes).

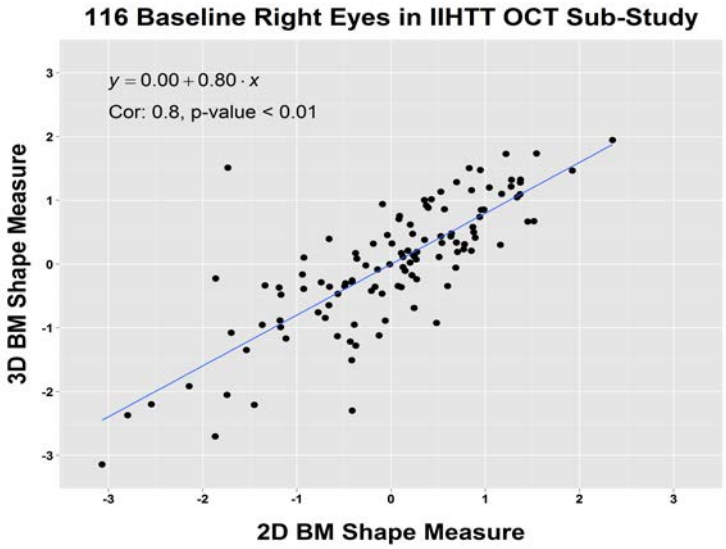

Figure 6.12: Comparison between 2D and 3D BM shape measures.

CHAPTER 7
QUANTITATIVE MEASUREMENTS OF PAPILLEDEMA SEVERITY (AIM 4)

7.1 Introduction

The Frisén grading scheme [a scale from 0 (normal) to 5 (severe)] is the standard approach that ophthalmologists often use to qualitatively assess the severity of papilledema by examining the features of the retina in a fundus image or direct funduscopic observation [3]. These retinal features are usually regional and not straightforward to quantify, such as the blurriness and color-change at the region around the Bruch's membrane opening (BMO), the tortuosity of vessels, and the presence of a C-shaped halo. Therefore, this qualitative method comes with the limitations such as high intra/inter-observer variability, low reproducibility, need for specific expertise, and non-continuous outputs [4–7].

Machine learning is a relatively new idea in the field of medical image processing. These algorithms are designed to let computers "learn" the decision criteria from an independent input dataset (i.e., the training set) and use the "learned criteria" to mimic how human experts make the decision in future datasets (i.e., the testing set). In the case of assessing the severity of papilledema, the machine-learning technique may provide a new perspective to overcome the limitations of the qualitative Frisén grading system. Instead of experts inspecting a patient's retina and directly deciding the degree of the optic disc edema, computers with machine-learning algorithms would have the ability to semi-/fully automatically compute all the pre-decided features from the input images and then output a severity score based on the pre-learned criteria. To achieve this goal, these computers, first, need to have the ability to compute the retinal features from the input images. Since SD-OCT has excellent potential for accessing cross-sectional information of the retina, certain quantitative measurements could be used as valuable input features for machine-learning algorithms, such as the total optic-nerve-head (ONH) volume, peripapillary retinal nerve fiber layer (pRNFL)

and total retinal layer (pTR) thicknesses, and 2D/3D peripapillary retinal pigment epithelium/Bruch's membrane (pRPE/BM) shape measures.

The **objective** of Aim 4 is to develop an automated machine-learning framework that can read retinal features from the input SD-OCT images, analyze the best feature combination, and output a score on a continuous scale to objectively reflect the disc-swelling severity. The correlation between the ONH volume and Frisén grades will be first addressed to demonstrate the relationship between the global optic disc volume and Frisén grade. Then, this idea is extended into using the combined features from the global and regional optic disc information to predict the Frisén grade. Finally, a comprehensive machine learning framework is proposed to involve all the available features to measure the papilledema severity on a continuous scale. The proposed system is expected to be more robust than the traditional Frisén grading scheme.

For **publication of Aim 4**, the comparisons among the Frisén grades, ONH volume, pRNFL and pTR thicknesses were published in [7]. Then, these OCT measurements were used in an OCT sub-study of Neuro-Ophthalmology Research Disease Investigator Consortium (NORDIC) Idiopathic Intracranial Hypertension Treatment Trial (IIHTT) to trace the ONH swelling changes in patients having diet control with/without the treatment of acetazolamide from baseline to six months [11, 12, 68]. In addition, the framework of predicting a Frisén grade using regional volumetric information was provided in [72].

7.2 Comparisons among Frisén Grades, ONH Volume, Peripapillary RNFL and TR Thicknesses

Because current commercial softwares do not have the ability to reliably segment retinal layers in cases of moderate to severe optic disc swelling, the 2D pRNFL and pTR thicknesses were only validated in mild-papilledema [4]. However, with the layer segmentation for severely swollen optic disc, in both SD-OCT HD-5LR and

volumetric images, introduced in Chapter 4, we can finally make fair comparisons among the Frisén grades, total ONH volume, pRNFL and pTR thicknesses.

7.2.1 Peripapillary RNFL and TR Thickness Measurements

With the segmentation results from Section 4.3, the mean pRNFL and pTR thicknesses are measured around a peripapillary circle with a radius of 1.73 mm (to match the same settings that Zeiss uses in the commercial Cirrus SD-OCT machines). In an unwrapped peripapillary 2D scan, the RNFL is the top layer (between the red and green surfaces in Fig. 7.1), and the TR thickness is defined by the space between the ILM and botRPE boundary (between the red and yellow surfaces in Fig. 7.1).

7.2.2 Total ONH Volume

Based on the segmentation results from Section 4.3, the total ONH volume is defined by the entire volumetric region (in mm^3) between the segmented ILM and botRPE surface in a complete SD-OCT scan (i.e., the space between the red and yellow surfaces in Fig. 7.2).

7.2.3 Frisén Scale Grade

All of the fundus photographs in this section have been graded by three independent neuro-ophthalmologists from the University of Iowa using the Frisén scale (from grade 0 to grade 4, in Fig. 7.2). The majority outcome is adopted when the original three judgments were not consistent (i.e., the "winner-takes-all" rule).

7.2.4 Experimental Methods and Results

Twenty-two patients with papilledema from the University of Iowa were enrolled in this study with a total of 86 image scans (including right and/or left eyes for different visit dates). Each patient had between two and four separate visit dates (12/22 subjects had two visits, 7/22 had three visits, and 3/22 had four visits), with

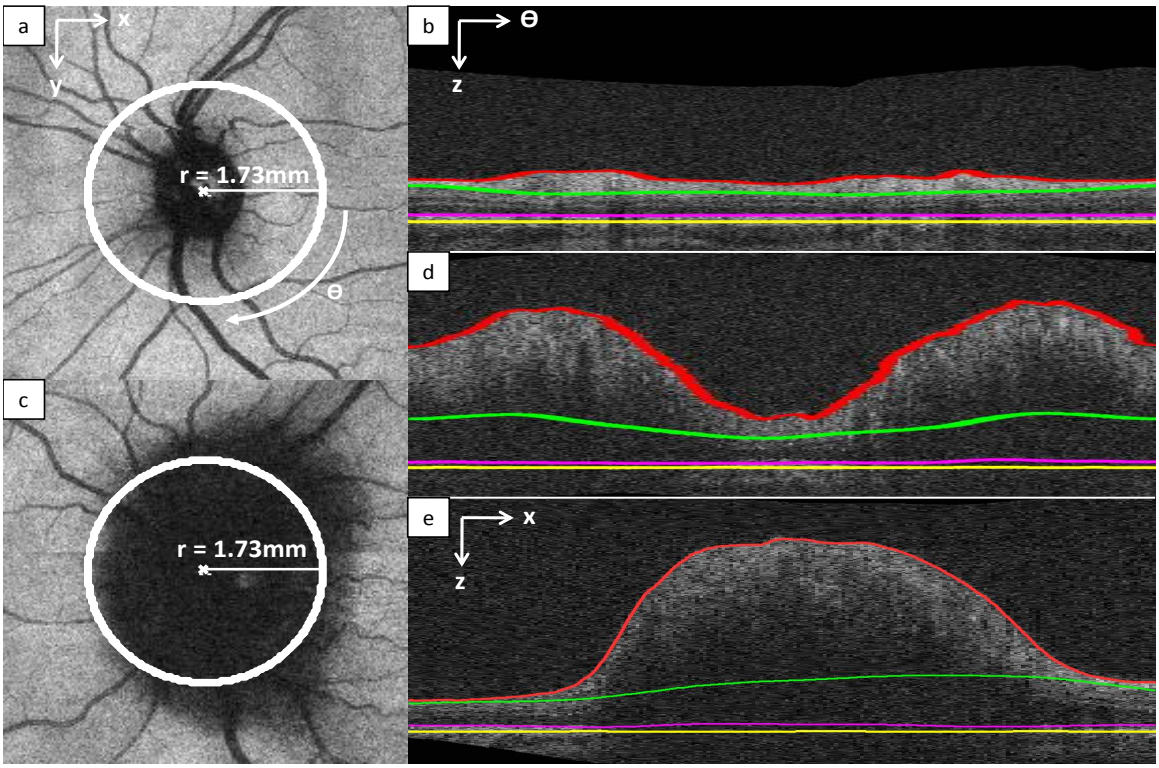

Figure 7.1: The locations of the peripapillary circle (as same as the commercial Zeiss Cirrus SD-OCT machines) and the layer segmentations in two different SD-OCT volumes with different levels of optic disc swelling. (a) The peripapillary circle (i.e., the white circle) in a non-swollen RPE *en-face* image. (b) The layer segmentation on the unwrapped peripapillary scan of (a). (c) The peripapillary circle in a swollen RPE *en-face* image, Frisén scale grade of 4. (d) The layer segmentation on the unwrapped peripapillary scan of (c). (e) The central B-scan of the same SD-OCT volume of (c), showing a sagittal cross-section through the center of the optic disc. The segmentation of the ILM border is depicted by the red line; the deeper, outer border of the RNFL by the green line; the photoreceptor boundary by the magenta line; and the retinal pigmented epithelial (RPE) border by the yellow line. In the region underlying the ONH (e), the borders are extrapolated using a thin-plate-spline (TPS) fit.

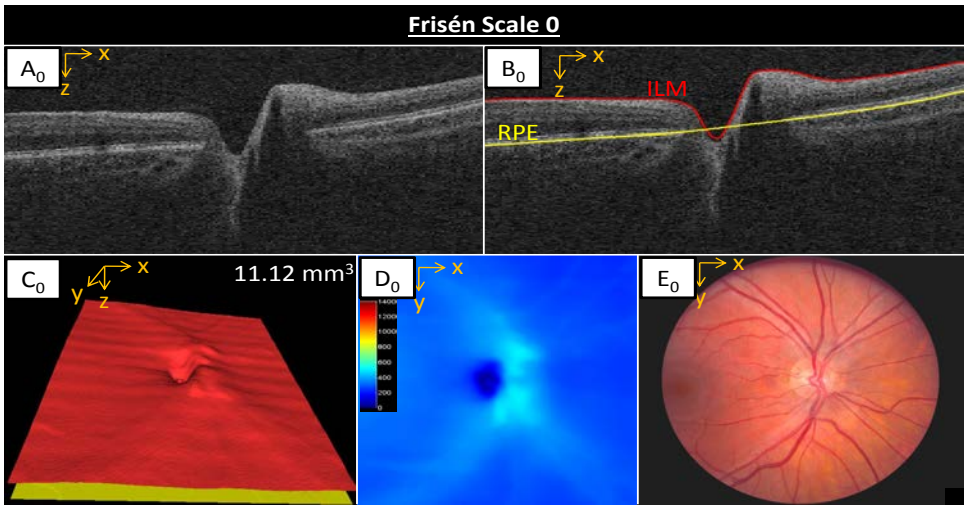

(a)

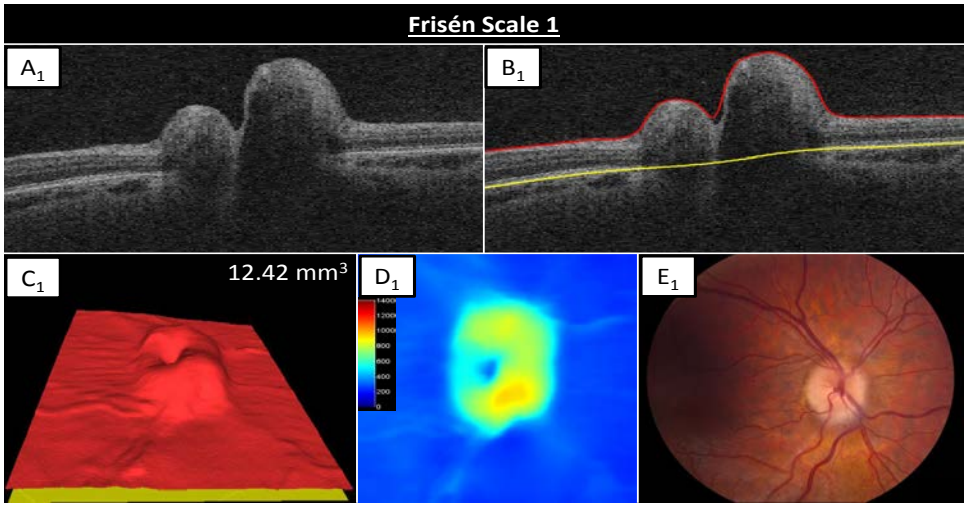

(b)

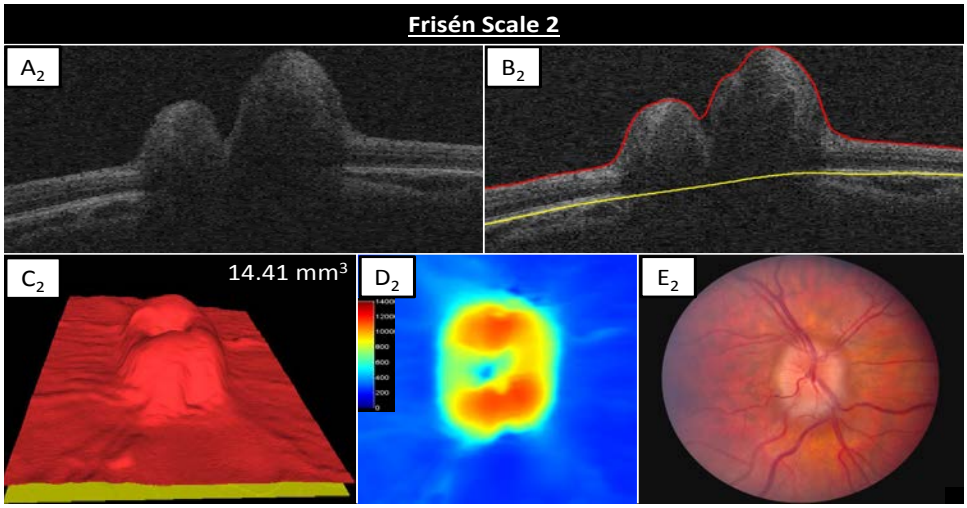

(c)

(Continued on next page)

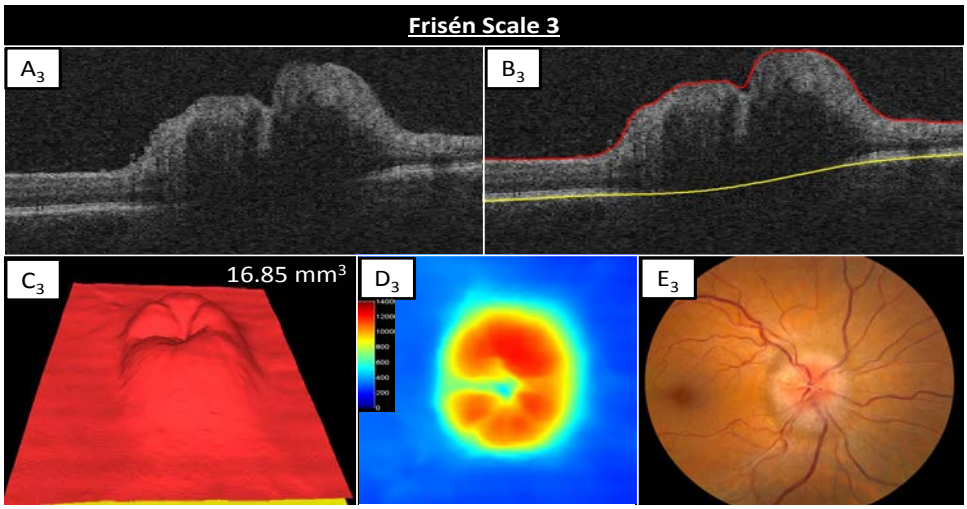

(d)

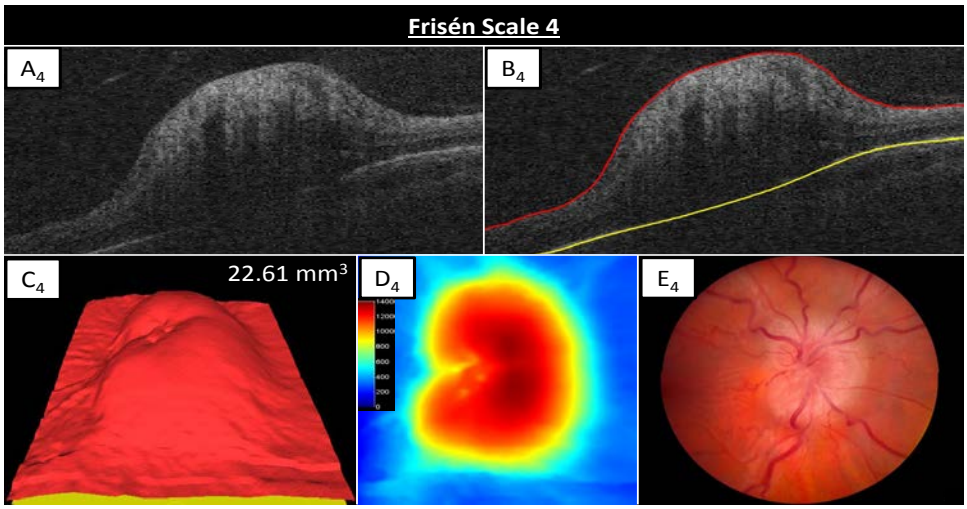

(e)

Figure 7.2: A composite example of papilledema cases of increasing Frisén scales (OD, from scale 0 to scale 4, shown as subscript) with their corresponding total ONH volumes derived from the 3D SD-OCT scans, where (A) the central B-scan of the original SD-OCT volume, (B) The layer segmentation of the ILM (the red surface) and lower bounding of the RPE surface (the yellow surface), (C) the 3D visualization of the entire SD-OCT volume, (D) the thickness map between the red and yellow surfaces, and (E) the corresponding fundus image.

the mean (± standard deviation) time interval between visits being 92 (± 80) days. In this original dataset, 5/86 (6%) had a Frisén grade of 0, 26/86 (30%) had a grade of 1, 33/86 (38%) had a grade of 2, 10/86 (12%) had a grade of 3, and 12/86 (14%) had a grade of 4. In defining these majority-rule grades, all three experts provided the same grade in 40/86 (47%) cases, one expert disagreed with the other two by one scale grade in 36/86 (42%) cases, one expert disagreed with the other two by two scale grades in 6/86 (7%) cases, and all three experts disagreed in 4/86 (5%) cases.

For all 86 scans, 15/86 (17%) of SD-OCT volumes were excluded because the scans did not contain the complete retinal tissue from the top of ILM to the bottom surface of the RPE complex due to operation errors. Summaries of the data inclusion and exclusion results are shown in Fig. 7.3. Of the remaining 71 volumes which were measured using the 3D graph-search algorithm (Section 4.3), 5 (7%) had a Frisén grade of 0, 25 (35%) had a grade of 1, 28 (39%) had a grade of 2, 8 (11%) had a grade of 3, and 5 (7%) had a grade of 4 (Table 7.1). There were no cases of Frisén scale 5, the severest grade of papilledema, in this dataset.

The mean (± standard deviation) resulting volumes for grade of 0 to 4 were 11.36 ± 0.56, 12.53 ± 1.21, 14.42 ± 2.11, 17.48 ± 2.63, and 21.81 ± 3.16 mm^3, respectively (Fig. 7.4 and Table 7.1). The Spearman rank coefficient between the ONH volume and Frisén grade was 0.74 ($p < 0.01$) (Table 7.1).

In the subsequent analysis, except for using our 3D algorithm, the mean pRNFL was also computed using Zeiss' algorithm, but 27/86 scans were excluded due to failures of segmenting the RNFL. Four additional scans were excluded using the original exclusion criteria (incomplete ILM or RPE included within the volume acquired within z-axis window of the SD-OCT scan), thus leaving 55 volumetric SD-OCT scans available for both our 3D and Zeiss' algorithms in the subsequent analyses, comparing the ONH volume with the pRNFL and pTR thicknesses (see Fig. 7.3 for data distribution). Using these 55 eyes, the computed Pearson's correlation coefficients

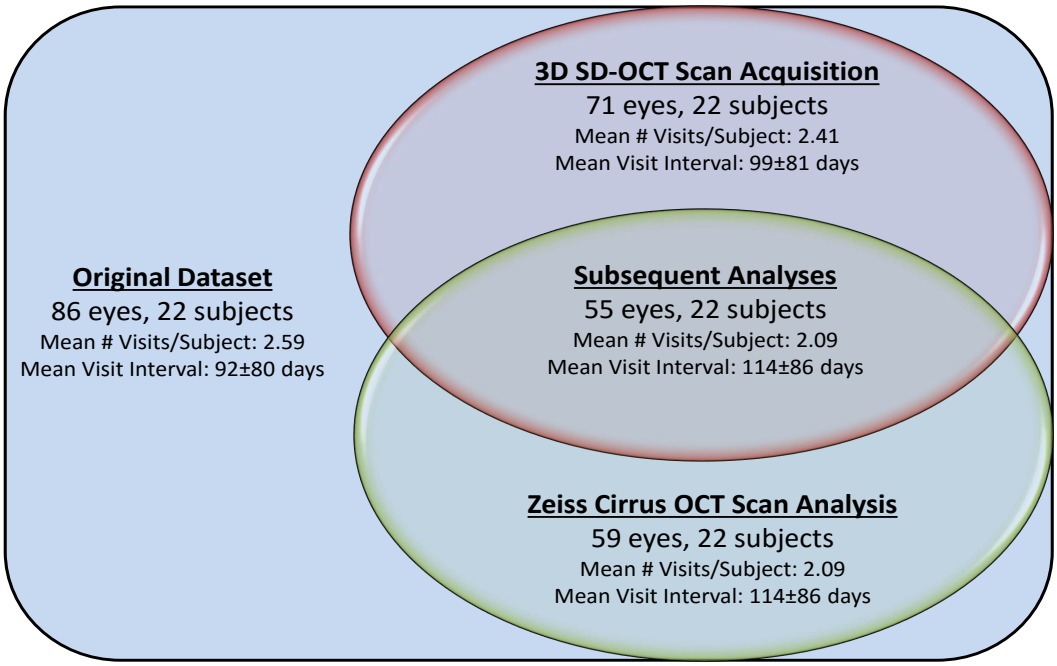

Figure 7.3: A Venn diagram shows the data used in section 7.2. The original dataset included 86 SD-OCT volumes and fundus photographs from 22 subjects. The exclusion of 15 volumetric scans (due to an incompletely acquired ILM or RPE in the confines of the **z** axis window) resulted in 71 volumetric SD-OCT volumes and fundus photographs from 22 subjects (indicated in red). This dataset was used for the first part of the study analyses. From the original dataset, the exclusion of 27 SD-OCT volumes due to the obvious failure of the SD-OCT scanner RNFL algorithm resulted in 59 volumetric SD-OCT volumes and fundus photographs from 22 subjects (indicated in green). This dataset was not directly used in the study analyses. The intersection of these two datasets (labeled "Subsequent Analyses") resulted in 55 SD-OCT volumes and fundus photographs from 22 subjects. This dataset was used for the remaining analyses. For each dataset, the mean number of visits per subject and mean time interval (± standard deviation) between visits is also shown.

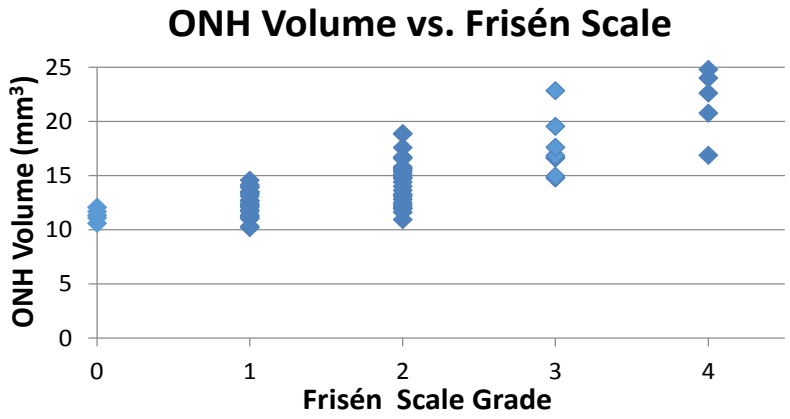

(a)

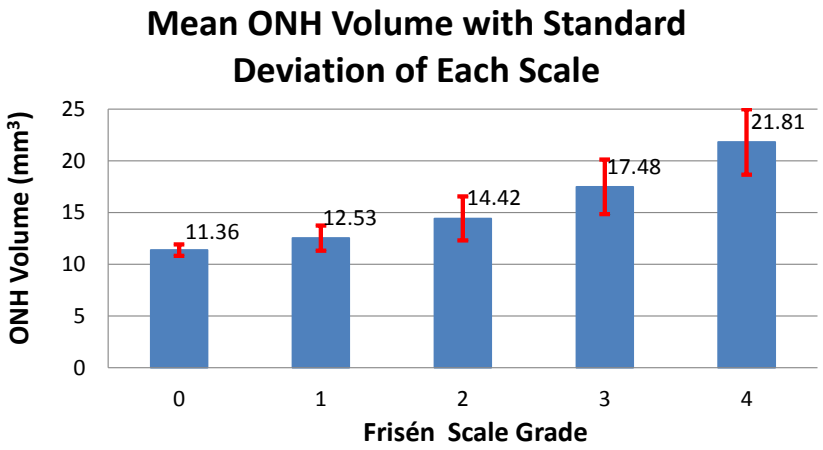

(b)

Figure 7.4: Papilledema grading differences in 71 eyes. (a) The scatter of the ONH volumes versus Frisén scales. (b) The mean ONH volumes with standard deviations of each Frisén scale.

Table 7.1: Distribution, mean volume and volume standard deviation of included SD-OCT scans for each Frisén grade of papilledema severity in 71 Eyes.

Frisén Scale	Number of Eyes	Mean Volume	Standard Deviation
0	5	11.36	0.56
1	25	12.53	1.21
2	28	14.42	2.11
3	8	17.48	2.63
4	5	21.81	3.16
Spearman's rank correlation coeffieient		$r = 0.74$	
Significant level		$p < 0.01$	
95% confidence interval		(0.61, 0.83)	
Total valid eyes		71	

(r) between the ONH volume and the mean pRNFL, pTR (based on our 3D segmentation algorithm in Section 4.3), and pRNFL (using the Zeiss Cirrus algorithm) thickness were 0.98, 0.93, and 0.95 (for all of them, $p < 0.01$), respectively (Fig. 7.5). The computed Pearson's correlation coefficients (r) between Zeiss pRNFL and our algorithm's mean pRNFL and pTR thickness measurements were 0.90 ($p < 0.01$) and 0.96 ($p < 0.01$), respectively (Fig. 7.5).

7.2.5 Conclusions

Intuitively, volumetric estimation is a straightforward approach for measuring papilledema, because papilledema manifests as swelling of the peripapillary retina and optic nerve. Since the volumetric measurement is based on a 3D approach, more image information is available in voxel format compared to the pixel format of a 2D thickness measurement (such as the transnational peripapillary RNFL and TR thickness measurements). Also, the measurement of 3D ONH volume would be expected to be more resistant to local artifacts or to isolated algorithm perturbations affected by a low signal to noise ratio in areas of the OCT scan. In summary, the total ONH volume rendered from 3D OCT scans appears to provide an excellent

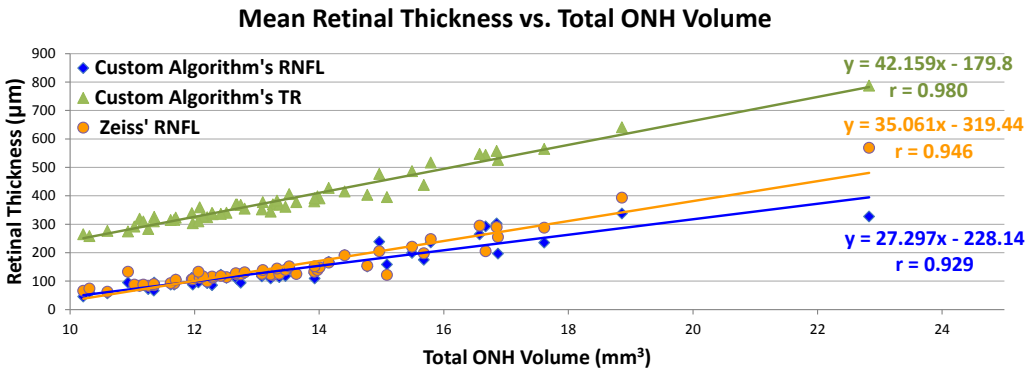

(a)

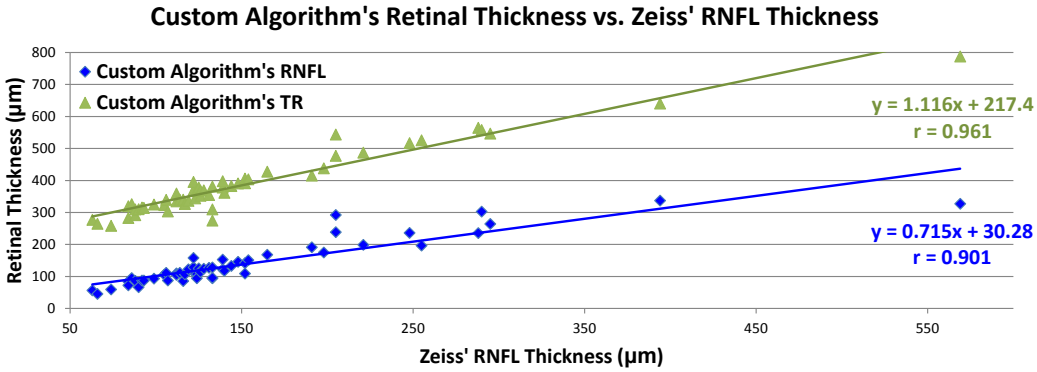

(b)

Figure 7.5: Measurement correlations between the total ONH volume and pRNFL and pTR thicknesses in 55 eyes from the subsequent analysis dataset. (a) Compares Zeiss' pRNFL and our pRNFL and pTR thicknesses with the total ONH volumetric measurement. (b) Compares the relationship between our algorithm's pRNFL and pTR thicknesses with Zeiss' pRNFL thickness.

continuous scale measurement of optic disc edema and changes over time. More thorough discussions and details can be found in [7].

7.3 Automated 3D Region-Based Volumetric Estimation of Optic Disc Swelling in Papilledema Using SD-OCT

In the previous section, a high correlation between the ONH volume and Frisén grade ($r = 0.74$) shows that the global volumetric measurement can be a potentially good option to assess the severity of papilledema. However, the region-based volumetric measurements were not addressed in the previous discussion. Because the regional features are often helpful in the expert-determination of Frisén scale grades from fundus photographs and considering the recent automated fundus-based analyses [5], these features can be expected to contribute in an OCT-based papilledema severity prediction system as well. Therefore, in this work, a machine-learning approach is proposed to use a fuzzy k-nearest-neighbor (k-NN) classifier to predict the Frisén grade for each input SD-OCT volumetric scan using the retinal features including not only the ONH volume, mean pRNFL and pTR thicknesses (as were discussed in the previous section) but also the newly added region-based volumetric measurements (i.e., the nasal, superior, temporal, and inferior volumes). The final selected features are decided by sequential forward feature selection and tested using a leave-one-subject-out cross validation method.

7.3.1 Automated Retinal Layer Segmentation and Swollen Region Segmentation

All the input SD-OCT volumetric scans are segmented using the 3D graph-search that was discussed in Section 4.3, where the ILM, bottom surface of the RNFL and the RPE complex are the target surfaces. After the layer segmentation, the RPE *en-face* image is generated [Fig. 7.6 (a)] by averaging voxel intensities for each A-scan in the RPE layer. Fig. 7.6 (a, b) shows 2D and 3D visualizations, respectively. Next,

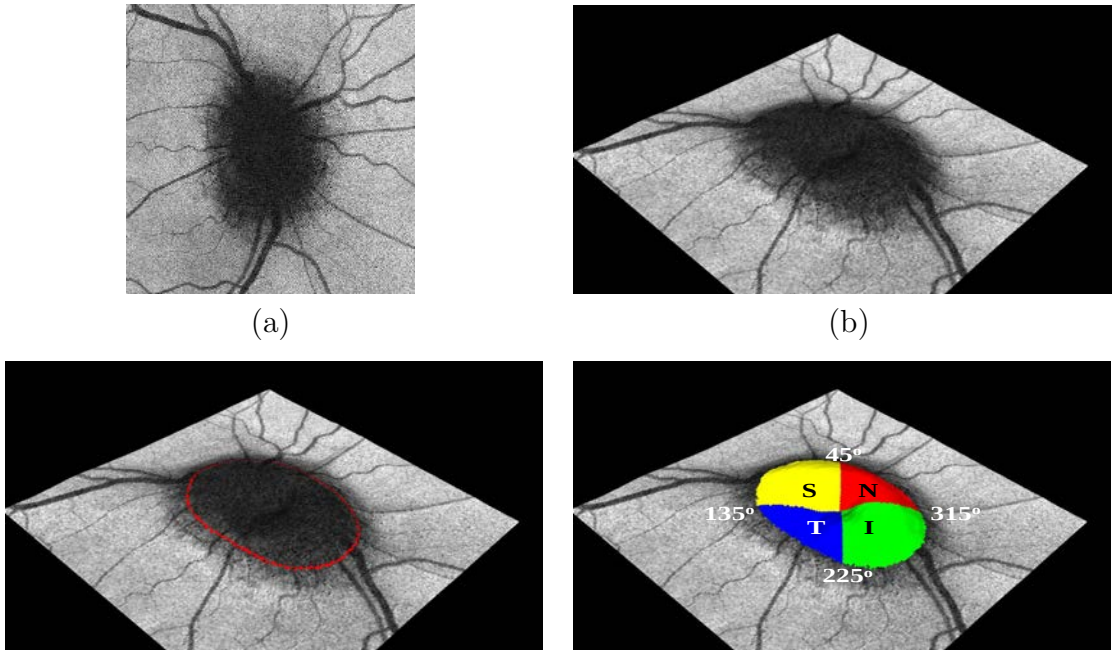

Figure 7.6: Steps of region-based volumetric estimation. (a) A RPE *en-face* image. (b) 3D visualization. (c) Segmentation of the swollen region. (d) A 3D color map of the region-based divisions, including the nasal (red), superior (yellow), temporal (blue), and inferior (green) areas.

a 2D graph-search algorithm [66] is used to segment the swollen region in the *en-face* image [i.e., the dark region inside the red circle in Fig. 7.6 (c)].

7.3.2 Computations of 3D Global, 2D Regional, and 3D Regional Retinal Features

Using the retinal layer segmentation results (and flipping the image into a right-eye orientation when necessary), the ONH volume is considered as a 3D global feature, which is defined as the volume between the ILM and the lower bounding of RPE (Section 7.2.2). For the 2D regional features, the mean peripapillary RNFL (pRNFL) and TR (pTR) thicknesses are calculated around a circular scan with a radius of 1.73 mm, which matched the same setting as Zeiss commercial machines (Section 7.2.1). Finally, the nasal, superior, temporal, and inferior regions within the swollen area

[i.e., the dark region inside the red circle, Fig. 7.6 (c)] are considered as 3D regional features. In particular, as illustrated in the red region in Fig. 7.6 (d), the nasal volume is defined as the TR volume within the nasal quadrant (315° to 45° using the geometric centroid of the swollen region). The volumes of the superior, temporal, and inferior regions are the quadrants of the total swelling regions between 45° to 135°, 135° to 225°, and 225° to 315° [i.e. the yellow, blue, green quadrants in Fig. 7.6 (d), respectively].

7.3.3 Classification of Frisén Scale Grade

A fuzzy k-nearest-neighbor (k-NN) algorithm was used to predict the Frisén scale grade associated with multiple SD-OCT features (i.e., the ONH volume, the mean pRNFL and pTR thicknesses, as well as the mean volumes of the nasal, superior, temporal, and inferior regions) and tested by a cross-validation, which means repeatedly excluding all the scans from one patient and then using the information of the other patients to predict the Frisén scales of the previously excluded scans. Further, the sequential forward searching algorithm is adopted to obtain the best possible combination of these features. The accuracy of prediction as well as the mean Frisén grade difference (MGD) of different feature combinations were computed, where MGD was defined as the absolute Frisén scale difference between the k-NN classifier's output and the agreement of three independent neuro-ophthalmologists. Thus, an MGD of zero would correspond to a perfect classification result. The k-NN algorithm was implemented using a C++ library for approximate nearest neighbor (ANN) searching [80]. Because only seven features were considered in this study (which means the computational time is relatively short), the error bound of the maximum approximation in the ANN library is set to zero in our implementation.

Table 7.2: The mean ONH volume (3D global feature), pRNFL and pTR thickness (2D regional features), and regional volumes (3D regional features) of the input 70 SD-OCT ONH scans for each Frisén scale grade in papilledema.

Frisén Scale Grade	0	1	2	3	4	
# of Eyes	5	25	28	7	5	
ONH Volume	11.18 [0.26]	12.32 [0.24]	14.30 [0.40]	16.53 [0.58]	21.45 [1.36]	(mm^3)
pRNFL Thickness	84.08 [9.50]	113.00 [5.35]	185.19 [14.95]	270.49 [34.47]	464.54 [74.10]	(μm)
pTR Thickness	309.31 [12.96]	341.48 [9.21]	418.56 [19.02]	525.68 [39.62]	805.72 [80.68]	(μm)
Nasal Volume	0.22 [0.03]	0.38 [0.03]	0.84 [0.08]	1.20 [0.13]	1.61 [0.26]	(mm^3)
Superior Volume	0.24 [0.05]	0.49 [0.05]	1.10 [0.10]	1.42 [0.13]	1.90 [0.25]	(mm^3)
Temporal Volume	0.15 [0.04]	0.25 [0.02]	0.63 [0.06]	0.92 [0.11]	1.40 [0.23]	(mm^3)
Inferior Volume	0.26 [0.05]	0.52 [0.05]	1.13 [0.10]	1.48 [0.14]	1.91 [0.24]	(mm^3)

Note: [*] represents the standard error of the mean.

7.3.4 Experimental Methods and Results

Seventy ONH-centered SD-OCT volumetric scans (Carl Zeiss Meditec, Inc., Dublin CA) from 22 papilledema patients with multiple visits were obtained from The University of Iowa. Each scan had dimensions of 200×200×1024 voxels that covered a volume 6×6×2 mm^3.

All of the corresponding fundus photographs were graded by three independent neuro-ophthalmologists from The University of Iowa, and the majority outcome, which was decided by the winner-take-all rule, was adopted when the original three judgments were not consistent. Within these 70 ONH scans, there were 5, 25, 28, 7, and 5 scans with Frisén grade of 0, 1, 2, 3, and 4, respectively. (Note: there were no scans with Frisén grade 5 in this work.)

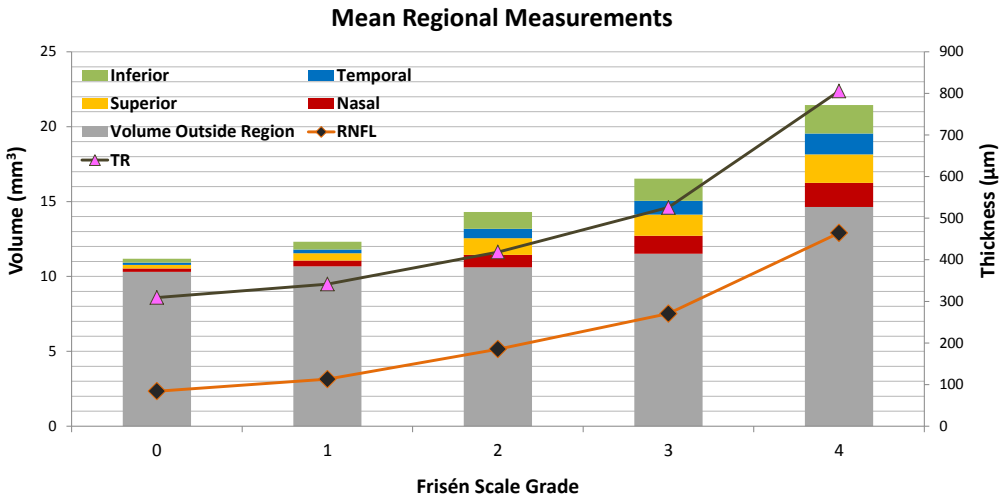

Figure 7.7: Bar chart indicating the mean values of each of the 2D and 3D features for each Frisén scale grade, where the volumetric (or thickness) measurements use the left (or right) y-scale.

The ONH volume was the only 3D global feature, and the mean ($\pm$ standard error) results from grades 0 to 4 were 11.18 ($\pm$ 0.26), 12.32 ($\pm$ 0.24), 14.30 ($\pm$ 0.40), 16.53 ($\pm$ 0.58), and 21.45 ($\pm$ 1.36) mm^3, respectively. For the 2D regional features (i.e., the pRNFL and pTR thicknesses) and the 3D regional features (i.e., the mean volumes of the nasal, superior, temporal, and inferior regions), organized results are shown in Table 7.2 and Fig. 7.7.

The Spearman rank correlation coefficients between the Frisén scale grade and the ONH volume, the mean pRNFL and pTR thicknesses, and the regional volumes of nasal, superior, temporal and inferior areas are shown in Table 7.3. Fig. 7.8 represents the mean thickness maps between ILM and RPE of each Frisén scale grade.

Using the k-NN classifier with k-value of 15, the best set of multi-feature selections is the combination of the TR thickness and the mean temporal volume, where the mean Frisén grade difference (MGD) was 0.386 and the accuracy of prediction was 64.29%. If only considering the 3-D global feature, the MGD and accuracy was just

Table 7.3: Spearman Rank Correlations between Frisén Scale Grade and 2D/3D Features.

Feature	3D Global ONH	2D Regional pRNFL	2D Regional pTR	3D Regional Nasal	3D Regional Superior	3D Regional Temporal	3D Regional Inferior
Spearman Correlation	0.737	0.739	0.673	0.752	0.747	0.770	0.758
	all p-values < 0.001						

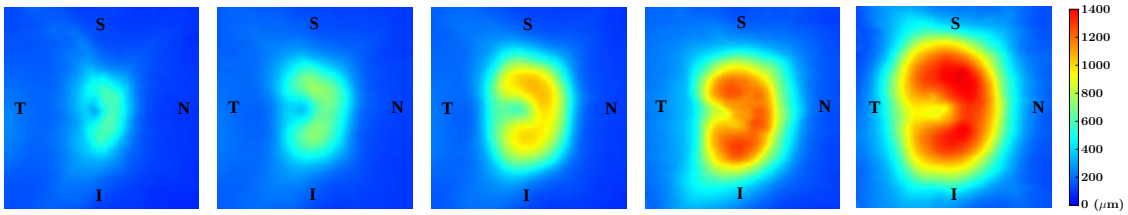

(a) (b) (c) (d) (e)

Figure 7.8: Mean thickness maps between the ILM and RPE in papilledema from Frisén scale grade 0 (a) to 4 (e), where labels 'N', 'S', 'T' and 'I' represent 'Nasal', 'Superior', 'Temporal' and 'Inferior', respectively.

0.629 and 41.43%, respectively. Fig. 7.9 is a performance-related comparison among features, where the dark purple represents the best feature combination (i.e. the mean pTR thickness and the temporal volume).

7.3.5 Conclusions

Although the Frisén scale grading system has been a popular and standard assessment for papilledema, the high subjectivity, low reproducibility, and the requirement of specific expertise are still unavoidable. The recent introduction of SD-OCT gives a great alternative for ophthalmologists to analyze 3D volumetric information of papilledema. Although the preliminary results have been recently presented showing high correlation between total retinal (TR) volume in SD-OCT and Frisén scale grades (Section 7.2, [7]), the work in this section reflects the first time that region-based met-

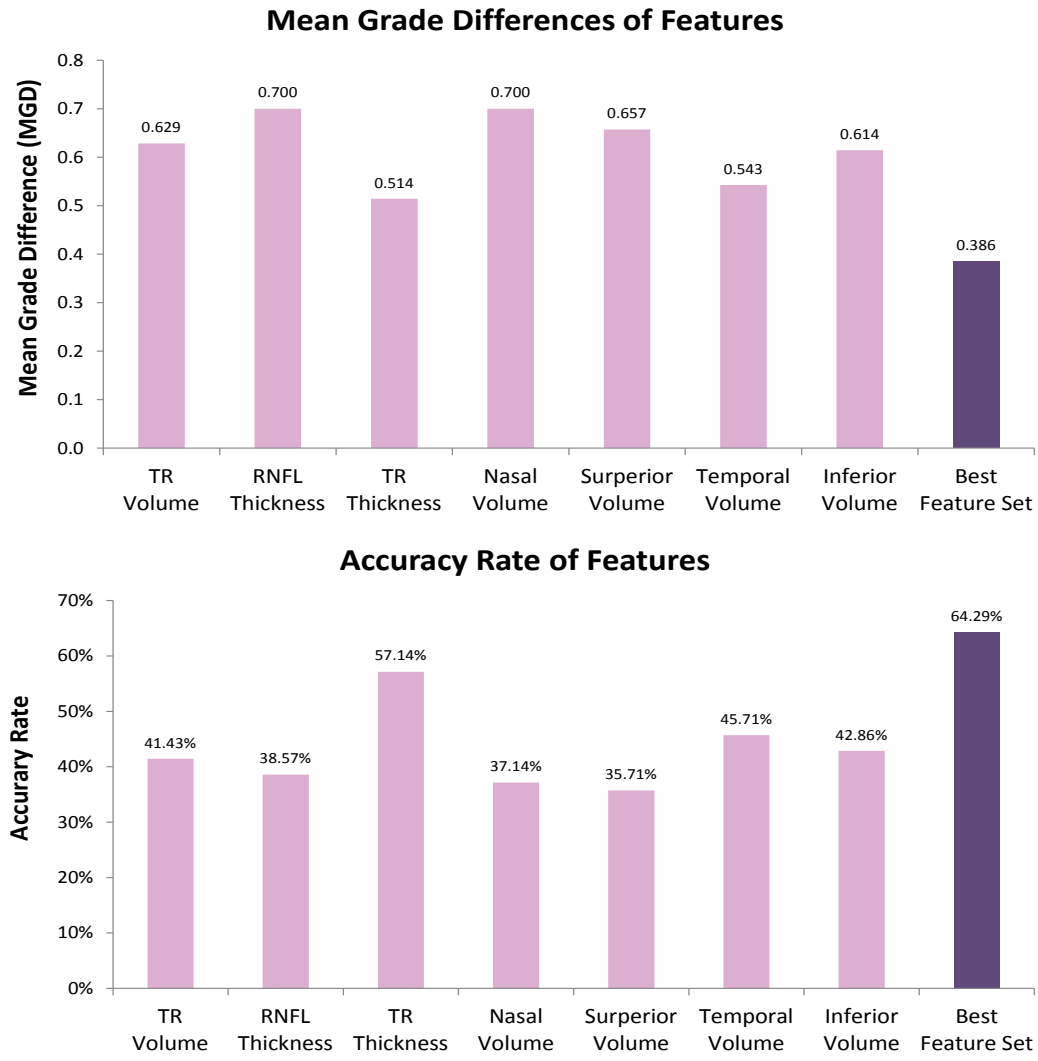

Figure 7.9: A performance-related comparison of the single-feature results and the best combination of the selected features, where the best feature set was the combination the mean pTR thickness and the temporal volume.

rics are examined for assessing papilledema. The changing of the "flipped C-shape" at the optic disc in Fig. 7.8 is strong evidence demonstrating that regional features play a very important role in differentiating the different grades of papilledema. Also, the region-based volumetric estimation had a higher Spearman rank correlation than the results from using the ONH volumetric estimation alone.

In addition, this is the first study for the Frisén scale grades that are predicted using a fuzzy k-NN classifier with the combination of global as well as regional features from the automated SD-OCT layer segmentations. Using sequential forward searching algorithm found the best multiple-feature set, which was the combination of the mean pTR thickness and the mean temporal volume. With the leave-one-subject-out cross validation, the fuzzy k-NN classifier with the best multiple-feature set reduced the mean Frisén grade difference down to 0.386 with the accuracy 64.29%. This was a significant improvement compared to only considering the ONH volume to predict Frisén scale grade which had an MGD of 0.629 and accuracy of 41.43%. In future work, it will be important to perform similar experiments on a larger dataset of subjects as this dataset is biased to contain a high proportion of Frisén scale grades 1 and 2. Thus, the selected features may be correspondingly biased to perform best on those grades. Nevertheless, at minimum, this work demonstrates the importance of considering region-based features in further studies.

7.4 Continuous-Scale Papilledema Severity Score Estimation

Since only a small dataset (including 22 papilledema subjects from the University of Iowa) was used in the previous section, the much larger dataset from the IIHTT OCT sub-study (including 126 papilledema subjects due to idiopathic intracranial hypertension (IIH) [11, 12, 18, 19, 68]) is used in this work to test the proposed idea of using a machine-learning technique to mimic experts' decisions of assessing papilledema severity. In addition to increasing the size of the input dataset, a few

modifications have also been added to this section. First, instead of using a fuzzy k-NN classifier, random forest classifiers are utilized to internally select the best input feature combination to achieve better prediction results. Second, the definitions of the region-based volumetric OCT features are slightly adjusted to better fit clinical meaning. Third, the peripapillary retinal pigment epithelium and/or Bruch's membrane (pRPE/BM) 2D and 3D shape measures are added to the learning system. Although it has been known that the pRPE/BM shape change may reflect the intrcacranial pressure change [13, 14], there is still no study that has addressed the comparisons between the pRPE/BM shape measure and Frisén grade.

7.4.1 Classification of Frisén Scale Grades

In IIHTT, Frisén grades (scale 0: normal; scale 5: severe) of papilledema are determined 1) by neuro-ophthalmologists in the photographic reading center (PRC) based on digital photographs evaluation, and 2) by the principal investigators at each site during the clinical examination (CE). In this study, the CE Frisén grade is considered as the reference standard, because we believe that the site investigators may have more available information than the clinicians in the reading center, who only have the assess to the fundus images.

7.4.2 Retinal Features Using Optical Coherence Tomography

Ten OCT features are used as the inputs of the machine learning system. The first three are the total ONH volume as well as peripapillary RNFL and TR thicknesses, which can be computed using the methods described in Section 7.2. Next, four region-based volumetric features are computed. The region boundary has been changed from using the detected swollen region (Section 7.3) to directly using the peripapillary circle (radius = 1.73 mm). As illustrated as the red region in Fig. 7.10, the nasal volume is defined as the ONH volume within the nasal quadrant (315° to 45° using

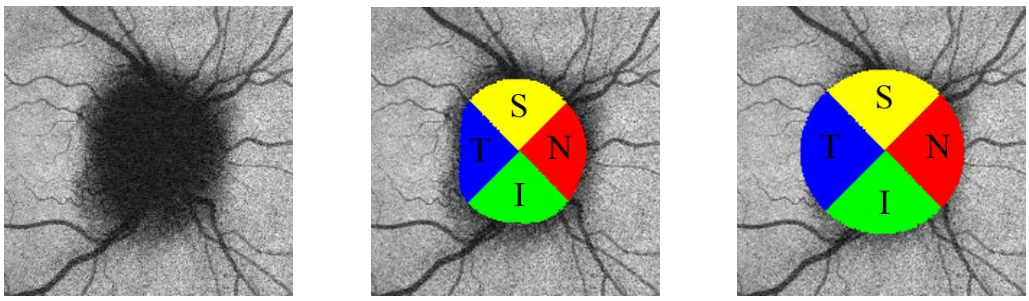

(a) (b) (c)

Figure 7.10: Region-based volumetric features. (a) Original RPE *en-face* image. (b) Region-based volumetric features in the swollen region, which is defined in Section 7.3.2. (c) Region-based volumetric features in the peripapillary region, where the radius is 1.73 mm.

the geometric centroid of the swollen region). The volumes of the superior, temporal, inferior regions are the quadrants of the total swelling regions between 45° to 135°, 135° to 225°, 225° to 315° [i.e. the yellow, blue, green quadrants in Fig. 7.10 (b, c), respectively]. The eighth feature is the volumetric summation of these four quadrants, called the peripapillary region volume. The last two features are the pRPE/BM 2D and 3D shape measures, which can be computed using the same methods as we discussed in Section 6.2 and 6.3, respectively.

7.4.3 Estimation and Validation of Papilledema Severity Score

Random forest classifiers are used to estimate the papilledema severity score (PSS) with the OCT input features that were discussed in the previous section: the total ONH volume, the peripapillary RNFL and TRT thicknesses, the volumes of the nasal, superior, temporal and inferior regions, the total peripapillary volume, and the pRPE/BM 2D as well as 3D shape measures. The random forest algorithm is implemented using R language with the classification and regression training (i.e., CARET) package [81]. The cross-validation method is implemented with the CARET package to automatically decide the best number of variables randomly sampled as candidates

at each split in these trees considering the lowest out-of-bag (OOB) error [81]. For the purpose of the severity score validation, the root-mean-square deviation (RMSD) and consistency rate between the predicted papilledema severity score and both PRC and CE Frisén grades are computed. Here, the RMSD is defined as the square root of the mean square residuals between the regression outputs of the random forest algorithm and the corresponding Frisén grades, and the consistency rate is defined as the percentage of the subjects whose rounded predicted PSS is the same as the corresponding Frisén grade.

7.4.4 Experimental Methods and Results

One-hundred and twenty-six papilledema subjects (due to idiopathic intracranial hypertension), right eyes at baseline, from the IIHTT dataset were initially included in this study. To compare the Frisén grades with the OCT features, eleven subjects were excluded because their OCT features were not available due to either missing images or bad image quality. Therefore, there were 115 right eyes included with their photographic reading center (PRC) and clinical examination (CE) Frisén grades and all of the ten OCT features. Next, these 115 right eyes were randomly split into a training set (80 eyes) and a testing set (35 eyes). In the training set, the counts for the CE (PRC) Frisén grade 0 to 5 were 1 (0), 18 (10), 23 (31), 23 (23), 11 (12), and 4 (4), respectively. The root-mean-square deviation (RMSD) between these two Frisén grades was 0.82, and the consistency rate was 0.48. Next, a regression model was trained by a random forest algorithm with 1000 randomly generated decision trees using the OCT features from the training set. The implementation was achieved using the CARET package in R language. The random forest classifiers considered the CE Frisén grade as the reference standard and utilized ten-fold cross-validation to decide the best amount of the variables to split on each node in these decision trees with the lowest out-of-bag (OOB) error. Meanwhile, the importance of each feature was computed and is shown in Fig. 7.11.

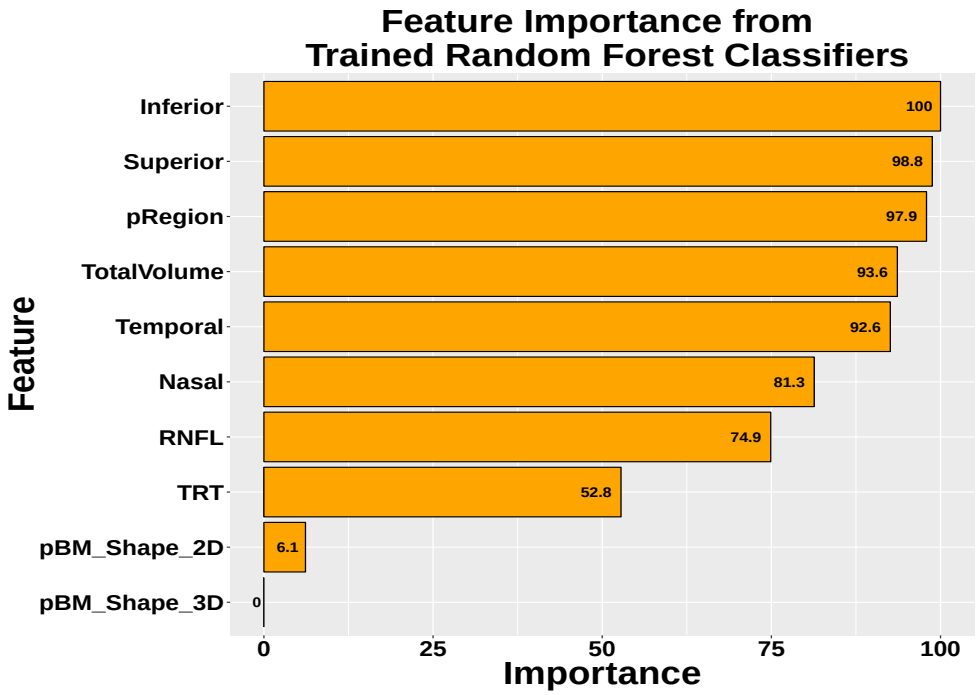

Figure 7.11: A bar chart of the feature importance from the random forest algorithm (scale from 0.0 to 100.0), where "TotalVolume" represents the total ONH volume, "Nasal", "Superior", "Temporal" and "Inferior" represents the four individual 90° quadrant volumes of the peripapillary region, "pRegion" represent the total volume of the peripapillary region, "RNFL" and "TRT" separately represents the peripapillary RNFL and TR thicknesses, and "pBM_Shape_2D" as well as "pBM_Shape_3D" represents the pRPE/BM 2D as well as 3D shape measure, respectively.

Table 7.4: The comparisons among the photographic reading center Frisén grades (PRCG), clinical examination Frisén grades (CEG), and papilledema severity score (PSS) in both training and testing sets.

		PRCG vs. CEG	PSS vs. CEG
Training Set (80 Eyes)	RMSD[a]	0.82	X
	Consistency Rate	0.48	X
Testing Set (35 Eyes)	RMSD	0.97	0.70
	Consistency Rate	0.31	0.49[b]

[a] Root-mean-square deviation
[b] PSS is rounded-off before the computation

On the other hand, in the testing set (35 eyes), the counts for the CE (PRC) Frisén grades from 0 to 5 were 1 (0), 5 (5), 12 (10), 11 (10), 6 (10), and 0 (0), respectively. The RMSD between these two Frisén grades was 0.97, and the consistency rate was 0.31. Fig. 7.12 (a, b) shows the confusion matrices of the training and testing dataset, respectively; note that there was no grade 5 in the testing set. After applying the testing set to the trained random forest model, the regression results, called papilledema severity scores (PSS), were computed. The RMSD between the PSS and clinical examination (CE) Frisén grades in the testing set was 0.70, which is significantly smaller than the RMSD between the PRC and CE Frisén grades in the testing set ($p < 0.05$). Fig. 7.13 (a) shows the histogram of the predicted PSS with a bin width of 0.5; Fig. 7.13 (b) shows the confusion matrix of the rounded PSS and CE Frisén grades, where the consistency rate was 0.49. Table 7.4 shows the comparisons among the PRC Frisén grade, CE Frisén grade and PSS in both training and testing sets.

In addition, considering both of the training and testing sets (i.e., 80 + 35 eyes), the Spearman rank correlations between the CE Frisén grade and the 10 OCT features were also calculated (Fig. 7.14).

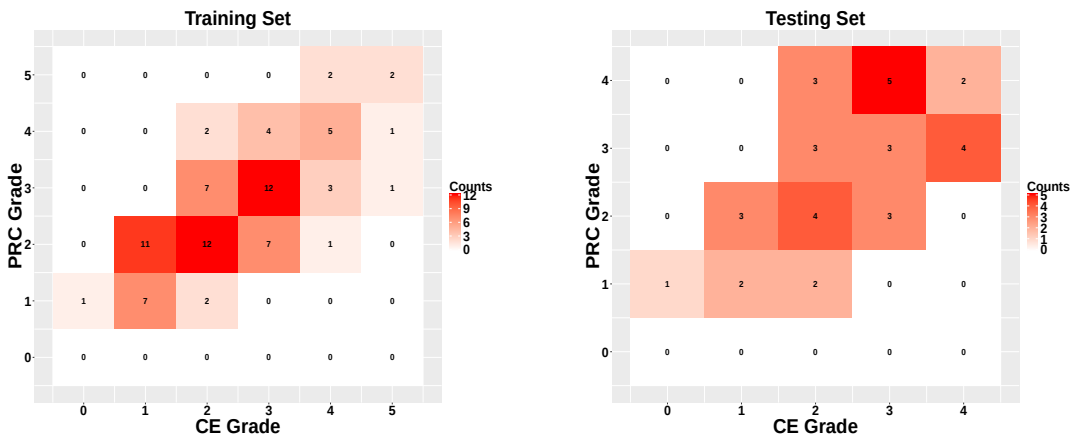

(a) (b)

Figure 7.12: Confusion matrix between the photographic reading center (PRC) and clinical examination (CE) Frisén grades in (a) the training set of 80 eyes, where the RMSD was 0.82 as well as consistency rate was 0.48, and (b) the testing set of 35 eyes, where the RMSD was 0.97 as well as consistency rate was 0.31. Note: there is no grade 5 in the testing set.

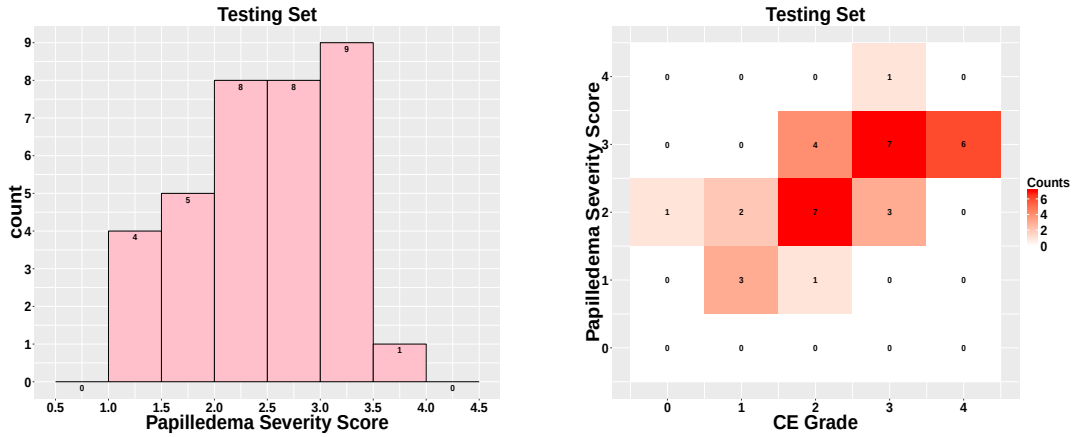

(a) (b)

Figure 7.13: Predicted papilledema severity scores (PSS) in the testing set of 35 eyes. (a) The histogram of the PSS with the bin width of 0.5. (b) The confusion matrix between the rounded PSS and CE Frisén grade, where the consistency rate was 0.49.

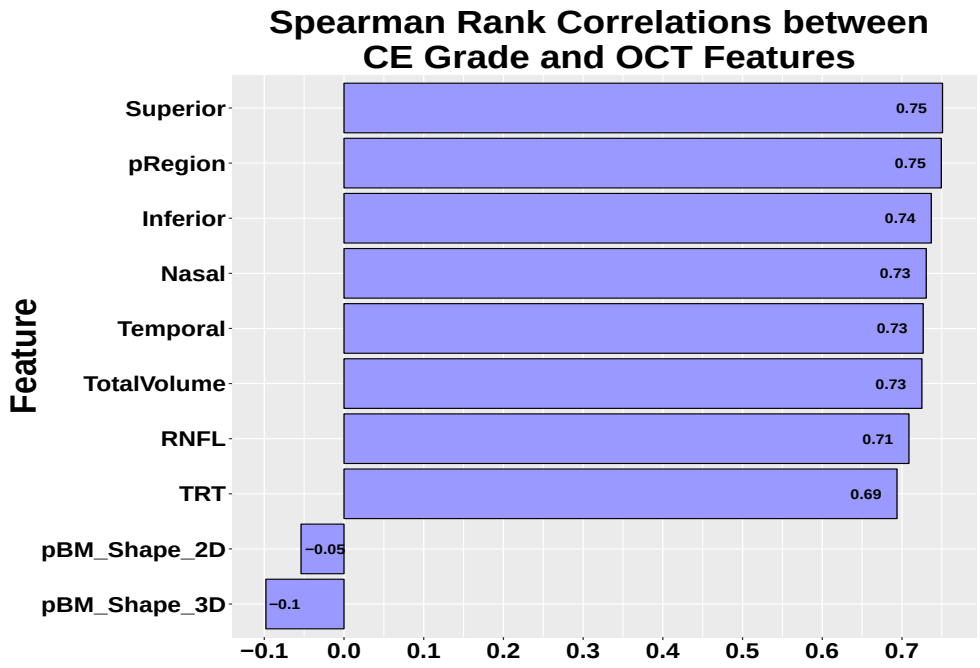

Figure 7.14: A bar chart of the Spearman rank correlation coefficients between the CE Frisén grade and the OCT features, where "TotalVolume" represents the total ONH volume, "Nasal", "Superior", "Temporal" and "Inferior" represents the four individual 90° quadrant volumes of the peripapillary region, "pRegion" represent the total volume of the peripapillary region, "RNFL" and "TRT" separately represents the peripapillary RNFL and TR thicknesses, and "pBM_Shape_2D" as well as "pBM_Shape_3D" represents the pRPE/BM 2D as well as 3D shape measure, respectively.

7.4.5 Conclusions

Fig. 7.14 demonstrates that the total ONH volume, the peripapillary RNFL and TR thicknesses, and the region-based volumetric measurements are strongly correlated to the Frisén grades in the IIHTT dataset, which is consistent with the conclusions from previous studies [7, 68, 72]. It is also not surprising to see that the pRPE/BM 2D and 3D shape measures have very limited correlations with the Frisén grades, since these pRPE/BM shape measures mostly represent the papilledema severity from the perspective of the changes in intracranial pressure [13, 14, 76]. (On the other hand, the Frisén grades are determined by the visible features of the peripapillary retina and the optic disc from the fundus photographs or direct funduscopic observation.) In addition, comparing Fig. 7.11 with Fig. 7.14, we find the feature importance from the random forest framework has a very similar patten to the Spearman rank correlations between the CE Frisén grade (i.e., the reference standard) and the OCT features. This adds to the explanation for why the pRPE/BM shape measures do not help the machine-learning algorithm to determine the Frisén grades.

In fact, although the data here has shown that the pRPE/BM shape measures do not directly contribute to the prediction of a Frisén-scale-based papilledema severity score, the pRPE/BM shape measures practically support evidence to help distinguish the causes of optic disc edema, such as pseudo-papilledema, ischemic optic neuropathy, and meningiomas of the optical nerve sheath [14, 15]. Since papilledema is defined by optic disc swelling due to elevated intracranial pressure, the pRPE/BM shape measures can be extremely helpful for the proposed machine-learning system to distinguish papilledema from the other types of optic disc swelling with an appropriate reference standard.

Based on Fig. 7.12, it is noticeable that the CE and PRC Frisén grades are not generally consistent (the consistency rate in training and testing sets are only 0.48 and 0.31, respectively). This is in agreement with the other studies showing that

the Frisén grading system has the limitation of high intra-observer variability [4–7]. Therefore, developing a more robust system to consistently evaluate papilledema is truly beneficial for the clinical needs. With a robust OCT layer-segmentation algorithms, the OCT features can be computed automatically and quantitatively. Then, the proposed machine-learning framework can be directly applied to these OCT measurements to output a severity score. Our data shows that the proposed papilledema severity score (PSS) was significantly closer to the reference standard than the Frisén grades that were determined by the photographic reading center. Because the expertise of accurately determining the severity of papilledema is unique, this machine-learning system can be potentially useful for helping clinicians who are under training to practice their judgments. Or, for some other situations, such as circumstances in which qualified clinicians are not immediately available (for example, emergency departments), technicians trained in operating OCT devices may use this proposed system to obtain a preliminary assessment without invasive exams. The proposed PSS system can be potentially useful in multiple clinical scenarios.

CHAPTER 8
CONCLUSIONS

Due to the low requirements of the imaging technique, the Frisén grade system has been a standard measurement of papilledema since its introduction in 1982. Because the Frisén grades are determined by experts qualitatively examining the visual features of the peripapillary retina and the optic disc from the fundus photographs or direct funduscopic observation, this grading system has inherent limitations (such as high intra- and inter-observer variability, need of specific expertise, tedious processing steps, and the ordinal nature of the scale), resulting in low reproducibility. Spectral-domain optical coherence tomography (SD-OCT), on the other hand, is a relatively new imaging technique and has an entirely different perspective of assessing the retinal tissue. SD-OCT has the ability to enable cross-sectional information of the retina to be acquired without invasive procedures; this type of advantage makes the OCT technique very popular in the fields of ophthalmology and neuro-ophthalmology.

To obtain accurate retinal measurements using the OCT images, the accuracy of the retinal layer segmentation plays an important role. Although most of the commercial OCT devices support automated retinal layer segmentation with regular measurements (such as the peripapillary RNFL and TR thicknesses), there is still no particular commercial device that has the ability to reliably perform the layer segmentation in severely swollen optic discs. Therefore, in Chapter 4, details were discussed about developing robust retinal layer segmentation algorithms for optic disc swelling in an automated fashion. These proposed algorithms work for both high-definition five-line raster (HD-5LR) and regular volumetric protocols. Based on accurate segmentation results, OCT parameters (such as the peripapillary RNFL and TR thicknesses, the volumes of the total ONH as well as peripapillary region, and the volumes of the peripapillary nasal, superior, temporal, and inferior quadrants) are also reliable. For example, in the Idiopathic Intracranial Hypertension Treatment

Trial (IIHTT) OCT sub-study baseline dataset, including 126 subjects, the proposed layer segmentation algorithms have been demonstrated to be less prone to failure in segmenting retinal layers under swollen optic discs compared to the accompanied algorithms of the commercial SD-OCT devices [11]. Chapter 4 provides a solid foundation to compute the OCT measurements in this doctoral work.

In addition to the volumetric and thickness measurements, multiple studies have also shown that the peripapillary retinal pigment epithelium and/or Bruch's membrane (pRPE/BM) deformation may reflect a change in intracranial pressure. Therefore, quantifying the pRPE/BM shape variation becomes another currently widespread topic in the field of investigating papilledema. To correctly evaluate the pRPE/BM shape, the accurate location of the pRPE/BM opening needs to be segmented beforehand. Chapter 5 thoroughly addressed this topic, from the difficulties of segmenting the pRPE/BM opening under severely swollen retinal tissue in SD-OCT images, to further providing semi- and fully automated methods to perform the pRPE/BM profile segmentation in the SD-OCT RPE *en-face* image domain. Then, Chapter 6 extended the obtained BMO contour and automatically placed landmarks, for the purpose of generating 2D and 3D pRPE/BM shape models. The traditional method (which is completely manual) of generating the pRPE/BM shape model was limited by its tediousness so that it was applicable only in 2D and for relatively small datasets. Chapter 5 and Chapter 6 improved the traditional method by automating it and successfully applied the computed 2D and 3D pRPE/BM shape measures for a large-scale dataset (i.e., IIHTT dataset). Having these two chapters is important, because this is the first study of automating the processes of generating statistical-shape models of the retinal layer, especially the methods working for both swollen and normal optic discs. However, since the optic disc swelling does not immediately subside when the intracranial pressure dramatically decreases (e.g. after shunt, lumbar puncture, or other aggressive procedures), the pRPE/BM shape measures may temporarily show

inconsistency with the other OCT volumetric or thickness measurements to reflect the papilledema severity. Generally speaking, the optic disc swelling may lag over the ensuring days to weeks [15].

Potential future work using the pRPE/BM shape models is to develop a system to use the pRPE/BM shape measures to be an alternative to reflect the true cerebrospinal fluid (CSF) pressure, so patients could reduce the need of receiving lumbar punctures. Also, because the pRPE/BM shape change reflects the change in the intracranial pressure, it is beneficial to use these shape measures to test if the optic disc swelling is papilledema. Since the Bruch's membrane opening is often obscure under a severely swollen inner retina in the OCT images, the true location may come clearer when the swelling subsides over time. Therefore, another potential extension of the pRPE/BM segmentation and shape models is to use the latter results in the longitudinal dataset to cross-validate the baseline results. In addition, using the results from the previous couple visits may be helpful in predicting papilledema development or treatment progress. Another application is to extend this methodology to model different retinal layers and/or the layer combinations for the purposes of classifying the types of optic disc swelling. The shapes of optic disc swelling may show dissimilarly at different retinal layers from various etiologic and pathogenetic mechanisms.

Due to the low reproducibility of Frisén grading system, neuro-ophthalmologists have been researching alternative methods on a continuous scale to present the papilledema severity more objectively. SD-OCT is relatively new and capable of quantifying retinal structure. Not surprisingly, researchers have started to investigate the possibility of using SD-OCT measurements as features to develop a quantitative system to replace the current qualitative method. Chapter 7, first, demonstrated that the total ONH volumes are strongly correlated with Frisén grades to show the potential usage of this 3D SD-OCT feature as new option to assess papilledema. This step is important, because the 2D thickness measurements (i.e., the peripapillary RNFL and

TR thicknesses) become less reliable when the optic disc swelling is severe [12]. Then, the SD-OCT volumetric region-based features were tested in a machine-learning system in a small dataset to indicate that using multiple SD-OCT features together may increase the accuracy of mimicking experts' decisions of assessing papilledema from fundus images. By observing Fig. 7.8, the inverse "C-shape" swelling clearly shows papilledema development by region in order of severity. Finally, a random forest algorithm was utilized to consider all the available SD-OCT features to compute the papilledema severity score (PSS) to objectively reflect the degree of the optic disc swelling due to raised intracranial pressure. So far, this machine-learning system was trained by utilizing Frisén grades as the reference standard. Since the Frisén grades and SD-OCT features may reflect different pathophysiological aspects of papilledema, the proposed machine-learning framework also keeps the flexibility of switching the learning targets as well as adding/removing extra features. For example, it is possible to switch the current reference standard to the experts' severity rankings. By doing so, the scales of the original Frisén grading system can be dramatically extended. Also, a recent study showed that multiple types and patterns of folds in papilledema, which express stress and strain, appear to be a function of two separate but interrelated biomechanical drivers: volumetric expansion of the optic nerve head and anterior deformation of the pRPE/BM [82]. Therefore, a possible extension of this system is to quantify these retinal folds and then use them as new features. Also, as we discussed in the previous section, measures of different retinal layers can be potentially good features as well. Considering all these new and proposed features together, the generalization of the proposed PSS system can be improved.

To summarize, this doctoral work develops a machine-learning system using 2D/3D SD-OCT images to evaluate papilledema severity based on global and regional features, including volumes and thicknesses, as well as shape measures. It is expected to be a more robust system than the traditional qualitative method (i.e., the Frisén

grading system). The current limitation of this work is that the Frisén grades are still the reference standard for the proposed system, so the learning system may be biased by the high variability in the ground truth. However, the advantage of this doctoral work is that the proposed machine-learning framework is flexible, so the input features and learning targets can be straightforwardly adjusted without much modification to fit new applications. Future works may include increasing the generalization of the proposed PSS system and switching to different reference standards for the machine-learning system to distinguish the types of the optic disc edema.

REFERENCES

[1] M. Rigi, S. J. Almarzouqi, M. L. Morgan, and A. G. Lee, "Papilledema: epidemiology, etiology, and clinical management," *Eye and Brain*, vol. 7, pp. 47–57, 2015.

[2] S. S. Hayreh, "Pathogenesis of optic disc edema in raised intracranial pressure," *Prog. Retin. Eye Res.*, vol. 50, pp. 108–144, 2016.

[3] L. Frisén, "Swelling of the optic nerve head: a staging scheme," *J Neurol Neurosurg Psychiatry*, vol. 45, pp. 13–18, 1982.

[4] C. J. Scott, R. H. Kardon, A. G. Lee, L. Frisén, and M. Wall, "Diagnosis and grading of papilledema in patients with raised intracranial pressure using optical coherence tomography vs clinical expert assessment using a clinical staging scale," *Arch Ophthalmol*, vol. 128, no. 6, pp. 705–711, 2010.

[5] S. Echegaray, G. Zamora, H. Yu, W. Luo, P. Soliz, and R. Kardon, "Automated analysis of optic nerve images for detection and staging of papilledema," *Invest Ophthalmol Vis Sci*, vol. 52, pp. 7470–7478, 2011.

[6] A. J. Sinclair, M. A. Burdon, P. G. Nightingale, T. D. Matthews, A. Jacks, M. Lawden, A. Sivaguru, B. J. Gaskin, S. Rauz, C. E. Clarke, and A. K. Ball, "Rating papilloedema: an evaluation of the Frisén classification in idiopathic intracranial hypertension," *J Neurol*, vol. 259, pp. 1406–1412, 2012.

[7] J.-K. Wang, R. H. Kardon, M. J. Kupersmith, and M. K. Garvin, "Automated quantification of volumetric optic disc swelling in papilledema using spectral-domain optical coherence tomography," *Invest Ophthalmol Vis Sci*, vol. 53, no. 7, pp. 4069–4075, 2012.

[8] D. Huang, E. A. Swanson, C. P. Lin, J. S. Schuman, W. G. Stinson, W. Chang, M. R. Hee, T. Flotte, K. Gregory, and C. A. Puliafito, "Optical coherence tomography," *Science*, vol. 254, no. 5035, pp. 1178–1181, Nov. 1991.

[9] E. Z. Karam and T. R. Hedges, "Optical coherence tomography of the retinal nerve fibre layer in mild papilloedema and pseudopapilloedema," *Br J Ophthalmol*, vol. 89, no. 3, pp. 294–298, 2005.

[10] G. Savini, C. Bellusci, M. Carbonelli, M. Zanini, V. Carelli, and P. B. Alfredo A. Sadun, "Detection and quantification of retinal nerve fiber layer thickness in optic disc edema using stratus OCT," *Arch Ophthalmol*, vol. 124, pp. 1111–1117, 2006.

[11] OCT Sub-Study Committee for the NORDIC Idiopathic Intracranial Hypertension Study Group, "Baseline OCT measurements in the Idiopathic Intracranial Hypertension Treatment Trial, Part I: Quality control, comparisons, and variability," *Invest Ophthalmol Vis Sci*, vol. 55, pp. 8180–8188, 2014.

[12] Optical Coherence Tomography Substudy Committee; NORDIC Idiopathic Intracranial Hypertension Study Group, "Papilledema outcomes from the optical coherence tomography substudy of the Idiopathic Intracranial Hypertension Treatment Trial," *Ophthalmology*, vol. 122, no. 9, pp. 1939–1945, 2015.

[13] M. J. Kupersmith, P. Sibony, G. Mandel, M. Durbin, and R. H. Kardon, "Optical coherence tomography of the swollen optic nerve head: Deformation of the peripapillary retinal pigment epithelium layer in papilledema," *Invest Ophthalmol Vis Sci*, vol. 52, no. 9, pp. 6558–6564, 2011.

[14] P. Sibony, M. J. Kupersmith, and F. J. Rohlf, "Shape analysis of the peripapillary RPE layer in papilledema and ischemic optic neuropathy," *Invest Ophthalmol Vis Sci*, vol. 52, no. 11, pp. 7987–7995, 2011.

[15] P. Sibony, M. J. Kupersmith, R. Honkanen, F. J. Rohlf, and A. Torab-Parhiz, "Effects of lowering cerebrospinal fluid pressure on the shape of the peripapillary retina in intracranial hypertension," *Invest Ophthalmol Vis Sci*, vol. 55, no. 12, pp. 8223–8231, 2014.

[16] K. Li, X. Wu, D. Z. Chen, and M. Sonka, "Optimal surface segmentation in volumetric images – a graph-theoretic approach," *IEEE Trans Pattern Anal Machine Intell*, vol. 28, no. 1, pp. 119–134, 2006.

[17] S. S. Hayreh, "Optic disc edema in raised intracranial pressure. VI. Associated visual disturbances and their pathogenesis," *Arch Ophthalmol.*, vol. 95, pp. 1566–1579, 1977.

[18] D. I. Friedman, M. P. McDermott, K. Kieburtz, M. J. Kupersmith, A. Stoutenburg, J. L. Keltner, S. E. Feldon, E. Schron, J. J. Corbett, M. Wall, and for the NORDIC IIHTT Study Group, "The Idiopathic Intracranial Hypertension Treatment Trial: Design considerations and methods," *J Neuroophthalmol*, vol. 34, no. 2, pp. 107–117, 2014.

[19] M. Wall, M. J. Kupersmith, K. D. Kieburtz, J. J. Corbett, S. E. Feldon, D. I. Friedman, D. M. Katz, J. L. Keltner, E. B. Schron, M. P. McDermott, and the NORDIC Idiopathic Intracranial Hypertension Study Group, "The Idiopathic Intracranial Hypertension Treatment Trial: Clinical profile at baseline," *JAMA Neurol.*, vol. 71, no. 6, pp. 693–701, 2014.

[20] K. A. Markey, S. P. Mollan, R. H. Jensen, and A. J. Sinclair, "Understanding idiopathic intracranial hypertension: mechanisms, management, and future directions," *Lancet Neurol*, vol. 15, pp. 78–91, 2016.

[21] L. T. Lai, H. V. Danesh-Meyer, and A. H. Kaye, "Visual outcomes and headache following interventions for idiopathic intracranial hypertension," *J. Clin. Neurosci.*, vol. 21, pp. 1670–1678, 2014.

[22] L. Tang, R. H. Kardon, J.-K. Wang, M. K. Garvin, K. Lee, and M. D. Abràmoff, "Quantitative evaluation of papilldema from stereoscopic color fundus photographs," *Invest Ophthalmol Vis Sci*, vol. 53, no. 8, pp. 4490–4497, 1911.

[23] M. Wojtkowski, R. Leitgeb, A. Kowalczyk, T. Bajraszewski, and A. F. Fercher, "In vivo human retinal imaging by Fourier domain optical coherence tomography," *J Biomed Opt*, vol. 7, no. 3, pp. 457–463, Jul. 2002.

[24] M. Wojtkowski, T. Bajraszewski, I. Gorczyńska, P. Targowski, A. Kowalczyk, W. Wasilewski, and C. Radzewicz, "Ophthalmic imaging by spectral optical coherence tomography," *American Journal of Ophthalmology*, vol. 138, pp. 412–419, 2004.

[25] M. Wojtkowski, V. Srinivasan, J. G. Fujimoto, T. Ko, J. S. Schuman, A. Kowalczyk, and J. S. Duker, "Three-dimensional retinal imaging with high-speed ultrahigh-resolution optical coherence tomography," *Ophthalmology*, vol. 112, no. 10, pp. 1734–1746, Oct. 2005.

[26] M. J. Kupersmith, P. Sibony, G. Mandel, M. Durbin, and R. H. Kardon, "Optical coherence tomography of the swollen optic nerve head: Deformation of the peripapillary retinal pigment epithelium layer in papilledema," *Invest Ophthalmol Vis Sci*, vol. 52, no. 9, pp. 6558–6564, 2011.

[27] Z. Yaqoob, J. Wu, and C. Yang, "Spectral domain optical coherence tomography: a better oct imaging strategy," *BioTechniques*, vol. 39, no. 6, pp. S6–13, 2015.

[28] A. F. Fercher, C. K. Hitzenbergera, G. Kampa, and S. Y. El-Zaiatb, "Measurement of intraocular distances by backscattering spectral interferometry," *Optics Communications*, vol. 117, pp. 43–48, 1995.

[29] A. F. Fercher, W. Drexler, C. K. Hitzenberger, and T. Lasser, "Optical coherence tomography—principles and applications," *Rep. Prog. Phys.*, vol. 66, pp. 239–303, 2003.

[30] B. Cense, N. Nassif, T. Chen, M. Pierce, S.-H. Yun, B. Park, B. Bouma, G. Tearney, and J. de Boer, "Ultrahigh-resolution high-speed retinal imaging using spectral-domain optical coherence tomography," *Optics Express*, vol. 12, pp. 2435–2447, 2004.

[31] D. C. DeBuc, "A review of algorithms for segmentation of retinal image data using optical coherence tomography," in *Image Segmentation*, P.-G. Ho, Ed. InTech, 2011.

[32] J. M. Schmitt, S. H. Xiang, and K. M. Yung, "Speckle in optical coherence tomography," *J. Biomed. Opt.*, vol. 4, pp. 95–105, 1999.

[33] M. Szkulmowski, I. Gorczynska, D. Szlag, M. Sylwestrzak, A. Kowalczyk, and M. Wojtkowski, "Efficient reduction of speckle noise in optical coherence tomography," *Optics Express*, vol. 20, no. 2, pp. 1337–1359, 2012.

[34] J.-K. Wang, R. H. Kardon, and M. K. Garvin, "Combined use of high-definition and volumetric optical coherence tomography for the segmentation of neural canal opening in cases of optic nerve edema," in *Proc. SPIE 9413, Medical Imaging 2015: Image Processing*, 2015, pp. 94 133V_1–94 133V_9.

[35] S. Ricco, M. Chen, H. Ishikawa, G. Wollstein, and J. Schuman, "Correcting motion artifacts in retinal spectral domain optical coherence tomography via image registration," in *MICCAI*, vol. 5761/2009. Springer, 2009, pp. 100–107.

[36] B. Antony, M. D. Abrmoff, L. Tang, W. D. Ramdas, J. R. Vingerling, N. M. Jansonius, K. Lee, Y. H. Kwon, M. Sonka, and M. K. Garvin, "Automated 3-D method for the correction of axial artifacts in spectral-domain optical coherence tomography images," *Biomedical Optics Express*, vol. 2, no. 8, pp. 2403–2416, 2011.

[37] M. R. Hee, J. A. Izatt, E. A. Swanson, D. Huang, J. S. Schuman, C. P. Lin, C. A. Puliafito, and J. G. Fujimoto, "Optical coherence tomography of the human retina," *Arch Ophthalmol*, vol. 113, pp. 325–332, 1995.

[38] D. Koozekanani, K. Boyer, and C. Roberts, "Retinal thickness measurements from optical coherence tomography using a markov boundary model," *IEEE Trans Med Imag*, vol. 20, no. 9, pp. 900–916, 2001.

[39] M. Shahidi, Z. Wang, and R. Zelkha, "Quantitative thickness measurement of retinal layers imaged by optical coherence tomography," *Am J Ophthalmol*, vol. 139, no. 6, pp. 1056–1061, Jun. 2005.

[40] H. Ishikawa, D. M. Stein, G. Wollstein, S. Beaton, J. G. Fujimoto, and J. S. Schuman, "Macular segmentation with optical coherence tomography," *Invest Ophthalmol Vis Sci*, vol. 46, no. 6, pp. 2012–2017, Jun. 2005.

[41] A. Chan, J. S. Duker, H. Ishikawa, T. H. Ko, J. S. Schuman, and J. G. Fujimoto, "Quantification of photoreceptor layer thickness in normal eyes using optical coherence tomography." *Retina*, vol. 26, no. 6, pp. 655–660, 2006.

[42] M. Baroni, P. Fortunato, and A. L. Torre, "Towards quantitative analysis of retinal features in optical coherence tomography," *Med Eng Phys*, vol. 29, no. 4, pp. 432–441, May 2007.

[43] D. Cabrera Fernández, H. M. Salinas, and C. A. Puliafito, "Automated detection of retinal layer structures on optical coherence tomography images," *Opt Express*, vol. 13, no. 25, pp. 10 200–10 216, 2005.

[44] O. Tan, G. Li, A. T.-H. Lu, R. Varma, D. Huang, and Advanced Imaging for Glaucoma Study Group, "Mapping of macular substructures with optical coherence tomography for glaucoma diagnosis," *Ophthalmology*, vol. 115, no. 6, pp. 949–956, Jun 2008.

[45] A. M. Bagci, M. Shahidi, R. Ansari, M. Blair, N. P. Blair, and R. Zelkha, "Thickness profiles of retinal layers by optical coherence tomography image segmentation," *Am J Ophthalmol*, pp. 679–687, Nov 2008.

[46] T. Fabritius, S. Makita, M. Miura, R. Myllylä, and Y. Yasuno, "Automated segmentation of the macula by optical coherence tomography," *Opt Express*, vol. 17, pp. 15 659–15 669, 2009.

[47] S. Lu, J. Liu, J. H. Lim, C. K.-S. Leung, and T. Y. Wong, "Automated layer segmentation of optical coherence tomography images," *IEEE Trans Biomed Eng*, vol. 57, no. 10, pp. 2605–2608, 2010.

[48] M. Mujat, R. C. Chan, B. Cense, B. H. Park, C. Joo, T. Akkin, T. C. Chen, and J. F. de Boer, "Retinal nerve fiber layer thickness map determined from optical coherence tomography images," *Opt Express*, vol. 13, no. 23, pp. 9480–9491, 2005.

[49] A. Mishra, A. Wong, K. Bizheva, and D. A. Clausi, "Intra-retinal layer segmentation in optical coherence tomography images," *Opt Express*, vol. 17, no. 26, pp. 23 719–23 728, 2009.

[50] A. Yazdanpanah, G. Hamarneh, B. R. Smith, and M. V. Sarunic, "Segmentation of intra-retinal layers from optical coherence tomography images using an active contour approach," *IEEE Trans Med Imag*, vol. 30, pp. 484–496, 2011.

[51] R. J. Zawadzki, A. R. Fuller, D. F. Wiley, B. Hamann, S. S. Choi, and J. S. Werner, "Adaptation of a support vector machine algorithm for segmentation and visualization of retinal structures in volumetric optical coherence tomography data sets," *J Biomed Opt*, vol. 12, no. 4, p. 041206, 2007.

[52] F. Rossant, I. Ghorbel, I. Bloch, M. Paques, and S. Tick, "Automated segmentation of retinal layers in OCT imaging and derived ophthalmic measures," in *Biomedical Imaging: From Nano to Macro, 2009. ISBI '09. IEEE International Symposium on*, 2009, pp. 1370–1373.

[53] K. A. Vermeer, J. van der Schoot, H. G. Lemij, and J. F. de Boer, "Automated segmentation by pixel classification of retinal layers in ophthalmic OCT images," *Biomed Opt Express*, vol. 2, no. 6, pp. 1743–1756, 2011.

[54] V. Kajić, B. Považay, B. Hermann, B. Hofer, D. Marshall, P. Rosin, and W. Drexler, "Robust segmentation of intraretinal layers in the normal human fovea using a novel statistical model based on texture and shape analysis," *Opt Express*, vol. 18, no. 14, pp. 14 730–14 744, 2010.

[55] F. Rathke, S. Schmidt, and C. Schnörr, "Order preserving and shape prior constrained intra-retinal layer segmentation in optical coherence tomography"," in *MICCAI (3)'11"*, 2011, pp. 370–377.

[56] Q. Yang, C. A. Reisman, Z. Wang, Y. Fukuma, M. Hangai, N. Yoshimura, A. Tomidokoro, M. Araie, A. S. Raza, D. C. Hood, and K. Chan, "Automated layer segmentation of macular OCT images using dual-scale gradient information," *Opt Express*, vol. 18, no. 20, pp. 21 293–21 307, 2010.

[57] S. J. Chiu, X. T. Li, P. Nicholas, C. A. Toth, J. A. Izatt, and S. Farsiu, "Automatic segmentation of seven retinal layers in SDOCT images congruent with expert manual segmentation," *Opt Express*, vol. 18, no. 18, pp. 19 413–19 428, 2010.

[58] S. J. Chiu, J. A. Izatt, R. V. O'Connell, K. P. Winter, C. A. Toth, and S. Farsiu, "Validated automatic segmentation of AMD pathology including drusen and geographic atrophy in SD-OCT images," *Invest Ophthalmol Vis Sci*, vol. 53, no. 1, pp. 53–61, 2012.

[59] M. K. Garvin, M. D. Abràmoff, X. Wu, S. R. Russell, T. L. Burns, and M. Sonka, "Automated 3-D intraretinal layer segmentation of macular spectral-domain optical coherence tomography images," *IEEE Trans Med Imag*, vol. 28, no. 9, pp. 1436–47, 2009.

[60] X. Wu and D. Z. Chen, "Optimal net surface problems with applications," in *Proceedings of the 29th International Colloquium on Automata, Languages, and Programming (ICALP), LNCS 2380*. Springer-Verlag, 2002, pp. 1029–1042.

[61] K. Lee, M. Niemeijer, M. K. Garvin, Y. H. Kwon, M. Sonka, and M. D. Abràmoff, "Segmentation of the optic disc in 3D-OCT scans of the optic nerve head," *IEEE Trans Med Imag*, vol. 29, pp. 159–168, 2010.

[62] B. J. Antony, M. D. Abrmoff, M. Sonka, Y. H. Kwon, and M. K. Garvin, "Incorporation of texture-based features in optimal graph-theoretic approach with application to the 3D segmentation of intraretinal surfaces in SD-OCT volumes," in *Proc. SPIE 8314, Medical Imaging 2012: Image Processing*, 2012, pp. 83 141G_1–83 141G_11.

[63] B. J. Antony, M. D. Abrmoff, M. M. Harper, W. Jeong, E. H. Sohn, Y. H. Kwon, R. Kardon, and M. K. Garvin, "A combined machine-learning and graph-based framework for the segmentation of retinal surfaces in SD-OCT volumes," *Biomed Opt Express*, vol. 4, no. 12, pp. 2712–2728, 2013.

[64] Q. Song, J. Bai, M. K. Garvin, M. Sonka, J. M. Buatti, and X. Wu, "Optimal multiple surface segmentation with shape and context priors," *IEEE Trans Med Imag*, vol. 32, no. 2, pp. 376–386, 2013.

[65] Y. Yin, X. Zhang, R. Williams, X. Wu, D. D. Anderson, and F. I. Milan Sonka, "LOGISMOS–layered optimal graph image segmentation of multiple objects and surfaces: cartilage segmentation in the knee joint," *IEEE Trans Med Imag*, vol. 29, no. 12, pp. 2023–2037, 2010.

[66] Z. Hu, M. D. Abràmoff, Y. H. Kwon, K. Lee, and M. K. Garvin, "Automated segmentation of neural canal opening and optic cup in 3D spectral optical coherence tomography volumes of the optic nerve head," *Invest Ophthalmol Vis Sci*, vol. 51, no. 11, pp. 5708–5717, 2010.

[67] B. J. Antony, M. S. Miri, M. D. Abràmoff, Y. H. Kwon, and M. K. Garvin, "Automated 3d segmentation of multiple surfaces with a shared hole: segmentation of the neural canal opening in sd-oct volumes," in *Medical Image Computing and Computer-Assisted Intervention MICCAI 2014*, 2014, pp. 739–746.

[68] OCT Sub-Study Committee for the NORDIC Idiopathic Intracranial Hypertension Study Group, "Baseline OCT measurements in the Idiopathic Intracranial Hypertension Treatment Trial, Part II: Correlations and relationship to clinical features," *Invest Ophthalmol Vis Sci*, vol. 55, pp. 8173–8179, 2014.

[69] J.-K. Wang, R. H. Kardon, M. J. Kupersmith, and M. K. Garvin, "Automated SD-OCT volumetric estimation of severe papilledema: Overcoming truncated scans," *Invest Ophthalmol Vis Sci*, pp. 373:ARVO E–Abstract 3922, 2012.

[70] F. L. Bookstein, "Principal warps: thin-plate splines and the decomposition of deformations," *IEEE Trans Pattern Anal Machine Intell*, vol. 11, no. 6, pp. 567–585, 1989.

[71] J.-K. Wang, R. H. Kardon, and M. K. Garvin, "Automated bruchs membrane opening segmentation in cases of optic disc swelling in combined 2D and 3D SD-OCT images using shape-prior and texture information," in *Proceedings of the Ophthalmic Medical Image Analysis Second International Workshop, OMIA 2015, Held in Conjunction with MICCAI 2015, Munich, Germany*, October 9, 2015, pp. 33–40.

[72] J.-K. Wang, M. S. Miri, R. H. Kardon, and M. K. Garvin, "Automated 3-D region-based volumetric estimation of optic disc swelling in papilledema using spectral-domain optical coherence tomography," in *Proc. SPIE 8672, Medical Imaging 2013: Biomedical Applications in Molecular, Structural, and Functional Imaging*, 2013, pp. 867 214_1–867 214_8.

[73] E. J. Sigler, K. G. Mascarenhas, J. C. Tsai, and N. A. Loewen, "Clinicopathologic correlation of disc and peripapillary region using SD-OCT," *Optom Vis Sci*, vol. 90, pp. 84–93, 2013.

[74] W. H. Nailon, "Texture analysis methods for medical image characterisation," in *Biomedical Imaging*, Y. Mao, Ed. InTech, 2010, ch. 4.

[75] Z. Hu, G. G. Medioni, M. Hernandez, and S. R. Sadda, "Automated segmentation of geographic atrophy in fundus autofluorescence images using supervised pixel classification," *J. Med. Imag.*, vol. 2, no. 1, pp. 014 501_1 – 014 507_7, Jan. 2015.

[76] J.-K. Wang, P. A. Sibony, R. H. Kardon, M. J. Kupersmith, M. K. Garvin, and on behalf of the OCT Sub-Study Committee for the NORDIC Idiopathic Intracranial Hypertension Study Group, "Semi-automated 2D Bruch's membrane shape analysis in papilledema using spectral-domain optical coherence tomography," in *Proc. SPIE 9417, Medical Imaging 2015: Biomedical Application in Molecular, Structure, and Functional Imaging*, 2015, pp. 941 721_1–941 721_10.

[77] J.-K. Wang, P. A. Sibony, R. H. Kardon, M. J. Kupersmith, and M. K. Garvin, "Change in the deflection of the neural canal opening over time with acetazolamide treatment in idiopathic intracranial hypertension," *Invest Ophthalmol Vis Sci*, pp. 278:ARVO E–Abstract 2233, 2015.

[78] J.-K. Wang, S. S. Johnson, R. H. Kardon, P. A. Sibony, M. J. Kupersmith, and M. K. Garvin, "Threedimensional bruchs membrane shape model in cases of papilledema," *Invest Ophthalmol Vis Sci*, pp. 526:ARVO E–Abstract 6113, 2016.

[79] T. F. Cootes, C. J. Taylor, D. H. Cooper, and J. Graham, "Active shape models — their training and application," *Comput Vis Image Underst*, vol. 61, no. 1, pp. 38–59, 1995.

[80] D. M. Mount and S. Arya, "Approximate nearest neighbor library," 2010, http://www.cs.umd.edu/ mount/ANN/.

[81] M. Kuhn and K. Johnson, *Applied Predictive Modeling*. Springer-Verlag New York, 2013.

[82] P. A. Sibony, M. J. Kupersmith, S. E. Feldon, J.-K. Wang, M. Garvin, and OCT Substudy Group for the NORDIC Idiopathic Intracranial Hypertension Treatment Trial, "Retinal and choroidal folds in papilledema," *Invest Ophthalmol Vis Sci*, vol. 56, no. 10, pp. 5670–5680, 2015.